ABSTRACT

SHABANIZARINKAFSHRASHTI, ELNAZ. Free Surface Melt Electrospinning: A Solvent Free Approach Toward Electrospinning. (Under the direction of Dr. Russell E. Gorga).

This Ph. D. dissertation studies the melt electrospinning from a flat plate source, known as free surface melt electrospinning. The replacement of single needle configuration with a free surface flat plate source is promising in addressing multiple limitations inherent to melt electrospinning, including production rate and frequent clogging issues. This Ph.D. dissertation explores techniques for fiber diameter attenuation, a significant challenge in melt electrospinning, and the corresponding microstructural transformation effect on the fibers' mechanical properties to derive process-structure-property relationship.

Chapter 1 introduces the field of melt electrospinning, including the configuration design, challenges, and the approaches that have been explored so far to address them. Particular focus is on free surface electrospinning as an emerging approach for scaling up electrospinning. Theoretical background for free surface electrospinning, particularly the electric field interaction with fluid surface tension leading to spontaneous perturbation formation on the free surface of a fluid, is explored. Ultimately, the most recent free surface interventions both for the solution and melt electrospinning is reviewed.

Chapter 2 demonstrates an efficient in situ imaging technique for exploring micron to sub-micron level objects and processing. To be able to navigate the optimization of melt electrospinning, it is essential to gather visual information about the cone formation, cone size, jet diameter, and other details inherent to the process. In this chapter, the development of backlighting technique is introduced as an imaging method capable of revealing precise edges and detailed information of tiny objects, and the broader implication of the technique (e.g., tubeless siphoning)

is explored. With this technique, the melt electrospinning jet's solidification process, as it moves along the spin-line, becomes observable.

In **Chapter 3,** the solidification information revealed by the backlighting technique is implemented as a basis to utilize the strategy of controlling the spin-line temperature profile to explore fiber diameter attenuation. Spin-line temperature profile, the temperature in the spinning zone, is shown to be a significantly effective strategy in decreasing fiber diameter, reported to being by four-folds. To validate the solidification length, revealed by the backlighting technique, computation fluid dynamic simulation by COMSOL was used to map spinning jet's temperature profile.

Chapter 4 derives microstructural information, in particular, mechanical properties with regard to spin-line temperature profile, as the leading processing strategy for fiber diameter attenuation, which was explored in chapter 3. Increasing the spin-line temperature profile above 100 °C in the cone zone creates fibers with only a few microns (~ 3.5 microns), which is comparable to commercialized production techniques like melt blowing while enhancing the tensile strength, yield strength, and toughness of the fibers without compromising the stiffness and Young's modulus.

Chapter 5 summarizes the state of the melt electrospinning and the futuristic pattern of the technique as an alternative production approach, especially in the time of crisis like the current pandemic where access to respirators and surgical masks has become extremely challenging. For the melt electrospinning to be commercialized, some issues must be addressed that are discussed in this chapter, along with the potential solutions.

The research presented in this Ph.D. dissertation aims to aid future research in applying and commercializing the melt electrospinning.

Free Surface Melt Electrospinning: A Solvent Free Approach Toward Electrospinning

by
Elnaz Shabanizarinkafshrashti

A dissertation submitted to the Graduate Faculty of
North Carolina State University
in partial fulfillment of the
requirements for the degree of
Doctor of Philosophy

Fiber and Polymer Science

Raleigh, North Carolina
2020

APPROVED BY:

_____	_____
Dr. Russell Gorga Committee Chair	Dr. Jan Genzer
_____	_____
Dr. Wendy Krause	Dr. Xiangwu Zhang

DEDICATION

To Alireza, my beloved husband and the love of my life, for being my best buddy since ever and for always being there for me.

Thank you for making my world beautiful!

To my family for all their sacrifices.

Mom, Dad, Puriya, thank you for being supportive of all my decisions!

To Sheyda, my adorable forever friend, in appreciation to her sense of empathy.

Thank you for being my rock through rough times!

And to myself for withstanding the hardest four years of my student life.

Thank you for never giving up!

BIOGRAPHY

Elnaz Shabani was born on December 3rd, 1990 in Rasht, Gilan, Iran to Shahla Kooshesh and Hamid Shabani and has one younger brother, Puriya Shabani. Elnaz was a writer at the age of 10, fell in love at the age of 18, and became a Polymer Engineer at 22. She was the first person in her family to attend college and the only student in her class of 2009 to get admission from the second-best university of Iran, Tehran Polytechnique. In May 2016, Elnaz graduated from Tehran Polytechnique with a master's degree in Polymer Engineering and few months after, began her PhD in the Wilson College of Textiles at NC State University. In March 2017, she joined the lab of Professor Russell E. Gorga studying free surface melt electrospinning. Under his supervision, Elnaz mentored four undergraduate students in the lab and developed a passion for teaching, mentorship, and leadership roles. During her time as a PhD student, Elnaz worked through a minor degree in Engineering Education where she conducted a research on creativity development in first year engineering design students under the supervision of Dr. Cameron Denson. She also got the Teaching and Communication Certificate where she taught polymer engineering to a class of very diverse audiences, the Leadership Development Certificate where she served in a project for hunger and homelessness, was selected as a Preparing the Professorate fellow, served as the Textile Graduate Student Association Secretary, and was a member of the SciBridge club. Her favorite things in the world are spending time with Alireza, her dog, and her friends, reading Dostoyevsky while listening to Baroque music and drinking Persian tea in a see-through glass cup, and following fashion design.

ACKNOWLEDGMENTS

The completion of my PhD would never have been possible without the support of many people and I wish to express my sincere appreciation to all of you who supported me over the last four years.

A very special thanks to my thesis supervisor, prof. Russell E. Gorga for giving me the opportunity to explore all the facets of this project and for being supportive of my non-scientific interests throughout my years at NC State. Dr. Gorga, I admire your open-minded approach in taking research directions, your patience and sense of empathy, and the unique care you give to each and every hundreds of students that you teach or advise. I truly appreciate the trust you had in me in navigating this project, in mentoring students in the lab, in being your teaching assistant for two semesters, and so many other things. The hands-off approach even though frustrating at times, is the reason for the empowered independent researcher that I became today, and for all of these I am grateful to you. Thank you for being extremely patient with me for the past 3.5 years. My inbox will miss the warmth of your occasional “Are you doing ok?” emails.

All members of my thesis Committee, Drs. Jan Genzer, Wendy Krause, and Xiangwu Zhang were instrumental in expanding the scope and improving the quality of the work. Special thanks to Dr. Jan Genzer for opening his lab to me and helping me getting the diverse and valuable experience of working in a chemistry lab and being able to explore a different aspect of the project. I appreciate Dr. Wendy Krause for her support and constructive feedbacks with publishing my first paper.

I would like to thank Taslim Ur Rashid for being the best lab mate and writing mentor ever. Taslim, thanks for all the genuine support you offered to me in the past two years. Getting my

publications out would have never been possible without your advices and encouragements. You are going to make an incredible professor and I wish all the best for you.

I would like to thank Dr. Vanessa Doriott Anderson for being the mentor I have always been looking for. Vanessa, thank you for teaching me so much both personally and professionally. You were the first person who showed me introverts can make wonderful caring teachers and I look forward to using all the things you taught me in my future career. I would like to express my appreciation to Dr. Cameron Denson in college of education for helping me to navigate my minor degree in engineering education and to establish my independent research in this field. I would like to thank Dr. Laura Bottomley for kindly letting me to conduct the research in her freshman engineering design classrooms.

I had the privilege of mentoring four undergraduate students throughout my PhD and I am grateful for their efforts and enthusiasm. Rebecca Komer and Patrick Hughes thanks for your time, helps, and companionship throughout this project and I look forward to seeing what you all will accomplish.

I would like to thank my husband for always being supportive, for being so much selfless, and for being the reason for me to experience love every minute of my life. Alireza, all I want is to grow old with you. To my mom and dad, thanks for all the sacrifices you made. Mom, I learned from you the value of hard work and dad, thanks for always being proud of me no matter what. My little brother Puriya, thanks for being the most caring brother in the world, I am very proud of you. To my friends, Sheyda, Yasaman, Ghazal, Nikki, Amirhassan, Mohammad, and Roshan thanks for being with me through worst and best. You are not just friends; you are like family members. And finally, thanks to my dog, Shiny, for always making me laugh at the end of a busy day, you are mama's fur baby. You all are my entire assets in life.

TABLE OF CONTENTS

LIST OF TABLES

LIST OF FIGURES

CHAPTER 1: Literature Review on Free Surface, Unconfined Electrospinning as a New Approach to Scale Up Melt Electrospinning

Elnaz Shabani[1], Neelam Sheoran[2], Jason R. Bochinski[2], Laura I. Clarke[2], Russell E. Gorga [1]
[1]Fiber and Polymer Science Program, North Carolina State University, Raleigh, NC 27695, USA
[2]Department of Physics, North Carolina State University, Raleigh, NC 27695, USA

Abstract

As a sustainable approach toward traditional solution-based electrospinning, melt electrospinning has drawn much attention in recent years as an eco-friendly process to produce thin fibers. Several studies have reported on the equipment innovation and process parameters to overcome some of the complexities inherent to this method, including high melt viscosity, production rate, and fiber diameter. This review provides a summary of the principles and configurations of the melt electrospinning process and the challenges associated with this method. Subsequently, it introduces free surface electrospinning along with fundamental physical concepts of this newly proposed electrospinning technique. The article provides a comprehensive review of theoretical equations related to fiber formation from a free surface of a liquid. Furthermore, free surface electrospinning as an alternative way to overcome many complexities of melt electrospinning to produce thin and continuous fibers is introduced and reviewed.

Keywords: Electrospinning, Melt electrospinning, Free surface electrospinning

1.1. Introduction

Polymer nanofibers, having a superior surface area-to-volume ratio, have a wide range of applications in many different fields, including chemical sensing[1–3], filtration[4,5], biomedical applications[6,7], composite material[8], and membranes[9-11]. These polymer nanofibers are produced widely using the process of electrospinning. In general, an electrospinning setup includes a source containing the polymeric fluid, an applied voltage, and a collector to collect the produced fibers. The overall idea of electrospinning is first, a voltage difference is applied between the polymeric fluid and the collector, then a polymer jet will be ejected toward the collector while solidifying in the spin-line.[12] Broadly, the electrospinning technique divides into two major categories: solution-based and melt based. In solution-based electrospinning, a very definitive solvent is needed to dissolve the given polymer. Further, jet formation occurs once the high voltage is applied to the polymer solution, which subsequently solidifies in the spin line by solvent evaporation. Conversely, melt electrospinning is a solvent-free method. Polymer melt forms polymer fibers after the solidification of the jets below the polymer melting point in the spin-line.[13] So far, there has been much research focusing on the solution-based method. However, due to some difficulties regarding the apparatus design and reaching an optimal viscosity range, melt electrospinning has been less a subject of research. Subsequently, solution-based techniques have some disadvantages, such as the use of toxic solvents, porosity on fibers surface, and finding definitive solvents for some commercial polymers (namely polyethylene and polypropylene). Melt electrospinning has attracted more attention in the last 15 years to overcome these challenges.[14] In this review, recent developments in the field of melt electrospinning are provided, followed by an introduction to free surface electrospinning as a new approach to scaling up melt electrospinning to a viable industrial scale.

In general, most of the electrospinning setups include a nozzle as a spinneret producing a single fiber, which leads to the problems of clogging and low fiber production. The introduction of free surface electrospinning eliminated this problem. Free surface electrospinning is a process in which multiple jets are formed from any polymeric fluid surface when an external electric field is applied to it and hence utilizing all the polymers for fiber production. There are different configurations designed for free surface melt electrospinning where magnetic fluids[15], balls[16], discs[17], wires[18], cylinders[19], etc., were used as rotators in the polymer solution to form multiple jets. Our research group made some recent developments, including fluid-filled bowl[20–23] and unconfined plate edge melt electrospinning[24,25] to scale up the fibers' yield. One of the significant disadvantages of free surface melt electrospinning is that there is a comparatively large open surface area where jet formation takes place along with other undesired processes such as solvent evaporation, water vapor adsorption, and corona discharges. This review summarizes the general theory behind free surface melt electrospinning by giving a theoretical background of some well-developed configurations.

1.2. Electrospinning

There are several methods of producing sub-micron fibers in the Textile industry, including melt spinning, melt blowing, electrospinning, etc.[26,27] Among them, electrospinning is famous for its simplicity in the design, large surface area to weight/volume ratio, small pore sizes in the web structure[13], ease of fiber functionalization (either by blending the solution prior to electrospinning[28-30], or using core-shell electrospinning setup[30,31], along with the ability to produce highly porous three-dimensional scaffolds from various polymer systems with application in tissue engineering[32-34]. Electrospinning has broadly two categories: solution electrospinning and melt-

electrospinning, according to the material used for spinning. Over the decades, solution electrospinning has been widely producing nanofibers from several types of polymers. In a study done by Dasdemir et al.[35], a comparison between melt and solution electrospun thermoplastic polyurethane (TPU) fiber showed that the deposition rate of the melt electrospun fibers is higher than the solution ones (0.6 g/h to 0.125 g/h). Moreover, the surface of the fibers produced in melt electrospinning is smooth compared to solution ones. However, the TPU fibers fabricated by melt electrospinning have a higher average diameter, which ranges from 4 to 8 μm compared to 220 to 280 nm for solution ones. The operational voltage in the melt method is a lot higher than the solution method, which is due to the higher viscosity of the polymer melts.[35] Disadvantages associated with the solution electrospinning, including the use of toxic solvents discharging to the atmosphere during the spinning time, the limited solubility of commercial thermoplastic polymers (such as polyethylene and polypropylene), and lower production rate has drawn much attention to the melt electrospinning.[35–37] The main difference in a melt electrospinning setup is designing a feeding part that includes a heater to melt the polymer. Also, the high voltage is usually applied to the collector instead of the fluid to prevent any damage to the heating systems. The following sections provide a comprehensive review of melt electrospinning. Ultimately free surface electrospinning is introduced as a new approach to overcoming several challenges inherent to this method, including intricate equipment design and the inherent difficulty associated with polymers like high viscosity, which can cause substantial clogging problems when the polymer melt pumps through a tiny nozzle.

1.3. Configuration and Parameters of Melt Electrospinning

A melt electrospinning setup has three significant parts. The first part consists of a melt supply zone with a heating system and a thermal sensor in which polymer converts to a molten state. The second part has a high voltage supply device that can electrically charge the polymer melt. Finally, the third part with a conductive collector where fibers are collected. Some other significant parts of configurations in melt electrospinning include a jet zone in which the jet's cooling and solidification occur [14,38]. The next part of the review discusses the significant components of this system and its configuration.

1.3.1. Polymer melt supply zone

The supply zone can be a metal tube container or a syringe in which polymer pellets or powders start to melt before the beginning of the process.[38–45] Also, there exist other types of melt supply zone such as plastic reservoir [46], a twin-screw extruder[47], or a combination of a reservoir with a screw extruder that can control the extrusion rate.[48] Recently, these tubular reservoirs have been replaced with an aluminum plate in which polymer melt can be electrospun from a free surface.[24]

1.3.2. Spinneret diameter

In most cases, the spinneret is a metal needle connected to the syringe or any melt supply zone through which polymer melt will shape and eject from the melt supply zone.[14] Spinneret diameter controls the final fiber diameter. Also, in some cases, spinneret temperature is controlled separately from the melt supply zone. In this case, the spinneret temperature is kept higher than the melt supply zone to decrease melt viscosity where it must flow through the small hole of the spinneret and avoid rapid solidification of the Taylor cone.[49]

1.3.3. Flow rate

Flow rate is the rate at which polymer fluid is pumped, and it has a significant effect on fiber diameter and morphology.[49] Dalton et al. showed that low flow rates are needed for melt electrospinning because more charges exist on polymer melts with a lower flow rate.[50] In another study by Dalton et al., it was shown that the flow rate of as low as 5 µL/h (compared to solution electrospinning) yields the smallest fiber diameter. Greater flow rates yield thicker fibers with the molten polymer collected on the collector that deteriorate nanofibers' fine properties, such as the small diameter and high surface area.[51] It is noteworthy to mention that a minimum flow rate is required to maintain a Taylor cone.[46] Recent developments of free surface electrospinning yield self-control of the flow rate depending on the number of self-initiated cones from the free surface of the polymer melt.[24,40] In a study done by Yang et al., several jets self-initiate at the rim of a free surface umbellate nozzle that yields to a high production rate of 1-100 g/h.[40]

1.3.4. Collection distance

Collection distance plays a crucial role as it provides time for the fibers to cool and solidify during spinning before they reach the collector. Collection distance should not be minimal as it can cause molten fibers deposition on the collector, and fiber diffusion occurs at the cross points.[52] Furthermore, collection distance affects the final fiber diameter. Shen et al. showed that by increasing collection distance first fiber diameter decreased to a certain amount due to the high degree of stretch followed by an increase due to the weakening of the electric field.[44] Yang et al. investigated the effect of electrospinning distance with a constant electric field of 3 kV/cm. They showed that thicker fibers form due to low voltage and small distance as it does not allow for enough elongation. At very long distances with high voltages, thick fibers are produced because

fibers are solidified long before reaching the collector.[38] Therefore, there needs to be an optimum combination of distance and voltage that yield to the smallest fiber diameter.[53]

1.3.5. Applied voltage

In the solution-based systems, the fluid gets charged by applying the high voltage directly to the feeding zone. It is unique to the melt electrospinning method that a high voltage is applied to the collector to prevent any damage to the heating sensors of the metal supply zone. Also, the supply zone with heating sources is grounded.[52] Joo et al. showed that by increasing voltage from 5 kV to 10 kV, local vibration of the jet starts to occur, and as the voltage increases to 20 kV, these vibrations evolve to whipping motions, which ultimately form thinner fibers.[49] Lyons et al. showed that in the melt electrospinning process, higher voltages are needed compared to solution electrospinning due to high polymer melt viscosity. However, beyond a critical voltage, an electrical discharge occurs. They also showed that the higher the voltage is, the thinner the fiber can get.[54] Ko et al. showed that by doubling the voltage, the fiber diameter decreases by 275%.[55] A more detailed result is shown by Yang et al. that fiber diameter is inversely proportional to the applied voltage up to some extent, but increasing the applied voltage beyond a critical value, fiber diameter increases. They provided two different reasons for this observation. Firstly, a stronger electric field can form a bigger Taylor cone causing more polymer melt to eject out of the nozzle. Second, a stronger electric field can cause more stretching and hence accelerate fiber collection on the collector failing fibers to undergo enough attenuation.[39,56] In a study done by Yang et al., an umbellate nozzle was used instead of a single needle in which several jets were made simultaneously at the rim of the umbellate nozzle. They showed that in this process, by increasing the applied voltage, the number of Taylor cones and the subsequent number of jets increases. Both

these reasons result in the decrease of inter-jet distance, and simultaneously, the speed of the jets in the electric field increases, leading to thinner fibers.[41,56]

1.3.6. Electric field

When subjected to an electric field, insulating materials like plastics and polymers get polarized with charges formed on their surface.[56] The charges can move inside or on the surface of the materials, and as the polymer melt's viscosity is higher than the solution, the charge density in melt electrospinning is lower than the solution.[57] Polymer jets with more surface charges are stretched more in the electric field. The electric field applies a force (Fe) on the charged jet in the spin line, defined by the following equation:

$$F_e = \frac{1}{2}\,\varepsilon E^2 \tag{1}$$

In which E is the electric field intensity, and ε is the relative permittivity of the air. The electric field intensity depends on the voltage, collection distance, and the geometry of the spinneret.[56] Another factor influencing the electrospinning process is the polarity of the applied voltage, which determines the direction of the electric field. In a study done by Schmidt et al., it was shown that if the applied voltage to the collector is positive, which makes the polymer melt negatively charged, a lower critical applied voltage and hence a lower electric field is needed. On the other hand, by applying a negative voltage at the collector, a positive net charge density at the emerging Taylor cone will form, yielding thinner and more uniform fibers.[58] The uniformity of the electric field in setup is an important factor that affects the stability of the process. In a study done by Liu et al., two parallel disks were used as electrodes for electrospinning to make a uniform electric field. Figure 1.1. They observed that electric field intensity on the edge of the metal disk is always stronger than the field at the center of the disk. The distribution and uniformity of the electric field depends on the diameters, distances, and relative areas of the disks.[59]

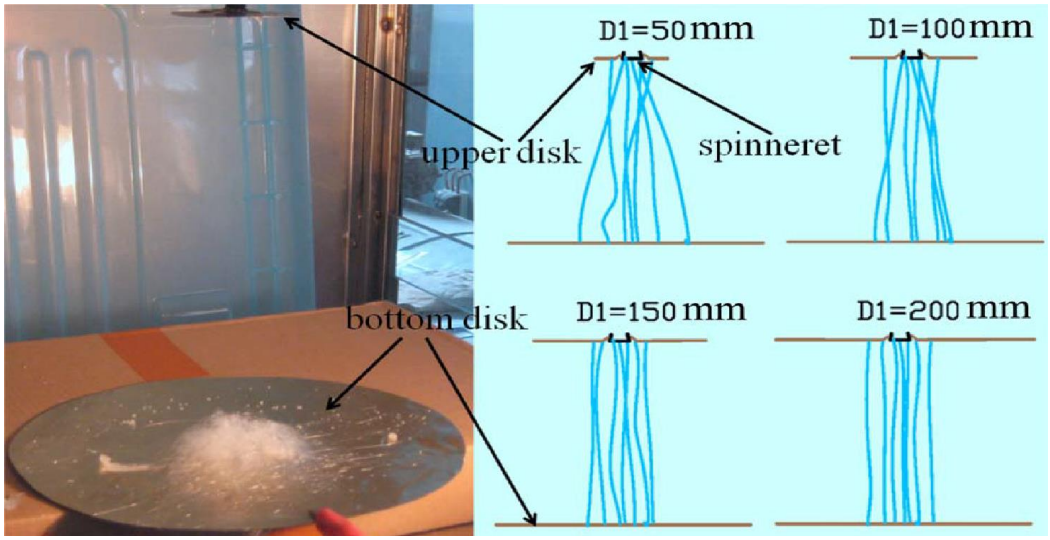

Figure 1.1. Melt electrospinning with parallel disks and the effect of the upper disk size on the stability of the process. Reproduced from Ref. 58, with permission from John Wiley and Sons.

In a study done by Liu et al.[59], the effect of a pulsed electric field on the fiber diameter and fiber diameter distribution was studied. Two factors of the pulsed electric field, frequency and the duty cycle (the ratio of the time that the voltage is on to the time that it is off), affected the final fiber properties. Figure 1.2 shows the schematic of the setup, along with the pulsed electric profile. The average fiber diameter decreases as the frequency increases, and it is smaller than the samples made during normal melt electrospinning.

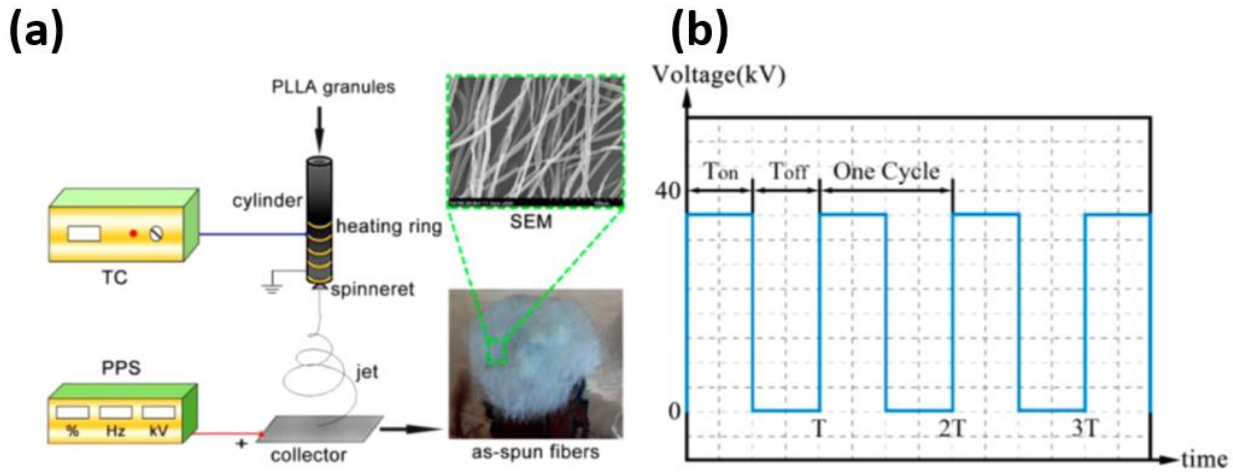

Figure 1.2. (a) Schematic diagram of the setup: (b) Schematic diagram of the output voltage. T represents the cycle. Frequency=1/T_{on} + T_{off} , duty cycle=$\frac{T_{on}}{T_{off}}$. Reproduced from Ref. 59, with permission from American Chemical Society.

According to them, the faster disentanglement of the polymer chains under pulsed electric field mode, yielding molecular orientation and fiber thinning, was a reason for this observation. The fiber diameter distribution was broader in a pulsed mode due to the acceleration and deceleration of the jet in the electric field. At a higher duty cycle, as the active time of the applied voltage increases (duty cycle=$\frac{T_{on}}{T_{off}}$), the jets underwent more stretching and hence attenuation. However, there is an optimum duty cycle at a particular frequency that yields the finest fiber diameter.

1.4. Spinning line Temperature Control

Controlling the polymer melt viscosity is one of the critical factors affecting the stability and the final fiber properties in the melt electrospinning technique. Broadly, two different approaches have been used to control the melt viscosity in this process. Garmabi et al. used a plasticizing agent to adjust the viscosity of the PLA to a certain degree to get the finest fibers.

They showed that at a spinning temperature of 180 °C adding 10-30% of polyethylene glycol (PEG) to the PLA enhances the spin ability of the PLA significantly, while by adding more than 30%, the spina bility diminishes due to the lack of elasticity and melt strength.[43] The second approach for controlling the viscosity is controlling the spin-line temperature. The following sections introduce two methods of controlling the spin-line temperature that has been used by researchers.

1.4.1. Heating chamber

Joo et al. used a heated chamber to control the spin line temperature. For this study, the group used polypropylene (PP) as the polymer. They showed that by increasing the spin line temperature to 80 °C stronger whipping motions happen, incorporating further stretching and thinning of the fibers. Also, to prevent melt degradation in the nozzle (due to higher shear forces applied by the tiny nozzle on the melt), its temperature was controlled separately from the melt reservoir to a lower degree. The temperature of the collector was cooled down separately for the PP fibers to maintain their orientation after collecting them on the collector.[14,49]

Kim et al.[52] used a two-part heating chamber. The first part of the spin-line, close to the spinneret where the temperature can reach to 150°C, is controlled by a ring-shaped heater while keeping the second half of the spin line at room temperature. Figure 1.3. Heating around the nozzle decreased the viscosity of the polymer (PLA) melt, and the subsequent exposure to room temperature maintain jets' structure and orientation.

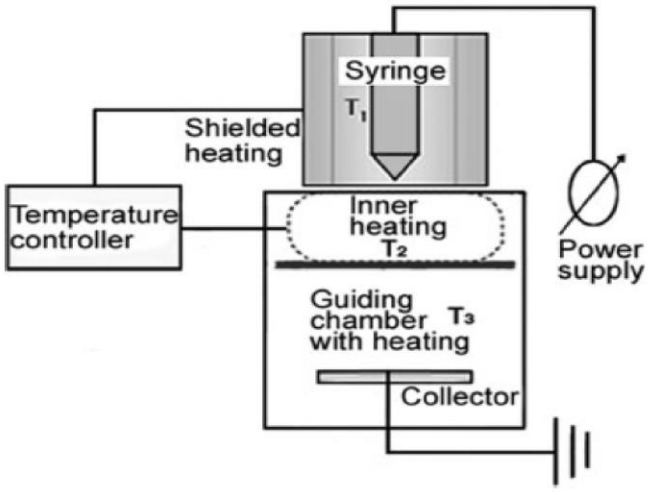

Figure 1.3. A melt electrospinning setup with a two-part spin-line temperature control. Reproduced from Ref. 52, with permission from John Wiley and Sons.

1.4.2. Hot airflow

In another study done by Joo et al., the spin line temperature was controlled by hot airflow. The advantage of this method over using a heater is the simplicity of the design since controlling the nozzle temperature separately from the spin-line brings much complexity to design. The hot airflow contributes to the jet thinning process in two ways: first, by delaying the solidification of the jet in the spin-line, and second, the drag force coming from the airflow on the jet surface can further stretch the fibers to a lower diameter. The fiber diameter with the aid of this method decreased from 3.5 μm to 0.18 μm, where air velocity was 300 m/s and T(air)=483K.[11]

Yang[39] and Bubakir et al.[100] used a melt differential electrospinning setup (described in section 1.6.2) with an airflow assisted part and a ring-like electrode. The advantage of using airflow is an air pressure gun, which intensifies the airflow and causes an extra stretching force acting on the jet. Also, it contracts the flying jets and prevents them from being attracted by the inner circle of the ring electrode.

Fong et al. showed the effect of the hot airflow on chain orientation and crystallinity. They used two different temperatures of 80°C and 120°C along with two fast and slow modes of the gun airflow. The study showed that at a higher speed of the airflow at T=120°C, fibers were slightly thinner with maximum orientation and crystallinity, with the crystal content changing from 8.3% to 27.2%. In this method, the gun airflow was perpendicular to the jet line. Consequently, it can further stretch the spinning fibers.[60]

While melt electrospinning opens the window towards a green fabrication methodology to produce mesoscale fibers, several processing issues are associated with this method. Lower production rate compared to other fiber melt processing techniques and persistent clogging problems when pumping high viscosity polymer melt through a tiny nozzle are among the main issues. Free surface unconfined electrospinning is a new methodology for enabling scale-up to commercially viable production rates while overcoming the clogging problems associated with needle-based techniques. The following sections summarize this discovery and how it can incorporate as a new approach towards melt electrospinning.

1.5. Background and Introduction of Free Surface Electrospinning

Needle electrospinning is a very well researched area with the capability of producing nanofibers with potential applications in fields of filtration, nanoelectronics, textile industry, tissue engineering, drug delivery, and wound dressing.[62–65] Needle electrospinning works on the principle of forming Taylor cones under critical conditions. Taylor cone formation depends on the proportion of the velocity with which jet launches from the polymer solution to the intensity of the applied potential. This ratio is limited as the electrode discharges once the maximum electrostatic field reaches the dielectric strength of the air. While melt electrospinning opens the window toward

a green fabrication methodology to produce thermoplastic mesoscale-fibers, there are several processing issues associated with this method. Persistent clogging problems when pumping high viscosity polymer melt through a tiny nozzle and the relatively large fiber diameter are a few main problems. Since instead of mechanical forces, only electrostatic forces come into play here, the advantage of fibers forming in the same space and time causing deposition of fibers in quasi-random orientation becomes one of the disadvantages for this system. However, the main problem of this electrospinning process is the low yield of nanofibers. Even after an hour-long process, the production of fibers is as low as 0.1g to 1g, which is very concerning from an industrial point of view. Free surface unconfined electrospinning is a new methodology toward enabling scale-up to commercially viable production rate.

Fundamentally, one of the remarkable features of electrospinning is that jets can be launched from any polymeric fluid surface resulted in the development of what is collectively referred to as "free surface electrospinning." Various investigators reported a different number of configurations describing free surface electrospinning. In many previous approaches, the jetting was achieved at much higher potentials, approximately 10^8 V/m. In 2004 Yarin et al.[15] proposed a new approach where they investigated the effect of the magnetic field and electrostatic field on the two-layer system, with the upper layer being the polymeric solution and the bottom layer being a ferromagnetic suspension. A standard magnetic field was applied to the two-layer method, resulting in stable vertical spikes of magnetic suspension perturbing the free surface of the topmost layer of a polymeric solution, and besides, the interlayer interface between the two also starts perturbing. Several jets launched from the free surface were directed upwards once the electric field was applied to this running setup, resulting in a 12-fold higher production rate while at the same time eliminating clogging problems. Along with the developments mentioned in this

approach, at a much lower magnitude of an electric field (10^5 V/m), spinning was achieved due to the magnetic fluid spikes pushing the jet formation. However, this method has a limitation that it can only work with the non-interactive pairs of a polymeric solution and oil-based ferromagnetic suspension.

On similar grounds, a patent[66] aimed at inventing a setup that can reach a higher yield of nanofibers, making it suitable for industrial drives. A method wherein the presence of the electric field forms a free-spinning surface on the charged rotating electrode was developed. The rotating electrode itself is transporting the polymer solution forming jets from the surface near the counter electrode. Several improvements were made in the base design to increase the polymer production rate and create uniform fibers. By sucking the air, an airstream was formed in the direction of the counter electrode to drift the jets more towards it to make thinner fibers. In addition to this, drying air was supplied in the space between the electrodes where fibers are formed to quicken the evaporation of solvent, hence increasing the productivity. One of the advantages of nanofibers being produced using this method is that they are being deposited as layers on counter electrode, creating not only high-quality fibers but also uniform layers of it, which is an essential factor in designing devices and has potential applications.

1.5.1. Theoretical Background and Equations in Free Surface Electrospinning

Taylor and Van Dyke described a critical voltage Vc is needed for jet formation in traditional needle electrospinning given by

$$\sqrt{4ln\left(\frac{2h}{r}\right)\pi r\gamma 1.30(0.09)} < V_c < \sqrt{4ln\left(\frac{4h}{r}\right)\pi r\gamma 1.30(0.09)} \quad (2)$$

Where Vc is in kilovolts, r is the capillary radius, h is the distance between the collector with zero hydrostatic pressure and capillary, and γ is the surface tension of the given liquid. However, the basic principle of needleless electrospinning is that applying a high voltage to polymer fluid causes

multiple jets perturbing simultaneously. In 2008 Lukas et al.[67] formulated a hypothesis that explains the self-organization of jets on one-dimensional free liquid surfaces in terms of electrohydrodynamic instability of surface waves. Dispersion law was thoroughly analyzed to validate this hypothesis. This model explained that the mechanism of the "fastest" forming instability causes the self-initiation of jets on a mesoscopic scale when an electric field is above the critical value. This model also predicted inter-jet distance as well as a relaxation time for spontaneous jetting for the potential above the critical value. Dimensionless parameters, which are universally valid for all conductive liquids of electrospinning number and inter-jet length, were defined.

The motion of the liquid surface wave can be described as periodic wave disturbance in z-direction given by,

$$\in = Aexp[i(kx - \omega t)] \tag{3}$$

A is the amplitude of the wave, k is the wavenumber, ω is the angular frequency, and t stands for time. Euler's equation given by Eq (4) was solved to get a dispersion law for ω^2.

$$\rho \frac{\overrightarrow{dv}}{dt} + \nabla p = 0 \tag{4}$$

$$\omega^2 = (\rho g + \gamma k^2 - \epsilon E_0^2 k) \frac{k}{\rho} \tag{5}$$

The pressure term in eq(5) is composed of three different pressures, capillary pressure $p_c = -\gamma(\partial^2\xi/\partial x^2)$, electric pressure p_e, and hydrostatic pressure $p_h = \rho g\xi$. Assumptions made to solve Euler's equation is that the wave amplitude is initially neglected with respect to the wavelength and potential on surface quenches as $z \to \infty$. For every wavenumber k, if the corresponding value of ω^2 is positive, the system is defined as stable. "Running" waves of constant amplitudes are observed for voltages lower than the critical value. The Critical value for the field was calculated by setting $\omega^2=0$.

$$E_c = \sqrt[4]{4\gamma\rho g/\epsilon^2} \quad (6)$$

The above equation allows for the definition of a dimensionless electrospinning number, $\Gamma = a\epsilon E_0^2/2$, which holds the threshold condition for electrospinning. Above this critical field, the value of ω^2 becomes negative and minimal, and hence the calculation and discussion become vital. Another dimensionless quantity, $\Lambda = \lambda / a$, has been introduced as intra-jet distance, where $\lambda = 2\pi / k$ and k's are obtained by finding the minimal value of ω^2 ($d\omega/dk=0$). The relationship between two dimensionless quantities Γ and Λ is given by:

$$\Lambda = \frac{3\pi}{\Gamma+\sqrt{\Gamma^2-3/4}} \quad (7)$$

Electrospinning starts when Γ and Λ cross their respective critical values ($\Gamma \geq 1$, $\Lambda_c = 2\pi$). Finally, relaxation time and T have been related using dimensionless wave number $K=2\pi / \Lambda$.

$$T = \sqrt{\frac{3}{2K(K\Gamma-1)}} \quad (8)$$

All these relationships (eq 10,11) are universally valid for all conductive liquids. This model also explained a strong correlation between field strength and jet density, which can be further explored to make different electrospinning configurations. However, the model neglected the constructive wave interference effect in 1-dimension, which could be the reason causing lower critical field values. Waves with amplitude bigger than original one's form because it locally increases the field value in the liquid film area.

In 2009, Miloh et al.[18] formulated a theoretical model explaining electrically driven instability and jet launching from a spherical free surface liquid layer and compared it with previously published experimental results. The purpose of this theoretical model was to demonstrate that spherical electrodes can launch multiple jets radially from the surface when the polymer is subjected to an electric field above the critical value. The Model started with the

assumption that the polymer layer of the sphere behaves as an ideal conductor (satisfying $\tau_c\gamma \ll 1$), and hence free surface is equipotential. This assumption is based on the ratio of characteristic hydrodynamic time(γ) to characteristic charge relaxation time(τ_c). Considering normal Maxwell stress, capillary pressure, and viscous stress, the stability criterion for perturbation growth rate σ have been formulated as:

$$\sigma = \left(\frac{T}{2\mu a}\right)\frac{n(n^2-1)(n+2-F)}{f_n(q,b/a)} \tag{9}$$

Where $\mu = \rho\nu$ is the dynamic viscosity of the liquid, 'a' is the distance from the center of the sphere to the liquid-air interface, and T is the liquid-air surface tension coefficient and:

$$f_n(q,b/a) = \frac{1}{U_{mn}(a)}n(n+1)\left[a\dot{U}_{mn}(a) - 2U_{mn}(a)\right] - \frac{1}{2}(qa)^2\left[(n+1)D_{mn} - n\widetilde{D}_{mn}\right] \tag{10}$$

Where $U_{mn}(a)$ and $\dot{U_{mn}}(a)$ are single radial complex function, and its derivative respectively, $D_{mn}(a)$ and $\widetilde{D}_{mn}(a)$ are complex coefficients obtained by satisfying boundary conditions.

Also, a dimensionless parameter F, which is the ratio between electric pressure to capillary pressure, is defined as:

$$F = \frac{\varepsilon_0 \Phi_0}{aT} \tag{11}$$

where ε_0 is the permittivity of air and Φ_0 is potential.

Further stability criterion for some limiting cases like a whole liquid globe, liquid layer on a rigid sphere were discussed in the presence and absence of an electric field. One of the limiting cases discussed was a planar liquid layer in which, for simplicity non-viscous liquid layer of thickness h was assumed. By applying the linearized dynamic boundary of the following dispersion relation is obtained:

$$\sigma^2 + k\left(g + \frac{Tk}{\rho}\right) - \frac{\varepsilon_0}{\rho}k^2E_0^2 = 0 \tag{12}$$

After adding the first-order correction to consider the liquid as "slightly" viscous equation becomes:

$$\sigma^2 - 2\nu k^2\sigma + \left(gk + \frac{Tk^3}{\rho} - \frac{\varepsilon_0}{\rho}k^2E_0^2\right)tanh(hk) = 0 \quad (13)$$

and for equation reduces to give the value of σ:

$$\sigma = \frac{Tk^3h^2}{2\mu}\left[1 - \frac{\varepsilon_0 E_0^2}{kT}\right] \quad (14)$$

The model explained that eigenfrequencies for the planar case could be a limiting case of spherical geometry.

In 2011 Forward et al.[68] analyzed the free surface system using a thin wire electrode. A rotating wire electrode with a thin layer of polymer layer deposited on it and using a bath of polymer solution subjected to a high electric field in a direction perpendicular to its axis. Coating of polymer liquid on wire electrode reaches a non-steady state when it is excited using an electrostatic field. These instabilities among the liquid surface follow Plateau-Rayleigh instability. Such instabilities cause the formation of droplets once the de-wetting of the film on wire happens. They investigated in detail two operating regimes (assuming the amount of liquid entrained on the wire is not varying with the applied field). Region one is where the number of jets perturbing from polymer surface, and hence productivity is limited by Plateau-Rayleigh instability depends on operating parameters and system geometry. Part two is where the applied electric field is limiting the number of jets.

For limited entrainment regime, estimating the amount of liquid entrained productivity is given by the following equation:

$$P_E = \pi\Omega Cr^2[(aCa^b + 1)^2 - 1] \quad (15)$$

C(mass/volume) is polymer concentration, Ω(degrees/sec) is rotation rate, r is the radius of capillary. On the other hand, productivity for the field-limited regime for a given geometry was estimated using the following equation:

$$P_F = V_d \Omega C n_J = \frac{\pi \lambda r^2 C}{t_J} [(aCa^b + 1)^2 - 1] \frac{\int_{\phi_1}^{180^0 - \phi_1} n_c\left(E_w(\phi')\right) d\phi'}{360^0} \quad 16)$$

Where V_d is the volume of the droplet, E_w is the electric field on the wire, and $n_J$is the linear jet density distribution function for each rotation. The center-to-center distance between the droplets was observed to be decreasing with an increase in the applied field as follows:

$$\lambda = \frac{2\pi a_0}{0.0028 V_A ppl + 0.50} \quad (17)$$

The model tries to explain the problems in the process of liquid entrainment on an entity when it passes through an interface between two liquids, jet launching by electrostatic forces, and perturbations of liquid films. Further discussion in paper explains how capillary and bond number plays a crucial role in liquid entrainment. On the one hand, the capillary number measures the relation between surface force and viscous force, whereas the bond number is the measurement of the relation between the surface force and gravitational force. Stimulations for spherical geometry performed by Geller et al.[69] along with several other investigators [70,71] revealed that liquid entrainment for small Reynolds number depends more rigidly on the capillary number rather than the Bond number. Extending this analogy to a cylindrical system (thin wire in the given model) film of liquid entrainment was verified experimentally to be dependent on capillary and bond numbers. Goren et al.[72] studied the problem associated with de-wetting using dispersion relation that related the rate of growth of infinitesimal periodic waves of annular liquid films. This model verified that droplet forming jets on the wire is controlled by the fast-growing disturbance with condition satisfying wavelength parameter ($2\pi a_0/\lambda$=0.69) for all liquids irrespective of viscosity,

and it depends very weakly on Ohnesorge number ($Oh = \eta/(\rho\gamma r)^{0.5}$). The wavelength parameter was also observed to be increasing linearly with the applied electric field due to the influence of charges on the surface of the liquid used. Hohman et al.[73,74] studied a general theory for electrodynamics valid for the charged fluid jet that considered the struggle between whipping instabilities and varicose. Although the study was performed on Newtonian fluids, several investigators further used this theory to explain the non- Newtonian fluids under non-isothermal conditions.[75,76] However, this model works for conducting liquids, but most of the polymeric solutions we use are not perfectly conducting and are termed as "leaky dielectrics." Leaky dielectrics induce a finite ionic charge density at their interfaces with other fluids. The local electric field gets modified by the ionic charges at interfaces, resulting in electrical stresses different from those in ideal conductors/dielectrics. Hence in the wire electrode model, the jet initiation critical field was observed to be different from the calculated value by a factor of two, which confirms that more extensive work is needed to be done to understand the "how" for a given fluid and its liquid properties effect on the critical electric field.

In 2010 Tang et al.[77] showed that in free surface splashing electrospinning, fiber morphology does not depend on individual processing parameters separately but a combination of them. In 2015 Nurwaha et al.[78] studied splashing electrospinning, spiral coil electrospinning, and rotary wires electrospinning methods to understand how different spinning parameters affect the spinning process and, more importantly, fiber productivity and uniformity. We have discussed in this review that how each of the process parameters, whether it is the liquid entrainment, electric field, or geometry change, causes changes in fiber morphology. For many applications, uniform fibers are needed implying that uniformity of fiber diameter is the most substantial property of electrospun fibers. Hence, the study focused its analysis of fiber diameter for all three types of free

surface electrospinning for different combinations of spinning parameters. Findings confirmed that the parameter like spiral distance has a little impact on fiber morphology, whereas factors like coil and wire diameter had a significant impact on fiber productivity but had only a slight influence on fiber diameter. Since the existing most developed spinning models are for specific polymer-solvent solutions, it is difficult to establish a relationship between fiber morphology and spinning parameters. A considerable approach should be made to understand how fiber morphology and fiber quality is affected by the properties of the polymer solution and its solvent. Current studies confirm a promising future in developing free surface electrospinning geometries where more control is possible to get desired fibers. The following section provides an overview of the most recent developments in the field of free surface electrospinning instrumentation.

1.5.2. Developed free surface configurations

The emerging field of free surface electrospinning has been proliferating since 2009 with several novel designs with a higher production rate and more versatility to produce sub-micron sized fibers from polymer solutions.[79–81] Gorga and Clarke et al. developed a parallel plate along with an edge plate free surface setup. According to them, the electric field gradient is an essential factor for the self-initiation of cones from a free surface. Based on their calculations, the parallel plate design does not produce enough field gradient on the center of the plate, while the gradient is more uniform in an edge-plate design. They also showed that the production rate for the edge-plate design is five times greater than conventional needle-based electrospinning.[25] In another series of studies done by this group, a bowl-shaped setup as a spinneret with a circular collector all around the bowl was developed to produce fiber from the free surface of the bowl filled with the polymer solution. The sharp edge of the bowl performs like a needle in terms of the electric field strength. The bowl is filled with the solution, and once the high voltage is applied, several

cones are formed spontaneously from the rim of the bowl within a few seconds, which ultimately forms the nanofiber jets. The voltage was initially high to favor the cone formation process. Subsequently, it lowers to an operating voltage for stable continuous operation. Figure 1.4.[20–23]

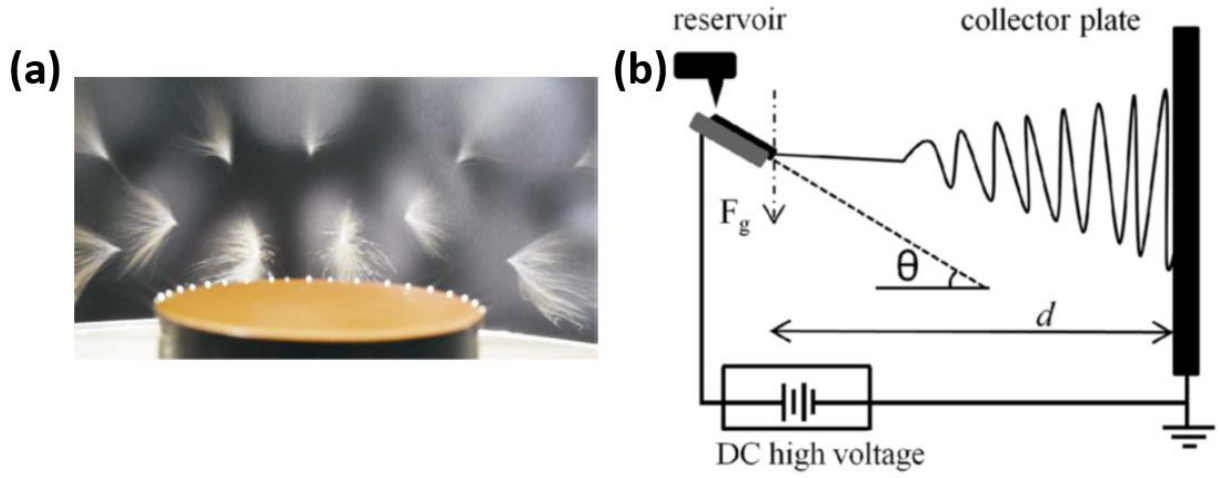

Figure 1.4. (a) Bowl and (b) edge-plate free surface electrospinning design.20,25 Reproduced from Ref. 20 and 25, with permission from IOPScience and Elsevier.

In a work done by Lin et al.[82], slot spinnerets were developed with four different line shapes: straight, rectangle, triangle, and curved. It showed that the slot line shape plays a vital role in affecting fiber diameter, productivity, and uniformity of the product. Compared to the other slots studied, the curved slot yields higher productivity and more consistency due to the higher intensity of the electric field with more uniformity. Figure 1.5

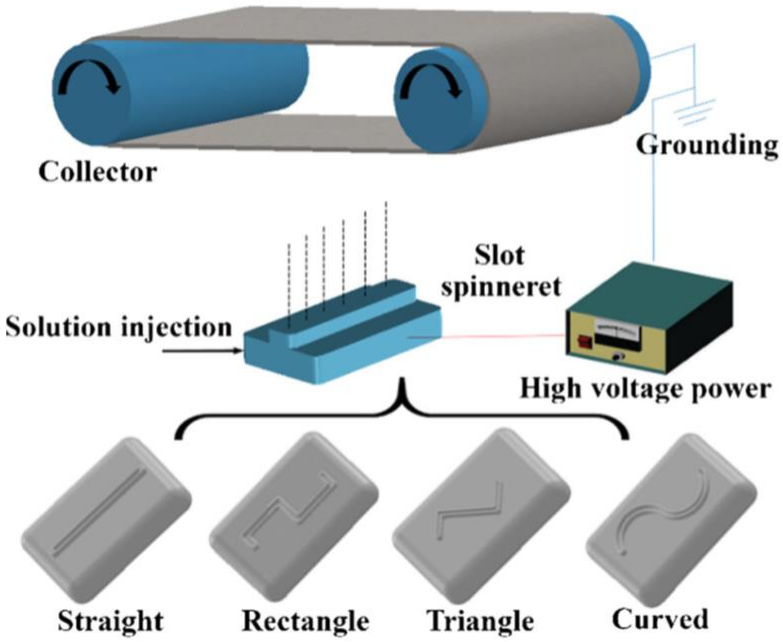

Figure 1.5. Schematic diagram of the slot free surface electrospinning with four different slot shapes as the spinneret. Reproduced from Ref. 82, with permission from Springer Nature.

Wu and Lin et al.[83] proposed a new concept to intensify the electric field near a free surface reservoir of the polymer solution, which eventually produces nanofibers. A non-conductive rod is moved above the solution reservoir at a very close distance to the reservoir to strengthen the electric field. The conductivity (as mentioned, a non-conductive rod is used to avoid discharge) and the speed of the rod movement are the two key factors that affect the cone formation process in this design. Figure 1.6

Chase and coworkers[84] designed a setup and produced fibers from the free surface of the rods containing two metal rods located 6 cm apart with a parallel collector. According to them, a critical factor in this design is the distance of rods to the collector, in which by increasing the distance, the fiber diameter decreases due to increased time and distance for the jet to stretch while moving toward the collector. Figure 1.7

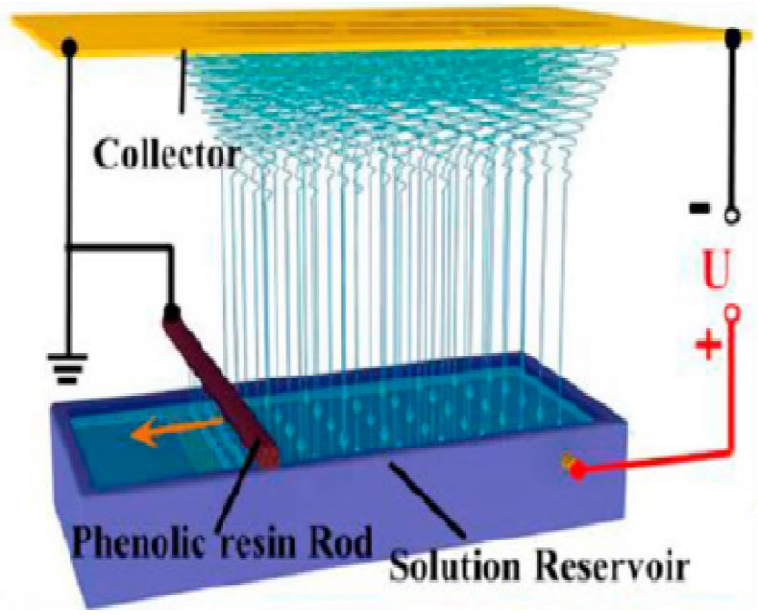

Figure 1.6. Schematic diagram of the rod-assisted free surface electrospinning. Reproduced from Ref. 83, with permission from IOPScience.

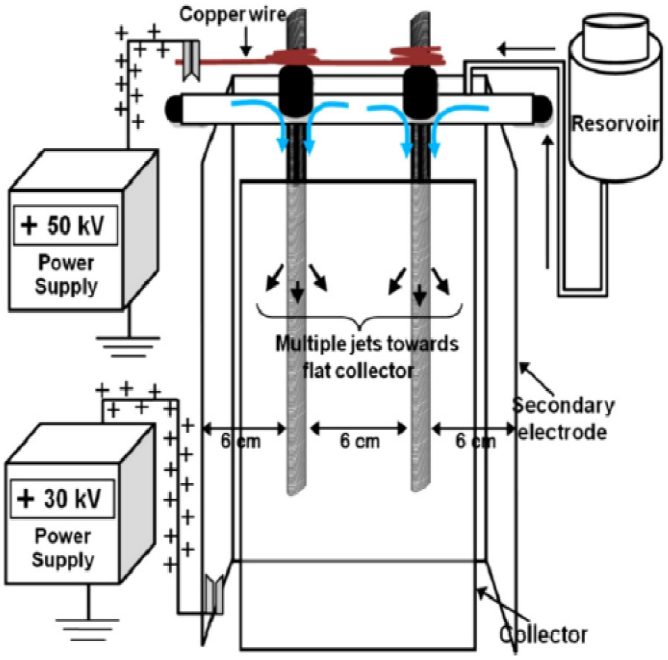

Figure 1.7. Schematic design of the parallel rod free surface electrospinning.84 Reproduced from Ref. 84.

There are a few designs in which the spinneret part of the setup is a moving object, usually in a bath of the polymer solution. The main factor affecting the fiber formation, the diameter, and the uniformity of the product is the speed of the moving part, which determines the thickness of the entrained layer of the solution on the moving spinneret. The moving spinneret free surface electrospinning generally falls into two categories. The first category is the one in which by rotating a cylinder or a disk in a solution bath, a thin film forms on the surface, and the fibers are formed directly from the thin film.[77,81,85,86] In the second category, the moving spinneret is a thin wire electrode[68] or a spiral coil[47], which rotates in a bath of a solution, and once a thin film entrains the wire droplets form due to the Plateau-Rayleigh instability which subsequently turns into jets. Figure 1.8

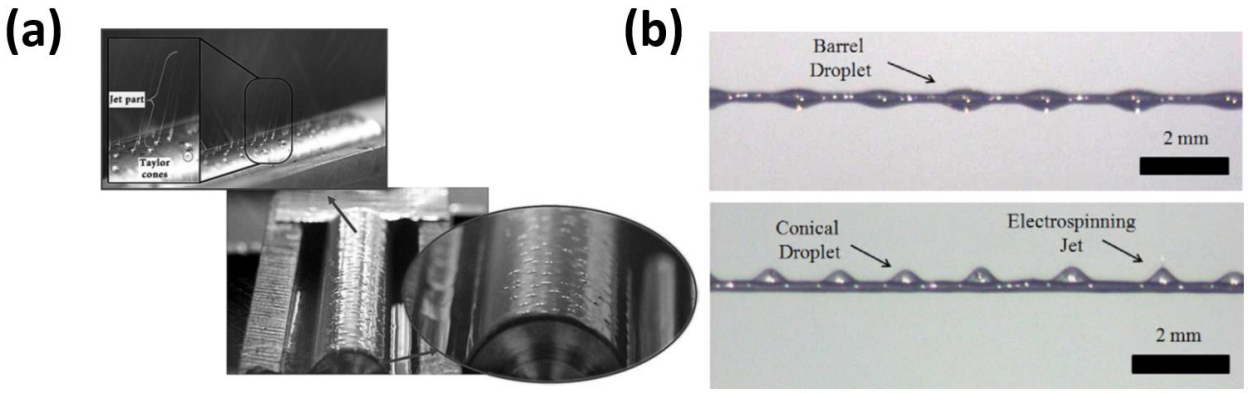

Figure 1.8. (a) Schematic of a rotating surface in a bath of solution, (b) rotating wire and the droplet formation. Reproduced from Ref. 68 and 85, with permission from Elsevier and SAGE.

1.5.3. Ability to produce core-shell fibers and nanocomposites from free surface electrospinning

Core-shell fibers are the structure in which the exterior of the fiber is made from a different material than the interior. The increasing need for making core-shell fibers goes back to their broad application scope, including scaffolds for tissue design[87] where less biocompatible material but usually of higher mechanical properties is used as the core part, isolating a sensitive component

from a highly reactive environment, drug delivery in which a substance needs to release on a schedule to a specific receptor and to add micro or nanoscale particles to the fiber structure for reinforcement, or continuous pharmaceutical manufacturing.[88,89,90] Electrospinning has been an up-and-coming method for producing controllable nano or microstructures. Co-axial electrospinning is one of the highly applicable methods for fabricating core-shell fibers in which two different materials are pumped separately through the co-axial spinneret, which is subsequently drawn by the force of the electric field toward the collector.[91,92] However, the conventional technique of co-axial electrospinning suffers from a low production rate, which makes the production of these fibers challenging at a commercial scale. There are a few kinds of research on producing core-shell fibers from a free surface of a polymer solution with a much higher production rate. Rutledge et al.[93] used a wire electrode free surface electrospinning setup. The solution bath contains the two materials of the core and the shell, which both entrain the wire once it is moving and passing the bath of a polymer solution. A core-shell droplet forms on the wire, and these droplets result in fibers. To make a final core-shell structure, the more viscose and conductive solution should be on the bottom layer to ensure that the more viscous liquid will form the jet first and subsequently, the less viscous layer will be entrained with it. Figure 1.9.

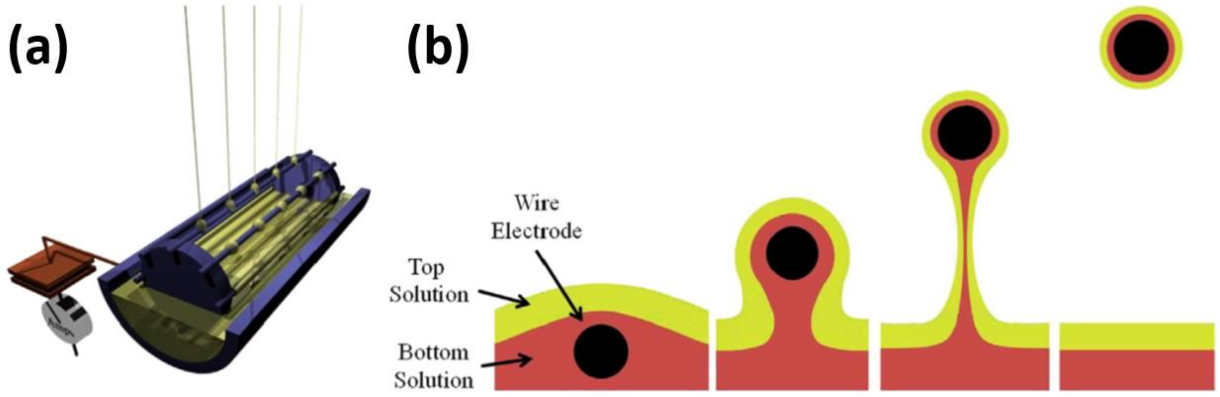

Figure 1.9. (a) Schematic diagram of a wire electrode free surface electrospinning (b) Entrainment of the core/shell droplets by the wire electrodes. Reproduced from Ref. 93, with permission from Elsevier.

Pham et al.[94] developed a slit-surface design for producing core-shells, and they showed that the production rate could be scaled to 1 L/hr for the first time to this magnitude. Figure 1.10

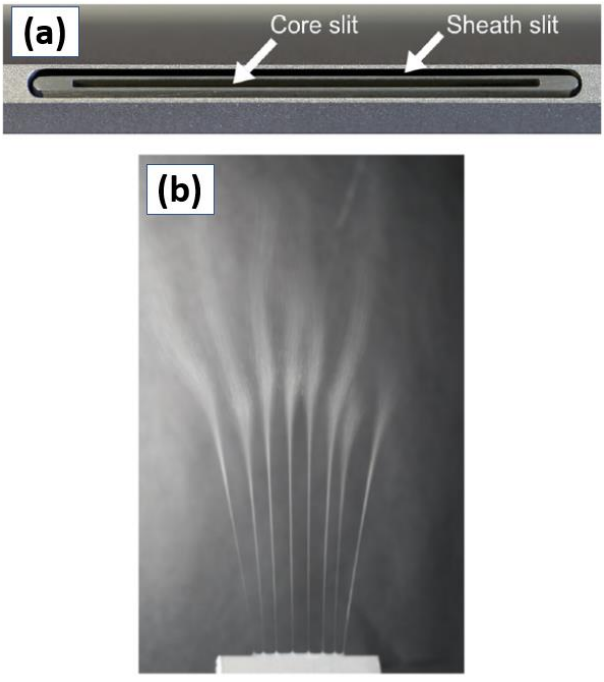

Figure 1.10. (a) Slit surface design for fabricating core/shell fibers. (b) Multiple jets spinning simultaneously from the slit surface. Reproduced from Ref. 94, with permission from PLOS.

Buzgo et al.[95] developed a simple unconstrained setup for producing core-shell fibers in which the two materials float over on top of each other without any barrier in between. Figure 1.11-a Qin and coworkers developed a pyramid-shaped design and used it for making core-shell fibers[93,96]. Figure 1.11-b Trout et al.[97] explored the possibility of adding microparticles to the fibers produced from free surface electrospinning. The results showed that the final fiber quality and diameter is independent of the microparticle showing that any microparticle can be used to make nanofibers with different types of application. Gregr et al.[98] studied the effect of adding carbon nanotubes to the solution. According to them, nanotubes can be pulled out of the solution in the self-initiation of the jetting process from a free surface.

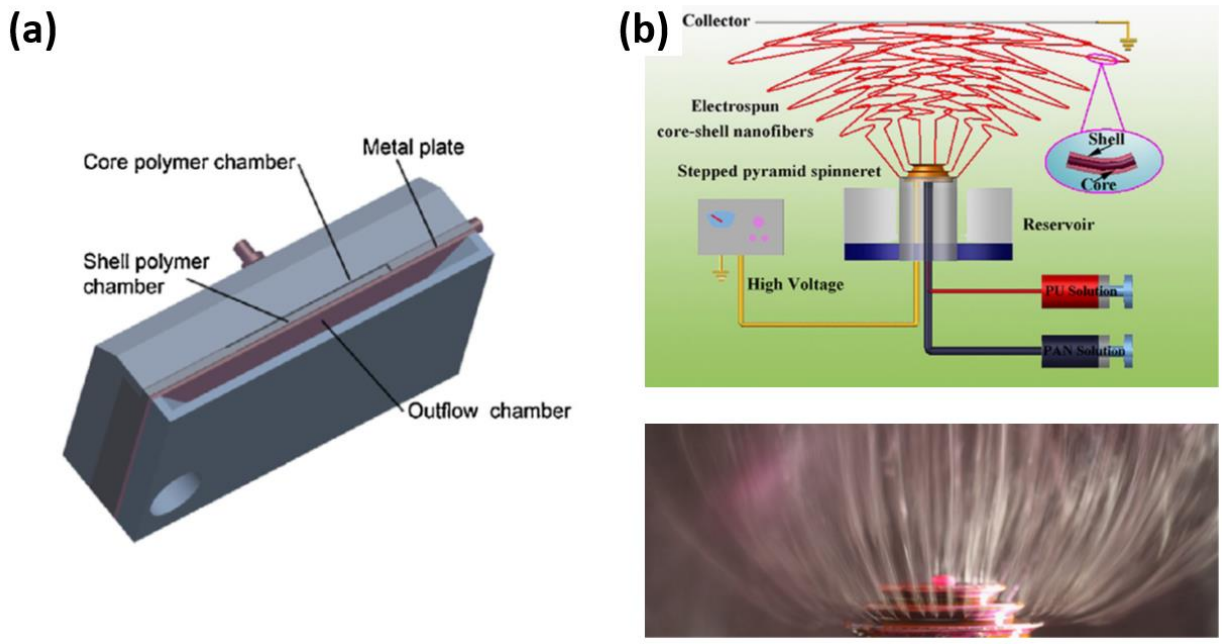

Figure 1.11. (a) Bilayer design for core/shell fiber fabrication, (b) Pyramid free surface electrospinning design. Reproduced from Ref. 95 and 96, with permission from Elsevier.

Overall, free surface electrospinning is a promising technique to commercialize electrospinning of nanofibers with a much higher production rate. However, very few researchers

have studied polymer melts in a free surface setup. The following sections in this paper review the latest developments of the free surface design in melt electrospinning.

1.6. Application of Free Surface Method in Melt Electrospinning

A few numbers of free surface melt electrospinning setups have been developed to overcome some existent challenges of this technique. The following subsections introduce these new configurations and setups.

1.6.1. Unconfined Edge Melt Electrospinning

Gorga and Clarke et al.[24] have developed an unconfined melt electrospinning setup in which they used an edge-plate as a spinneret that can mimic the conventional needle-based technique in terms of sharpness and electric field. Self-initiation of the cones happens within a few minutes of the process on the edge of the plate, and subsequently, ejecting cones made fibers. This method eradicates the hardship of pumping a highly viscous fluid, polymer melt, through a tiny nozzle. They showed that under suitable conditions, fibers with an average diameter of 5 μm and a production rate of 0.5 g/h can be fabricated. Figure 1.12

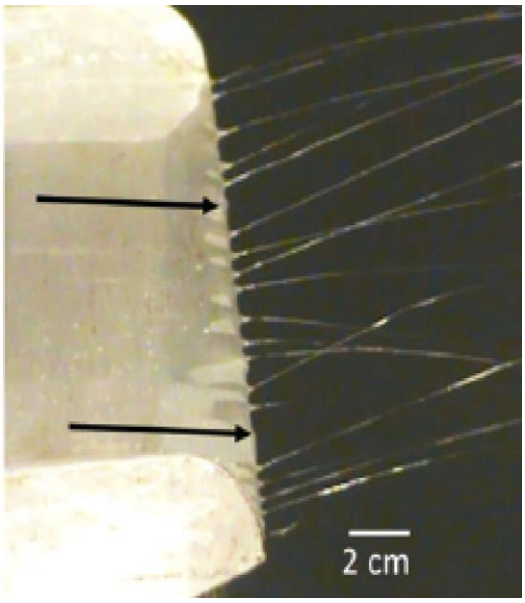

Figure 1.12. Unconfined edge-plate setup of melt electrospinning. Reproduced from Ref. 24, with permission from IOPScience.

1.6.2. Melt Differential Electrospinning (MD)

Yang et al.[40] developed a needleless MD electrospinning. Figure 1.13 In this mechanism, extrusion of the polymer occurs from the umbellate nozzle. This extrusion occurs from the thin layer of the polymer melt forming at the circumferential surface of the nozzle. Finally, as the high voltage is applied, several jets are self-initiated on the rim of the nozzle, moving towards the collector. The inter-jet distance depends on the electric field strength, melt viscosity, and material properties. By increasing the high voltage and hence field strength, the self-organizing differential effect becomes more vigorous. Another study done by this group, showed that the inter-jet distance decreased with the decrease of spinning distance at a fixed voltage of 40 kV. When the electric field was constant at 5 kV/cm, by increasing the spinning distance up to 7 cm, the inter-jet distance decreased. With longer distances up to 13 cm, the inter-jet distance was constant. By simulating the electric field between nozzle and collector, the study showed that the maximum electric field strength happens at the rim of the nozzle (the sharp edge), and it increases with the increase of

spinning distance. In this study, they monitored the effect of Polypropylene (PP) viscosity on inter-jet distance by changing the nozzle temperature (T). By increasing temperature from 190 °C to 280 °C, the inter-jet distance decreased from 7 mm to 4.4 mm until T=230 °C and then remained unchanged, showing a finite reduction in viscosity is useful for scale-up production.[41]

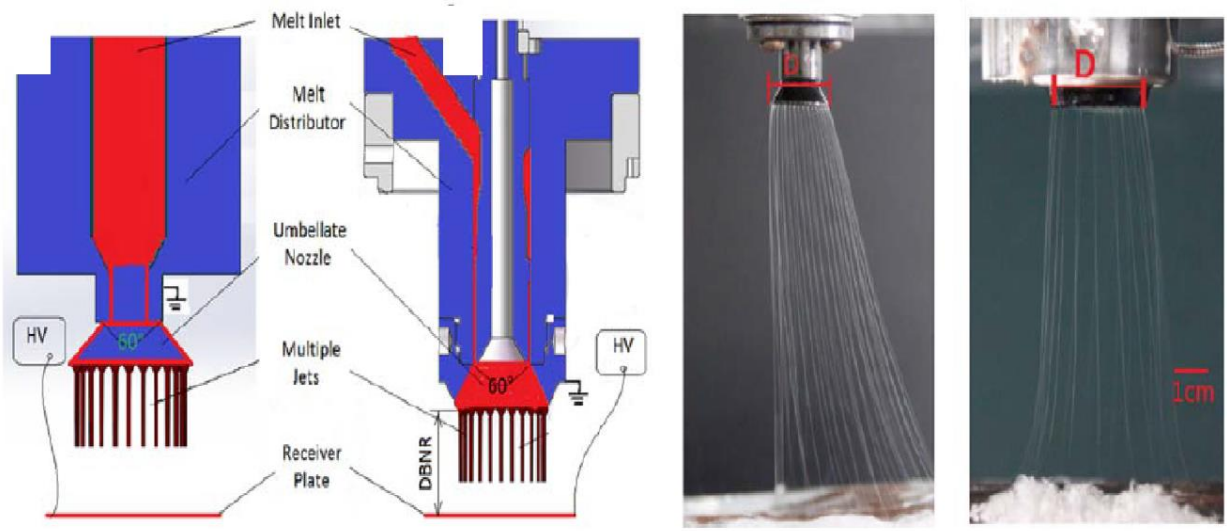

Figure 1.13. Melt differential setup with two different nozzles. Reproduced from Ref. 41, with permission from John Wiley and Sons.

In another work done by Yang et al.[61], they used an MD technique coupled with airflow and a ring-like electrode between nozzle and collector. Figure 1.14-a They produced the PP fibers with a smooth surface and with a diameter of 600 nm-6 µm. In another work by this group, they showed that the hollow electrode caused superfine fibers. After simulating the electric field by finite element method (FEM), they found that there is also an electric field under the electrode for the inner hole, which helps the jet stretch further to be longer than that. The maximum electric field is at the electrode's sharp ring edge, which is not a function of the inner hole diameter.[56] In another work, Yang et al.[39] used the produced PP web for oil cleanup via sorption in which they observed that the sorption capacity was 6-7 times that of melt-blown nonwoven. In another study, they fabricated a composite membrane in which PP was produced by melt electrospinning (average

fiber diameter=2 µm), which was used as a base layer for solution electrospun PVA. This is an efficient method for a microfiltration membrane having both high flux and high rejection ratio.[99]

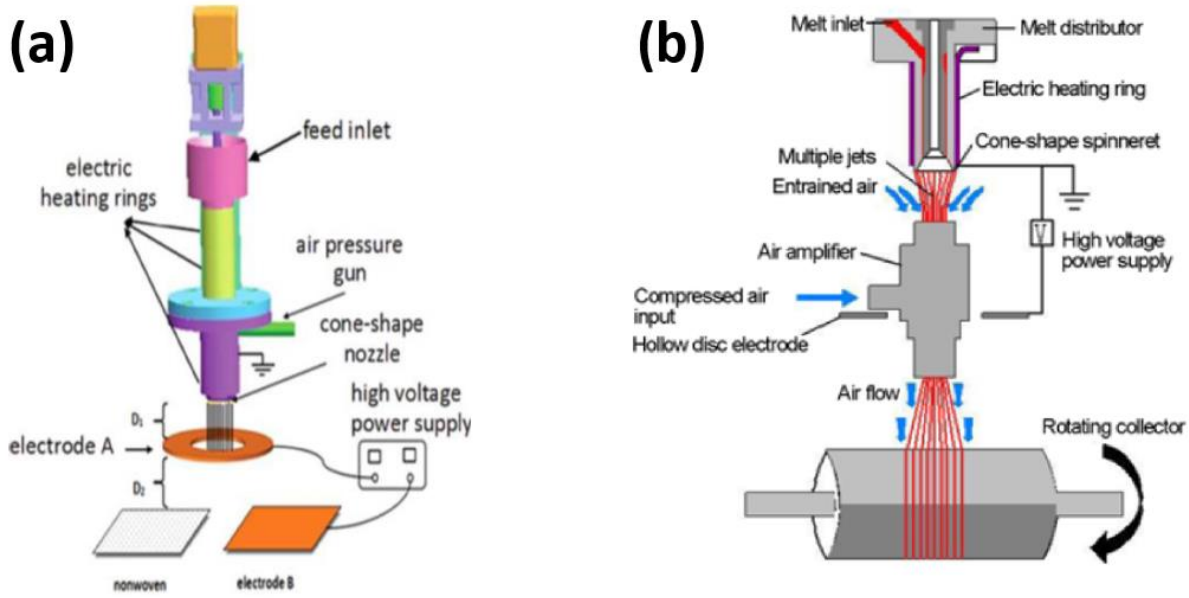

Figure 1.14. (a) Melt differential electrospinning with hot airflow system and ring-like electrodes, (b) Air-suction assisted melt differential system. Reproduced from Ref. 100 and 45, with permission from IOPScience and Springer, respectively.

In another study by Yang et al.[45], they developed an air-suction method coupled with MD electrospinning with more promising results than other MD methods. In this method, the fibers are stretched further due to the driven airflow, and the collector and spinneret are separated so that the fibers do not interfere with the rebounded air; hence fiber diameter distribution gets narrower. Figure 1.14-b

1.6.3. Disc Needleless Melt electrospinning

In this method, Lin et al.[57] used a rotating metal disc submerged in a polymer melt reservoir below it as a fiber producer (Figure 8). Both the tank and the disc were heated to keep the working temperature. Two iron and aluminum (Al) discs were used, and the fibers diameter obtained by the iron disc was about 8.69 µm, whereas it was 3.31 µm with a narrower distribution for the Al

disc. The heat loss compensation was more relaxed and faster due to the higher conductivity of the Al. One drawback of this method that could have potentially stopped it from further development was the considerable heat loss by the rotation of the disc in the reservoir. Figure 1.15

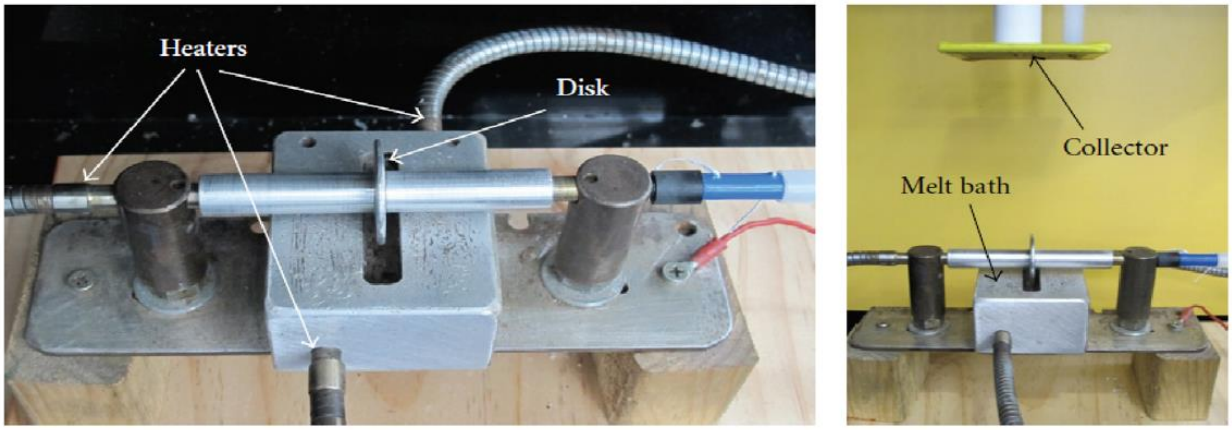

Figure 1.15. Disc melt-electrospinning setup. Reproduced from Ref. 56, with permission from Hindawi.

1.6.4. Slit rod melt electrospinning

A significant parameter in the melt electrospinning system is the design of the spinning and collector electrodes. The shape of the spinning electrode determines the electric field distribution in the spin line region. As the electric force is the only force applied to the jet while stretching in the spin line region, it is essential that all the electrostatic force of the electric field concentrates in the spin line region. In a study done by Komarek et al.[99], two different emitting electrodes were studied. A rod-type electrode used in this method is shown in Figure 1.16-a. In this method, a polymer is fed to the top of the rod-shaped electrode in the form of pellets or powder, molten and spun from the free melt surface. Advantages of this type of electrode are low consumption of the polymer and simplicity of the process. The second electrode was a 'cleft spinner,' shown in Figure 1.16-b. In this type of electrode, the polymer melt is supplied to the

linear spinning cleft from the heated piston reservoir. Advantages of this electrode are the relatively more straightforward polymer feeding and the possibility for upscaling.

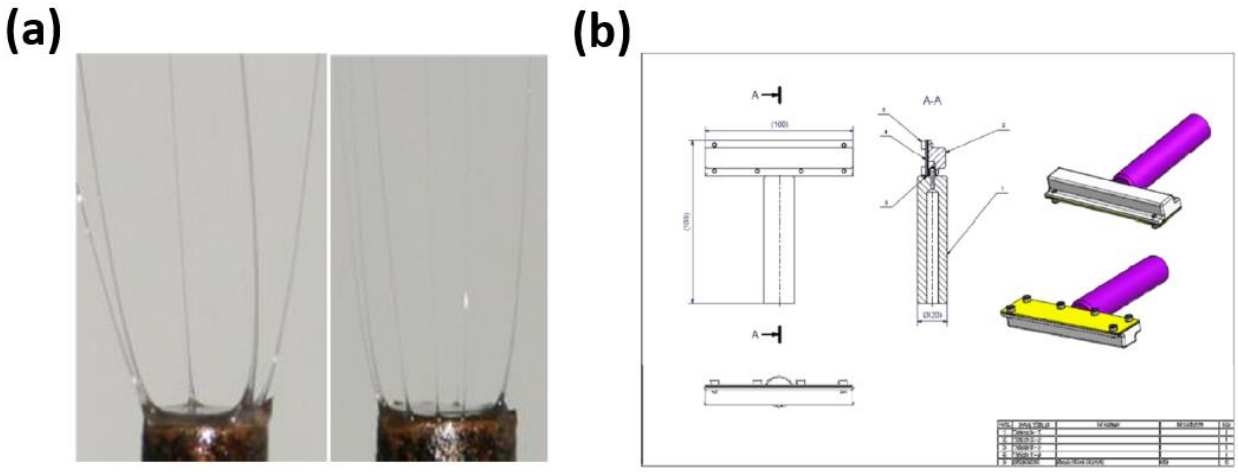

Figure 1.16. (a) Emitting electrode, the 'rod' type, and the inter-jet distance (b) Emitting electrode, the 'cleft' type. Reproduced from Ref. 99, with permission from SJR.

1.7. Conclusions

Many applications exist for which thermoplastic (i.e., highly entangled commercial polymers) mesoscale fibers (< 2 μm diameter) are highly desirable. Most of the well-developed electrospinning techniques utilize a solvent to prepare a spinnable fluid, while attractive thermoplastic materials (such as polyethylene and polypropylene) are not readily soluble. Therefore, melt electrospinning plays a vital role as a method of producing fibers directly from polymer melts. The advantages of this technique are enabling access to a wide range of materials as well as its innate "green" nature – the ability to process without environmentally harmful organic solvents. However, while traditional needle melt electrospinning is the most direct pathway to form such mesoscale fibers, this technique is notoriously unpopular due to processing issues such as frequent clogging, the severe difficulty in pumping high viscosity fluids at low feed

rates, obstacles in generating jetting from highly insulating materials, and the relatively large diameter of the resultant fibers. Therefore, needleless electrospinning is an alternative way of electrospinning suitable for polymer melt which, while maintaining the same quality as the needle-based method, is more productive and more comfortable to handle. This paper reviewed the electrospinning from a free surface, which brings in many fundamentals in physics. In general, electrospinning is balancing the different forces acting on the fluid and different geometrical parameters affecting the process to produce the desired fibers. General theoretical explanations of a free surface electrospinning process become complicated; hence investigators generally talk about electrospinning phenomena for a specific geometry. Most of the theories discussed neglect some critical effects like the interaction of waves on 2-D liquid surfaces, wave interference, viscoelasticity, and electrical forces for leaky dielectrics. To control the fiber morphology, one needs not only a detailed theoretical analysis of all these effects but also systematic experimental verification of the spinning phenomena. To make free surface melt electrospinning a viable process, researchers must focus on the key fundamental parameters affecting the spinning and final fiber morphology.

1.8. Motivation and Objectives

Melt Electrospinning is a sustainable candidate as an alternative approach for melt processing techniques of nonwoven manufacturing. For melt electrospinning to become more accessible, ample research avenues exist that have been unexplored to this date. The research presented in this Ph.D. dissertation aims to identify the major limitations of melt electrospinning and provides sustainable solutions backed by fundamental and scientific standpoints. It is well-known that achieving sub-micron scale fibers from melt electrospinning is extremely challenging.

While part of this is due to the high viscosity nature of the melt, the lack of control over the process parameters is another setback that needs major consideration. Although there has been a good deal of research in proposing strategies to control the fiber diameter, little work has been done to identify the behavior of a melt electrospinning jet in the spin line, especially in a free surface platform, that directly affects the final product diameter and morphology. Likewise, little work has been performed to develop a mechanistic correlation between the process parameters that affect the fiber diameter and the structure/properties of the fibers. Hence, the overall objectives of this research are to provide an understanding of the best mechanism for fiber diameter reduction, the origin of its effectivity, and its effect on the final properties of the fibers. Specifically, the objectives of this research based on their organization in the dissertation are as follows:

1) To develop a technique where jet behavior and its properties in the spin-line can be monitored in situ. Electrospinning is a complicated process where many factors are directly and indirectly controlling the process. Therefore, being able to develop predictive knowledge about electrospinning can be facilitated by adopting a systematic methodology to directly observe jet behavior in situ. The second chapter of this dissertation introduces an imaging technique that reveals in situ information of the process to fundamentally correlates parameters that contribute to fiber diameter attenuation, namely the solidification of the jet in the spin-line.
2) Thoroughly investigating the strategy of "spin line temperature control" in controlling fiber diameter that has been mostly overlooked by other researchers. Chapter 3 aims to adopt the in situ information of the solidification in the jet versus spin-line temperature profile, obtained in the second chapter, to thoroughly investigate an efficient strategy for fiber diameter reduction in melt electrospinning.

3) Understanding the effect of the spin-line temperature, as an effective parameter to reduce fiber diameter (explored in chapter 3), on the properties and performance of the fibers. In chapter 4, the mechanical and viscoelastic properties of the fibers as an indicator of their performance under use were explored to derive a mechanistic correlation for process-structure-property.

Chapter 5 discusses future research directions for free surface melt electrospinning and examines potential solutions to key research questions remaining in the field.

1.9. References

1. Mercante, L. A., Scagion, V. P., Migliorini, F. L., Mattoso, L. H. C., Correa, D. S. *TrAC - Trends Anal. Chem.*, 2017, **91**, 91–103.
2. Aussawasathien, D., Sahasithiwat, S., Menbangpung, L., Teerawattananon, C. *Sensors Actuators, B Chem.*, 2011, **151**, 341–350.
3. Mao, X., Tian, W., Hatton, T. A., Rutledge, G. C. *Anal. Bioanal. Chem.*, 2016, **408**, 1307–1326.
4. Qin, X. H., Wang, S. Y. *J. Appl. Polym. Sci.*, 2006, **102**, 1285–1290.
5. Bjorge, D., Daels, N., De Vrieze, S., Dejans, P., Van Camp, T., Audenaert, W., Hogie, J., Westbroek, P., De Clerck, K., Van Hulle, S. W. H. *Desalination*, 2009, **249**, 942–948.
6. Agarwal, S., Wendorff, J. H., Greiner, A. *Polymer (Guildf).*, 2008, **49**, 5603–5621.
7. Suwantong, O. *Polym. Adv. Technol.*, 2016, **27**, 1264–1273.
8. Yao, Y., Xu, Y., Wang, B., Yin, W., Lu, H. *Pigment Resin Technol.*, 2018, **47**, 47–54.
9. Ahmed, F. E., Lalia, B. S., Hashaikeh, R. *Desalination*, 2015, **356**, 15–30.
10. Scheffler, R., Bell, N. S., Sigmund, W. *J. Mater. Res.*, 2010, **25**, 1595–1600.
11. Zhmayev, E., Cho, D., Joo, Y. L. *Polymer (Guildf).*, 2010, **51**, 4140–4144.
12. Detta, N., Brown, T. D., Edin, F. K., Albrecht, K., Chiellini, F., Chiellini, E., Dalton, P. D., Hutmacher, D. W. *Polym. Int.*, 2010, **59**, 1558–1562.
13. Lian, H., Meng, Z. *Mater. Sci. Eng. C*, 2017, **74**, 117–123.
14. Brown, T. D., Dalton, P. D., Hutmacher, D. W. *Prog. Polym. Sci.*, 2016, **56**, 116–166.
15. Yarin, A. L., Zussman, E. *Polymer (Guildf).*, 2004, **45**, 2977–2980.
16. Niu, H., Lin, T. *J. Nanomater.*, 2012, **2012**.
17. Jentzsch, E., Gül, Ö., Öznergiz, E. *J. Electrostat.*, 2013, **71**, 294–298.

18. Miloh, T., Spivak, B., Yarin, A. L. *J. Appl. Phys.*, 2009, **106**, 114910.

19. Li, J., Gao, F., Liu, L. Q., Zhang, Z. *Express Polym. Lett.*, 2013, **7**, 683–689.

20. Thoppey, N. M., Bochinski, J. R., Clarke, L. I., Gorga, R. E. *Nanotechnology*, 2011, **22**.

21. Thoppey, N. M., Gorga, R. E., Bochinski, J. R., Clarke, L. I. *Macromolecules*, 2012, **45**, 6527–6537.

22. Roman, M. P., Thoppey, N. M., Gorga, R. E., Bochinski, J. R., Clarke, L. I. *Macromolecules*, 2013, **46**, 7352–7362.

23. Thoppey, N. M., Gorga, R. E., Clarke, L. I., Bochinski, J. R. *Polym. (United Kingdom)*, 2014, **55**, 6390–6398.

24. Wang, Q., Curtis, C. K., Thoppey, N. M., Bochinski, J. R., Gorga, R. E., Clarke, L. I. *Mater. Res. Express*, 2015, **1**, 45304.

25. Thoppey, N. M., Bochinski, J. R., Clarke, L. I., Gorga, R. E. *Polymer (Guildf).*, 2010, **51**, 4928–4936.

26. Qin, Y. *Polym. Int.*, 2008, **57**, 171–180.

27. Sas, I., Gorga, R. E., Joines, J. A., Thoney, K. A. *J. Polym. Sci. Part B Polym. Phys.*, 2012, **50**, 824–845.

28. Bao, J., Clarke, L. I., Gorga, R. E. *J. Polym. Sci. Part B Polym. Phys.*, 2016, **54**, 787–796.

29. McCullen, S. D., Stano, K. L., Stevens, D. R., Roberts, W. A., Monteiro-Riviere, N. A., Clarke, L. I., Gorga, R. E. *J. Appl. Polym. Sci.*, 2007, **105**, 1668–1678.

30. Ojha, S. S., Stevens, D. R., Stano, K., Hoffman, T., Clarke, L. I., Gorga, R. E. *Image (Rochester, N.Y.)*, 2008, 2509–2513.

31. Ojha, S. S., Stevens, D. R., Hoffman, T. J., Stano, K., Klossner, R., Scott, M. C., Krause, W., Clarke, L. I., Gorga, R. E. *Biomacromolecules*, 2008, **9**, 2523–2529.

32. McCullen, S. D., Stevens, D. R., Roberts, W. A., Clarke, L. I., Bernacki, S. H., Gorga, R. E., Loboa, E. G. *Int. J. Nanomedicine*, 2007, **2**, 253–263.

33. McCullen, S. D., Miller, P. R., Gittard, S. D., Gorga, R. E., Pourdeyhimi, B., Narayan, R. J., Loboa, E. G. *Tissue Eng. Part C. Methods*, 2010, **16**, 1095–105.

34. Mccullen, S. D., Ramaswamy, S., Clarke, L. I., Gorga, R. E. *Wiley Interdiscip. Rev. Nanomedicine Nanobiotechnology*, 2009, **1**, 369-390.

35. Dasdemir, M., Topalbekiroglu, M., Demir, A. *J. Appl. Polym. Sci.*, 2013, **127**, 1901–1908.

36. Nayak, R., Padhye, R., Arnold, L. Melt-electrospinning of nanofibers, Elsevier Ltd., 2016.

37. Malakhov, S. N., Chvalun, S. N. *Russ. J. Gen. Chem.*, 2017, **87**, 1364–1370.

38. Deng, R., Liu, Y., Ding, Y., Xie, P., Luo, L., Yang, W. *J. Appl. Polym. Sci.*, 2009, **114**, 166–175.

39. Li, H., Wu, W., Bubakir, M. M., Chen, H., Zhong, X., Liu, Z., Ding, Y., Yang, W. *J. Appl. Polym. Sci.*, 2014, **131**.

40. Yang, W., Li, H. *IOP Conf. Ser.: Mater. Sci. Eng.*, 2014, **64** 012013

41. Li, H., Chen, H., Zhong, X., Wu, W., Ding, Y., Yang, W. *J. Appl. Polym. Sci.*, 2014, **131**.

42. Haoyi, L., Weimin, Y., Hongbo, C., Jing, T., Pengcheng, X. *AIP Conf. Proc.*, 2016, **1713**.

43. Nazari, T., Garmabi, H. *J. Appl. Polym. Sci.*, 2016, **133**.

44. Shen, Y., Liu, Q., Deng, B., Yao, P., Xia, S. *Fibers Polym.*, 2016, **17**, 1227–1237.

45. Chen, H., Li, H., Ma, X., He, W., Tan, J., Yang, W. *Fibers Polym.*, 2016, **17**, 576–581.

46. Doustgani, A., Ahmadi, E. *J. Ind. Text.*, 2016, **45**, 626–634.

47. Uthaman, N., Majeed, A., Pandurangan *E-Polymers*, 2006, 1–9.

48. Mota, C., Puppi, D., Gazzarri, M., Bártolo, P., Chiellini, F. *Polym. Int.*, 2013, **62**, 893–900.

49. Zhou, H., Green, T. B., Joo, Y. L. *Polymer (Guildf).*, 2006, **47**, 7497–7505.

50. Dalton, P. D., Grafahrend, D., Klinkhammer, K., Klee, D., Möller, M. *Polymer (Guildf).*, 2007, **48**, 6823–6833.

51. Dalton, P. D., Joergensen, N. T., Groll, J., Moeller, M. *Biomed. Mater.*, 2008, **3**.

52. Kong, C. S., Jo, K. J., Jo, N. K., Kim, H. S. *Polym. Eng. Sci.*, 2009, **49**, 391–396.

53. Lyons, J., Li, C., Ko, F. *Polymer (Guildf).*, 2004, **45**, 7597–7603.

54. Ko, J., Ahsani, V., Yao, S. X., Mohtaram, N. K., Lee, P. C., Jun, M. B. G. *J. Micromechanics Microengineering*, 2017, **27**.

55. Liu, Z., Li, H., Wu, W., Chen, H., Ding, Y., Yang, W. *J. Polym. Eng.*, 2015, **35**, 61–70.

56. Fang, J., Zhang, L., Sutton, D., Wang, X., Lin, T. *J. Nanomater.*, 2012, **2012**.

57. Singer, J. C., Ringk, A., Giesa, R., Schmidt, H. W. *Macromol. Mater. Eng.*, 2015, **300**, 259–276.

58. Liu, Y., Li, X., Ramakrishna, S. *J. Polym. Sci. Part B Polym. Phys.*, 2014, **52**, 946–952.

59. Xie, G., Wang, Y., Han, X., Gong, Y., Wang, J., Zhang, J., Deng, D., Liu, Y. *Ind. Eng. Chem. Res.*, 2016, **55**, 7116–7123.

60. Li, X., Liu, Y., Peng, H., Ma, X., Fong, H. *Mater. Lett.*, 2016, **176**, 194–198.

61. Li, X., Yang, W., Li, H., Wang, Y., Bubakir, M. M., Ding, Y., Zhang, Y. *J. Appl. Polym. Sci.*, 2015, **132**, 1–8.

62. Mirjalili, M., Zohoori, S. *J. Nanostructure Chem.*, 2016, **6**, 207–213.

63. Zhu, M., Han, J., Wang, F., Shao, W., Xiong, R., Zhang, Q., Pan, H., Yang, Y., Samal, S. K., Zhang, F., Huang, C. *Macromol. Mater. Eng.*, 2017, **302**, 1–27.

64. Xu, Y., Yuan, D., Bao, J., Xie, Y., He, M., Shi, Z., Chen, S., He, C., Zhao, W., Zhao, C. *J. Mater. Chem. A*, 2018, **6**, 13359–13372.

65. Cho, H., Min, S. Y., Lee, T. W. *Macromol. Mater. Eng.*, 2013, **298**, 475–486.

66. Kotek, V., Martinova, L., Chaloupek, J., Examiner, P., Lynn, M. 2009, **2**.

67. Lukas, D., Sarkar, A., Pokorny, P. *J. Appl. Phys.*, 2008, **103**.

68. Forward, K. M., Rutledge, G. C. *Chem. Eng. J.*, 2012, **183**, 492–503.

69. Geller, A. S., Lee, S. H., Leal, L. G. *J. Fluid Mech.*, 1986, **169**, 27–69.

70. Lee, S. H., Leal, L. G. *J. Colloid Interface Sci.*, 1982, **87**, 81–106.

71. Stone, H. A. *J. Fluid Mech.*, 1995, **287**, 279–298.

72. Goren, S. L. *J. Fluid Mech.*, 1962, **12**, 309.

73. Hohman, M. M., Shin, M., Rutledge, G., Brenner, M. P. *Phys. Fluids*, 2001, **13**, 2221–2236.

74. Shin, Y. M., Hohman, M. M., Brenner, M. P., Rutledge, G. C. *Appl. Phys. Lett.*, 2001, **78**, 1149–1151.

75. Yu, J. H., Fridrikh, S. V., Rutledge, G. C. *Polymer (Guildf).*, 2006, **47**, 4789–4797.

76. Carroll, C. P., Joo, Y. L. *J. Nonnewton. Fluid Mech.*, 2008, **153**, 130–148.

77. Tang, S., Zeng, Y., Wang, X. *Polym. Eng. Sci.*, 2010, **50**, 2252–2257.

78. Nurwaha, D., Wang, X. *Fibers Polym.*, 2015, **16**, 850–866.

79. Zhang, J., Song, M., Li, D., Yang, Z., Cao, J., Chen, Y., Xu, Y., Wei, Q. *Fibers Polym.*, 2016, **17**, 1414–1420.

80. Jiang, G., Zhang, S., Wang, Y., Qin, X. *Mater. Lett.*, 2015, **144**, 22–25.

81. Guo, C., Zhou, L., Lv, J. *Polym. Polym. Compos.*, 2013, **21**, 449–456.

82. Yan, G., Niu, H., Shao, H., Zhao, X., Zhou, H., Lin, T. *J. Mater. Sci.*, 2017, **52**, 11749–11758.

83. Wu, D., Xiao, Z., Teh, K. S., Han, Z., Luo, G., Shi, C., Sun, D., Zhao, J., Lin, L. *J. Phys. D. Appl. Phys.*, 2016, **49**, 365302.

84. Shin, H. U., Li, Y., Paynter, A., Nartetamrongsutt, K., Chase, G. G. *Data Br.*, 2015, **5**, 41–

44.

85. Yalcinkaya, F., Yalcinkaya, B., Jirsak, O. *Text. Res. J.*, 2017, **87**, 913–928.

86. Ali, U., Niu, H., Aslam, S., Jabbar, A., Rajput, A. W., Lin, T. *J. Mater. Sci.*, 2017, **52**, 7567–7577.

87. Liu, H., Mukherjee, S., Liu, Y., Ramakrishna, S. *J. Appl. Polym. Sci.*, 2018, **135**.

88. Lu, Y., Huang, J., Yu, G., Cardenas, R., Wei, S., Wujcik, E. K., Guo, Z. *Wiley Interdiscip. Rev. Nanomedicine Nanobiotechnology*, 2016, **8**, 654–677.

89. Balogh, A., Domokos, A., Farkas, B., Farkas, A., Rapi, Z., Kiss, D., Nyiri, Z., Eke, Z., Szarka, G., Örkényi, R., Mátravölgyi, B., Faigl, F., Marosi, G., Nagy, Z. K. *Chem. Eng. J.*, 2018, **350**, 290–299.

90. Nagy, Z. K., Balogh, A., Démuth, B., Pataki, H., Vigh, T., Szabó, B., Molnár, K., Schmidt, B. T., Horák, P., Marosi, G., Verreck, G., Van Assche, I., Brewster, M. E. *Int. J. Pharm.*, 2015, **480**, 137–142.

91. Elahi, M. F., Lu, W. *J. Bioeng. Biomed. Sci.*, 2013, **03**, 1–14.

92. Moghe, A. K., Gupta, B. S. *Polym. Rev.*, 2008, **48**, 353–377.

93. Forward, K. M., Flores, A., Rutledge, G. C. *Chem. Eng. Sci.*, 2013, **104**, 250–259.

94. Yan, X., Marini, J., Mulligan, R., Deleault, A., Sharma, U., Brenner, M. P., Rutledge, G. C., Freyman, T., Pham, Q. P. *PLoS One*, 2015, **10**, 1–12.

95. Vysloužilová, L., Buzgo, M., Pokorný, P., Chvojka, J., Míčková, A., Rampichová, M., Kula, J., Pejchar, K., Bílek, M., Lukáš, D., Amler, E. *Int. J. Pharm.*, 2017, **516**, 293–300.

96. Jiang, G., Qin, X. *Mater. Lett.*, 2014, **128**, 259–262.

97. Brettmann, B. K., Tsang, S., Forward, K. M., Rutledge, G. C., Myerson, A. S., Trout, B. L. *Langmuir*, 2012, **28**, 9714–9721.

98. Kostakova, E., Meszaros, L., Gregr, J. *Mater. Lett.*, 2009, **63**, 2419–2422.

99. Komárek, M., Martinová, L. 2010, 10–15.

100. Bubakir, M. M., Li, H., Wu, W., Li, X., Ma, S., Yang, W. *IOP Conf. Ser. Mater. Sci. Eng.*, 2014, 64.

101. Guo, C., Zhou, L., Lv, J. *Polym. Polym. Compos.*, 2013, **21**, 449–456.

CHAPTER 2: A facile LED backlight *in situ* imaging technique to investigate sub-micron level processing

Elnaz Shabani[1, *], Taslim Ur Rashid[1], Russell E. Gorga, Wendy E. Krause
Fiber and Polymer Science Program, Department of Textile Engineering, Chemistry, and Science, Wilson College of Textiles, North Carolina State University, 1020 Main Campus Drive, Raleigh, NC, 27606.
[1]The Authors contributed equally
*Corresponding author: Elnaz Shabani, Email address: eshaban@ncsu.edu

This chapter has been published as a manuscript in the journal Polymer Testing (Elsevier) in 2020.

Abstract

Many laboratory experimental techniques used for investigating fine fluid structure, such as fiber spinning, microfluidic flow, and electrospinning, require high quality images with good contrast. Common processes of observation and image recording rely heavily on highly technical light and camera setups which can be difficult to operate in some processing conditions and expensive as well. Here, we report a facile technique using LED backlight imaging to investigate ultrathin fluid profile in two different processes, melt electrospinning and tubeless siphoning. The setup comprises of a simple LED light source facing toward the camera, directly shining into the camera lens. The object under investigation was placed between the camera and the light source. The high-quality captured images and video recordings enable the precise analysis of the cone diameter and jet solidification in case of melt electrospinning, and extensional behavior profiles for tubeless siphoning. The LED backlight setup with high resolution camera is a useful tool to investigate sub-micron scale dimensions in fiber spinning, microfluidic flow, solution electrospinning, contact angle measurement for surface properties analysis, etc.

Keywords: LED backlighting; imaging; melt electrospinning; tubeless siphoning

2.1. Introduction

In the manufacturing industry, *in situ* measurement is a widespread need for inspecting processing conditions. Many processes need high spatial resolution (from micron to sub-micron) imaging techniques that are viable to localize for in situ imaging. Examples of scientific applications that require such photography are electrospinning, contact angle measurement for surface properties analysis, fiber spinning, extensional viscosity measurement, etc. For example, in melt electrospinning, it is crucial to investigate micron scale dimensions to precisely analyze the jet stability, cone diameter and jet solidification zone, and correlate them to the process parameters such as electric field intensity, plate to collector distance or temperature for optimizing the process. Tubeless siphoning, which is a useful tool to explore extensional flow profile of non-Newtonian fluids, also needs clear visualization of thin siphon line, especially in case of low viscosity fluids. To date, various imaging techniques have been developed and utilized for analyzing industrial processing both qualitatively and quantitatively [1-6]. The most common inspection method uses a camera to acquire two dimensional images of the system under investigation [7]. Matthys reported a flow visualization technique to investigate extensional flow profile for tubeless siphoning of polymeric fluids by using intense ultraviolet (UV) light generated by a pulsed nitrogen laser [3]. The technique was based on the activation of a photochromic dye by illuminating from the side with a very short pulse of UV light focused in a small beam at the location of interest. The photoactivation resulted in the apparition of dark marker lines in the center of the siphoned fluid which allowed to record high speed movies to compute velocities anywhere inside the flow field. Later on, another group of researchers used NMR microscopy to observe the velocity profiles directly at any point of the tubeless siphon column of viscoelastic fluid (polyethylene oxide (PEO) in water) [2]. The technique was efficient to measure the radial profiles

of axial velocity in the siphon flow; however, it was comparatively expensive and not convenient for industrial implementation. While investigating electrospinning jet stabilities for PEO-water, Shin et al. used area backlight to improve the contrast of the images that were taken on conventional film using of high-speed photographic techniques [8]. The technique used multiple equipment arrangement that might not be a feasible to perform in situ measurements. Thoppey et al. used a halogen lamp and/or a light source comprised of a square array of white LEDs to illuminate polymer jets to record images of the electrospinning process of PEO solutions for further analysis [9]. They tinted the polymer solution with a dye to provide enhanced imaging contrast for viewing the jet initiation process and subsequent stabilized jets.

Most of the imaging techniques used by the researchers are either complicated in design or not cost effective. Some setups use dye molecules for improved visualization of the process, which are difficult to implement in large scale industrial setting. Moreover, current methodologies often require a microscope that even though very precise, is not flexible enough to be properly localized for a specific application especially in cases where in-situ photography is needed. In addition, the direct use of light source from the same side of the camera suffers from non-uniform illumination caused by the light source and the surrounding environment. To overcome these problems, in recent years, researchers emphasize using backlight technique for imaging objects or in-line processing [7, 10-13]. In backlight setup, the object is placed between the camera and the light source that enables shining the camera lens directly. Chen et al. presented smartphone supported backlight illumination technique for microfluidic imaging [11]. However, the complicated imaging box system restricts their design from ubiquitous applications. In a recent work, Liu et al. also utilized backlight technique using an incandescent lamp for optical observations of droplet-jet shape to guide adjustments to optimize and maintain fiber diameter in online controlled

electrospinning of PEO solution [13]. However, they used a microscopic lens attached with a single-lens reflex camera to observe and record the process that might not be convenient for universal use and cost effective as well. In a recent study, Wunner et al. used two cameras to capture the flight path and fiber diameter on the collector in a melt electrowriting process [14]. In this technique the first camera was placed at a distance of 100 mm to focus on the region of the fiber flight path and the second camera was a microscopic camera with 10x magnification lens. The images from this technique appear as a dark line in front of an illuminated background with no detailed information of the inside jet. The images were utilized for high throughput analysis of the melt electrowriting process parameters to develop the best processing conditions among the many parameters affecting the jet diameter. The necessity for small distance of the camera to the object and the utilization of the microscopic camera could potentially complexify the setup design in large scale applications.

In this paper we introduce a simple yet versatile photography technique that can be utilized to take in-situ still images from sub-micron scale objects with high resolution that enables post-processes measurements and analysis. Our study aims to develop a simple but accurate tool to acquire both qualitative and quantitative information about the subject. We use a LED lamp as a source of light and a digital single-lens reflex camera (DSLR) or a smartphone for capturing image or video. The capability of this technique is investigated for various areas of research including 1) melt electrospinning, and 2) tubeless siphoning, showing the broad ranges of applicability. For melt electrospinning, images are collected for further analysis on the jet cone size, jet number and jet diameter at the initiation, and the solidification point of the jet during the process. For tubeless siphoning, applicability of the technique to collect high quality images and videos for measuring

extensional behavior of the fluids is investigated. We demonstrate that this simple imaging setup is applicable to a variety of laboratory and industrial processing.

2.2. Methodology

2.2.1. Backlight Setup

The backlighting setup comprises of a light source, namely a LED lamp that is placed in such a way as to directly shine the camera lens. The object is placed between the camera and the light source. The purpose is to signify the edges of the object in the illustration which will ultimately enable us to perform precise dimension analysis for the specific application. (Figure 2.1). We used a simple LED lamp (33 LED Super Bright Wardrobe Lights, Portable Magnetic Stick Wireless, geometry 9.5 inch by 1.5 inch by 0.7 inch, manufacturer: CHNXU). This LED lamp minimizes the environment lighting compared to the translucent lamp used by Liu et al. [13]; hence, the focused light coming from the LED source shines the camera lens effectively. Both a high-quality Canon DSLR (Canon EOS Rebel T5i with 18-135mm EF-S IS STM Lens, single flexible zoom lens, 18.0 Megapixel CMOS sensor, able to take both color and black and white images, pixel pitch: 4.29 µm, pixel area: 18.40 μm^2, and pixel density: 5.43 MP/cm^2) and simple smartphone cameras (Samsung Galaxy J7 Prime; 13 MP Sony Exmor RS, f/1.9 aperture, zoom levels: 4x) have been utilized in this work to show the versatility of this technique with ranges of camera specifications. However, in the case of sub-micron scale dimensions, high resolution cameras will get more precise images.

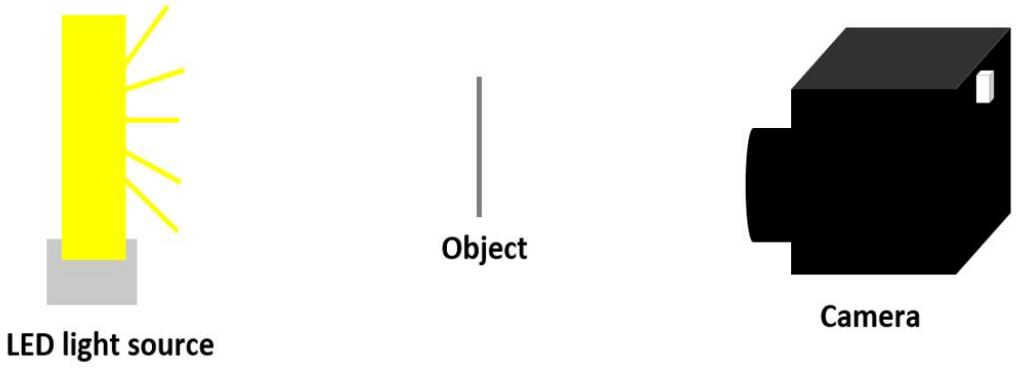

Figure 2.1. Schematic configuration of a backlighting setup. The object is placed in between the camera and the LED light source. The distance between the LED and the object is 10-20 cm, and that between the object and the camera is 10-50 cm.

In the case of the Canon DSLR camera, the settings need to be manually adjusted properly for backlit photography. The three main setting parameters that need to be adjusted are as following: aperture, shutter speed, and ISO (International Organization for Standardization) speed. Aperture is the opening in a lens through which light passes to enter the camera. A larger aperture allows more light to enter the camera. The shutter speed determines how long shutter remains open as the picture is taken. The slower the shutter speed, the longer the exposure time. The shutter speed and aperture together control the total amount of light reaching the sensor. However, for backlit photography, especially in the cases where the object is favored to be isolated from the background, adjusting the aperture to a wider degree (means lower number e.g. f/5.6) and adjusting the light based on the shutter speed is recommended. As the light source is positioned behind the object and is directly lighting the lens, a higher shutter speed, (e.g. 1/1000) is recommended to minimize the exposure of the camera to the light. The third important parameter to be adjusted is the ISO speed which determines the sensitivity of the camera sensors to the light and for this technique is recommended to be adjusted to the lower degrees. The settings that were adopted in this work were: ISO speed: 200, f1/5.6 and shutter speed 1/1000. The camera setting for Samsung

Galaxy J7 Prime is much straightforward. We used automatic mode of the camera with occasional adjustment of the zoom (up to 4x) with manual focusing.

2.2.2. Melt Electrospinning setup

A free surface melt electrospinning setup was utilized to fabricate micron scale fibers of linear low density polyethylene (LLDPE) (granule, ASPUN 6850 Fiber Grade Resin with the melt index of 30 g/min under 190 °C/2.16 kg based on the data sheet provided by the manufacturer; Supplier: Dow Chemical company) [15]. The apparatus consists of an aluminum sharp edge plate and a commercial hot plate (Fisher Scientific, model: HP88857100) to heat up the source plate. The source plate is a hand-made aluminum plate with the surface area of 13.6 x 4.8 cm and edge walls of 1 mm thickness and 0.8 cm height on the sides (with no wall on the sharp edge where fibers are formed). The source plate temperature is set to 190 °C. One side of the source plate is connected to a k-type thermocouple to monitor the temperature of the source plate. The opposite side of the plate is attached to ground wire. The counter electrode consists of a square aluminum plate with the surface area of 30 x 30 cm that is connected to the negative polarity of a high voltage source (Glassman, Model FC60R2). The entire apparatus is placed in a wood chamber with transparent acrylic plastic as front door and top wall to observe the process. The thermocouple reader is placed outside the box, however for the schematic purposes it is shown inside the chamber (Figure 2.2). Figure 2.2 illustrates the schematic design of the melt electrospinning setup.

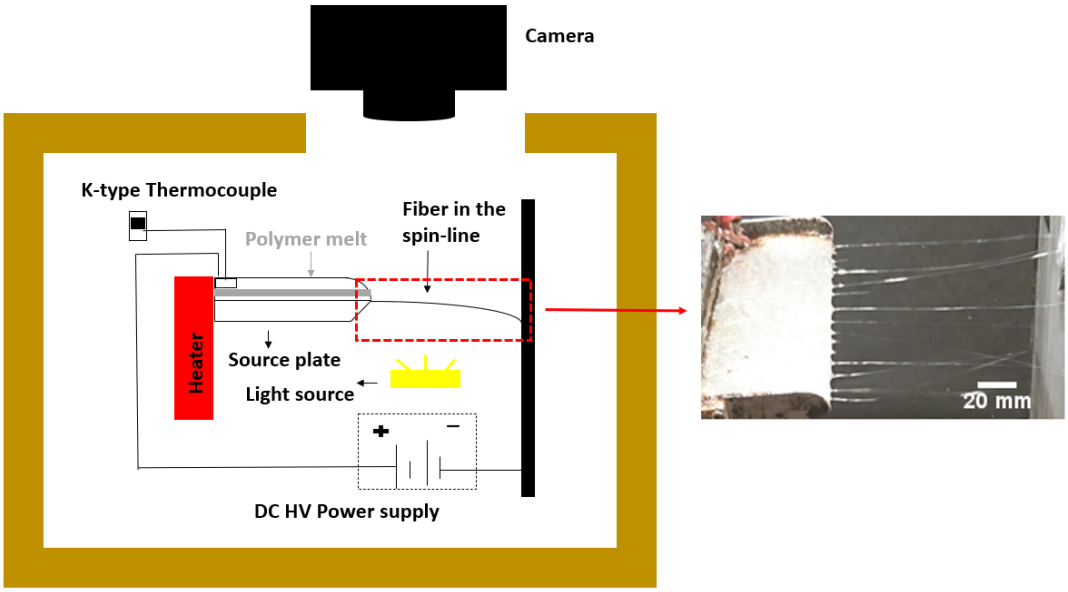

Figure 2.2. Schematic of the melt electrospinning apparatus for PE with backlit photography setup; the light source is placed behind the spinning jets, directly shinning the camera lens. The distance between the LED and the object is 18 cm, and that between the object and the camera is 43 cm. With utilizing this technique *in situ* still images were taken from the process as well as the jets for further analysis on the cone size, jet number, jet diameter at the initiation and the solidification point of the jet as it goes through a phase change during the process. The image is added to illustrate the overview of the spinning location and is taken via a side-lit setup and the phone camera. The side-lit setting illuminates the entire plate and give a better overview of the entire process where the aim is not on the detailed analysis of the jet.

2.2.3. Tubeless siphoning setup

Some non-Newtonian fluids, such as polymer solutions with sufficient entanglements or polymer melts have a special ability to form a tubeless siphon (ductless siphon). Figure 2.3 depicts a set up for tubeless siphoning of 2% (w/w) solution of polyethylene oxide (PEO) (MW 400,000; supplier: Scientific Polymer Products, INC.) in water. When the glass pipette nozzle (connected to a tube and vacuum source) is inserted into the PEO solution, a siphon starts first. The siphoning action continues when the nozzle is raised above the free surface of the fluid. The non-Newtonian viscoelastic stresses, resulting from stretching of the polymer molecules in solution, support the weight of the jet against the gravitational force [16]. This technique has been used to investigate

the extensional properties of the non-Newtonian fluids [3, 17]. Here, an LED backlighting technique is utilized (as illustrated in the Figure 2.3) for the close investigation of the extensional behavior of PEO solution by measuring siphon height and change in siphon diameter with respect to axial distance from the solution surface.

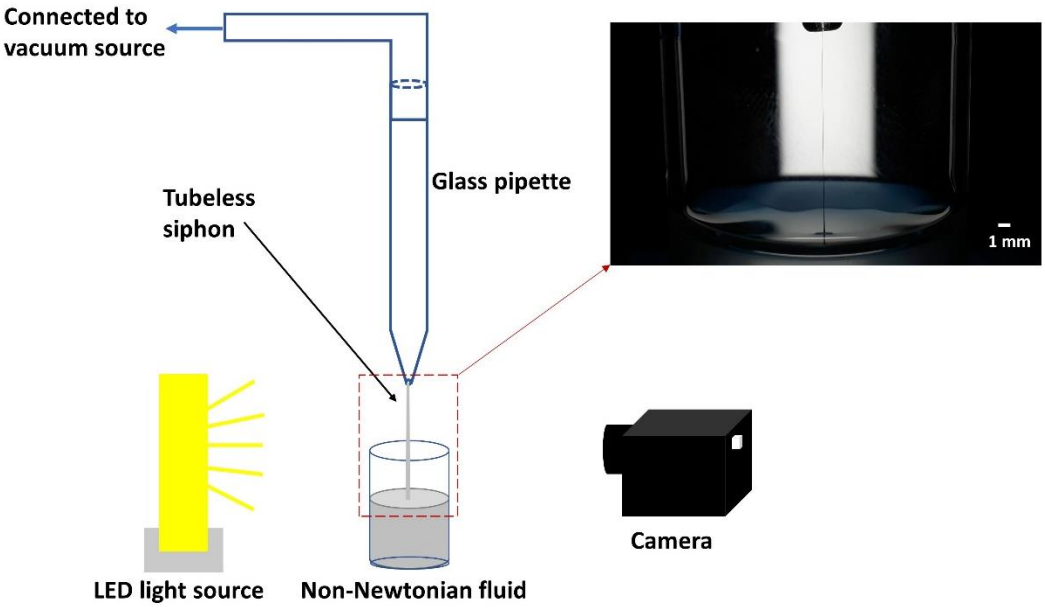

Figure 2.3. Schematic of the tubeless siphoning PEO solution with backlight photography setup. The fluid reservoir is placed in between the LED light source and camera for better visualization of the thin siphon line. The distance between the LED and the object is 15 cm, and that between the object and the camera is 10 cm. Images are taken during siphoning operation and are used to investigate siphon line profile. The image of the tubeless siphoning used here is for 2% (w/w) PEO solution (in water), taken by smartphone camera (Samsung Galaxy J7 Prime).

2.3. Results and Discussion

2.3.1. Melt Electrospinning

Decreasing fiber diameter has been a long-lasting and challenging goal of the researchers in the melt electrospinning process due to the high viscosity nature of the polymer melt. Attempts have been taken to reduce the melt viscosity including temperature change and incorporation of additives or plasticizers that have been effective in reducing the fiber diameter [18]. Using

conductive additives have also been reported to be effective in reducing the fiber diameter due to an increase in the melt conductivity [19, 20]. However, no systematic method was utilized to capture the jet behavior to fundamentally study the mechanisms of the modification in each of the cases. An *in-situ* observation of the jet formation in the electrospinning process enabled us to precisely measure the formed cones diameter and correlate that to the modification mechanisms that are being employed ultimately to further optimize the process. More importantly, in-situ observation in electrospinning entails inherent limitations due to the high voltage utilization that inhibits close shots. Utilizing a backlight sharpens the edges of the objects, facilitating the size or shape analysis from the taken images even in lower resolutions taken from long distances (Figure 2.4-a).

2.3.1.1. Cone Diameter Analysis

Fabrication of sub-micron fibers have long been desired for many applications including filtration, tissue engineering, drug delivery, etc. There are many factors in an electrospinning process that controls the final fiber diameter. In a free surface electrospinning, precise control of the cone diameter at the initiation is crucially important. Factors including voltage, distance, or temperature can have a huge effect on the cone diameter. Having a systematic design to take in-situ picture of the cones enable us to control the final fiber diameter. Utilizing the backlit setup in Figure 2.2, an in-situ picture was taken from a single cone during the process (Figure 2.4-a). Using ImageJ software, the diameter of the cone at the initiation point as well as the diameter of the jet immediately after formation is measured. This is a useful information especially in a free surface electrospinning where no nozzle or spinneret is utilized to control the formation of the cones. For comparison, a picture was taken utilizing a side-lighting setup. In side-lighting the light source was placed on one side of the setup, shinning the jets from the side angle. As observed in Figure

2.4-b, this method of lighting does not offer enough clarity and the edges of the object tend to be fuzzy and over illuminated.

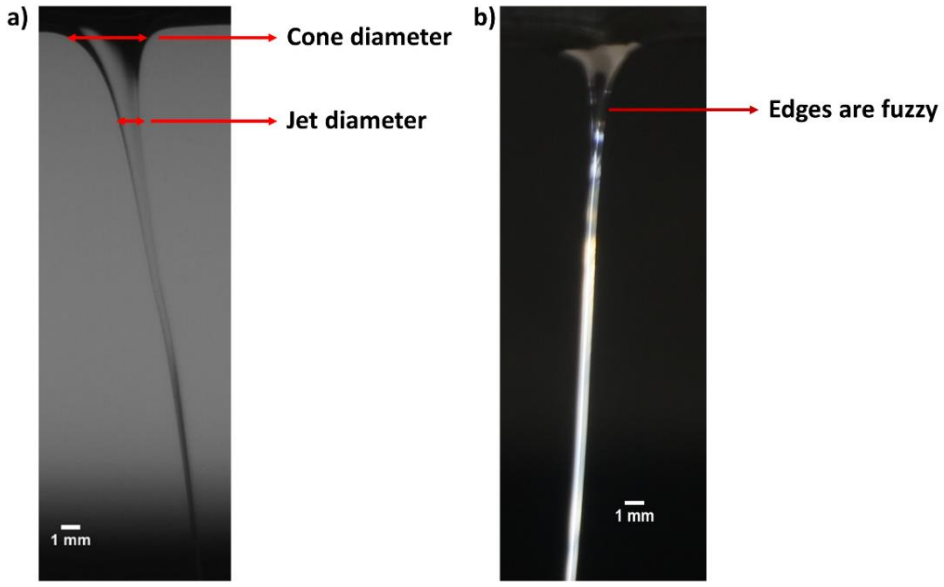

Figure 2.4. Picture of a single jet taken in-situ in the melt electrospinning process of PE utilizing a) backlit setup b) side-lighting setup. The backlit image of the jet provides clear edges for precise measurements while the side lighting image shows fuzzy edges with over illumination. The experiment conditions were: distance from the plate to collector 10 cm, voltage 40 kV, in an open environment temperature. The cone diameter obtained was 2.9±0.9 mm (at the initiation of the process) and 1±0.1 mm (after 20 minutes run of the process).

2.3.1.2. Jet Solidification

In many fiber processing techniques, fibers are fabricated through a jet formation followed by a phase change, usually solidification, process. In fiber melt processing, the solidification of the jet happens through heat transfer with the surrounding environment. After the solidification, no more stretching can be applied to the jet that could affect its properties including diameter. Monitoring the solidification point throughout the jet *in situ* is very important. So far, there is no effective visual technique to be utilized to observe the phase change in a fiber spinning process. In a solidification process, a transparent liquid phase transforms into an opaque solid phase. This transparency transformation creates a significant light contrast which can be captured by utilizing

a backlit setup (Figure 2.5). As observed in Figure 2.4-b, side-lighting does not provide this visual of the jet. The solidification point here is reported to occur within 0.7 cm of the length of the jet. Such a short solidification distance was previously identified by Zhmayev et al. and referred to electrohydrodynamic jet quenching in melt electrospinning process [21]. Knowing the solidification information would enable researchers to have a precise control over the solidification point by controlling the parameters affecting the phase change, (e.g. spin-line temperature, and the subsequent heat transfer process in the case of melt electrospinning) that significantly affects the final fiber morphology and properties.

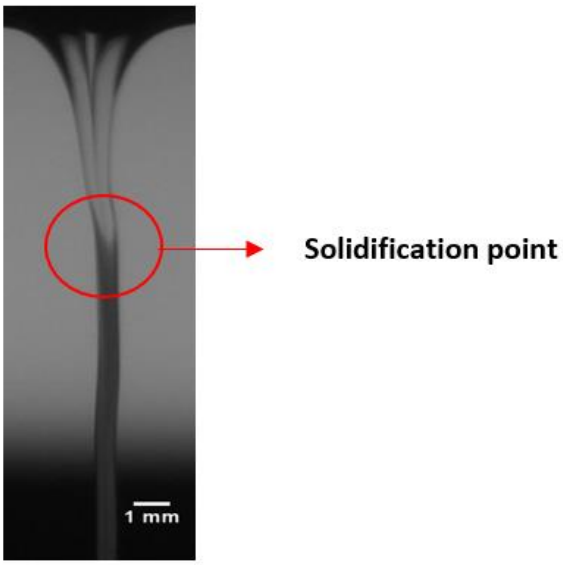

Figure 2.5. Visualization of the in-situ solidification of the jet in the melt electrospinning process utilizing backlight setup. The side-lit image does not capture the solidification point.

2.3.2. Tubeless siphoning

Extensional viscosities for non-Newtonian fluid can be estimated by the tubeless siphon technique where the liquid is continuously drawn into a capillary with raising the tube above the

liquid surface forming a column, as shown in Figure 2.6 [22, 23]. Having a stress-free boundary, tubeless siphoning is often considered to be wholly extensional, which is one of the major prerequisites for extensional viscosity measurement technique. The maximum height of siphon (h) is used to characterize the ratio (η_E/η) of non-Newtonian fluids, where η is shear viscosity, and η_E is extensional viscosity. An approximate hydrodynamic analysis shows $\eta_E/\eta \sim (h)^2$ [17]. However, clear visualization of siphon line is challenging to measure, especially in case of low viscosity polymer solutions. Figure 2.6 illustrates how siphon height can be measured from high resolution images taken from a video. The maximum siphon height can be calculated from the images by using ImageJ software. This measurement can successfully replace the manual measurement of the height by using measuring scale.

Moreover, as seen in the Figure 2.6, the column diameter decreases with distance from the fluid surface to the pipette entrance. This gradual decrease in diameter is needed to balance gravitational stress by increasing mean velocity component along the column [2]. A correlation between siphon height and diameter can be established to investigate extensional behavior of different polymer solutions. Images taken at different magnifications under backlight setting will be a potential tool to analyze the profile of extremely thin siphon lines which are not visible at certain height with the naked eye.

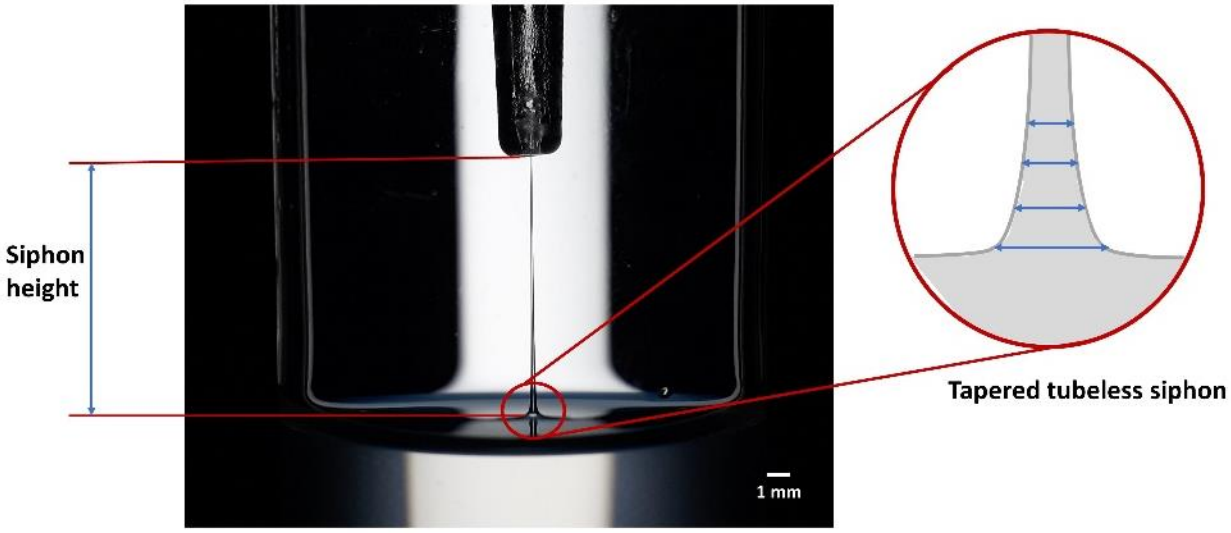

Figure 2.6. Illustration of siphon height and diameter measurement from images with improved contrast. The inset shows the gradual change in siphon diameter with axial distance from liquid surface for an extremely thin siphon line. **S**iphon diameter at different heights can be measured to investigate extensional behavior of different polymer solutions. The image of the tubeless siphoning used in the figure is for 2% (w/w) PEO solution (in water).

2.4. Conclusion

We have demonstrated a facile technique to acquire visual information using a simple LED backlight setup. The use of this imaging technique may allow to precisely analyze the processing profiles of melt electrospinning and tubeless siphoning of polymer fluids. A detailed quantitative analysis of these effects will be presented in future publications. The report presented herein could potentially be extended to in-line real-time determination of the sub-micron scale dimensions in fiber spinning, microfluidic flow, solution electrospinning, contact angle measurement for surface properties analysis, etc., where the output could be used to adjust the feeders.

2.5. Acknowledgement

This work was partially funded by the National Science Foundation (CMMI #1635113).

2.6. References

[1] Y. Murai, K. Inaba, Y. Takeda, F. Yamamoto, Backlight imaging tomography for slug flows in straight and helical tubes, Flow Measurement and Instrumentation 18(5-6) (2007) 223-229.

[2] Y. Xia, P. Callaghan, Imaging the velocity profiles in tubeless siphon flow by NMR microscopy, Journal of Magnetic Resonance 164(2) (2003) 365-368.

[3] E.F. Matthys, Measurement of velocity for polymeric fluids by a photochromic flow visualization technique: the tubeless siphon, Journal of Rheology 32(8) (1988) 773-788.

[4] K.S. Bronk, K.L. Michael, P. Pantano, D.R. Walt, Combined imaging and chemical sensing using a single optical imaging fiber, Analytical chemistry 67(17) (1995) 2750-2757.

[5] D. Glick, P. Thiansathaporn, R. Superfine, In situ imaging of polymer melt spreading with a high-temperature atomic force microscope, Applied physics letters 71(24) (1997) 3513-3515.

[6] J.C. De Anda, X. Wang, X. Lai, K. Roberts, K. Jennings, M. Wilkinson, D. Watson, D. Roberts, Real-time product morphology monitoring in crystallization using imaging technique, AIChE Journal 51(5) (2005) 1406-1414.

[7] B.L. Quist, Method and apparatus for backlighting and imaging multiple views of isolated features of an object, Google Patents, 2006.

[8] Y. Shin, M. Hohman, M. Brenner, G. Rutledge, Experimental characterization of electrospinning: the electrically forced jet and instabilities, Polymer 42(25) (2001) 09955-09967.

[9] N.M. Thoppey, J. Bochinski, L. Clarke, R.E. Gorga, Edge electrospinning for high throughput production of quality nanofibers, Nanotechnology 22(34) (2011) 345301.

[10] Y. Murai, H. Oiwa, T. Sasaki, K. Kondou, S. Yoshikawa, F. Yamamoto, Backlight imaging tomography for gas–liquid two-phase flow in a helically coiled tube, Measurement Science and Technology 16(7) (2005) 1459.

[11] G. Chen, H.H. Chai, L. Yu, C. Fang, Smartphone supported backlight illumination and image acquisition for microfluidic-based point-of-care testing, Biomedical Optics Express 9(10) (2018) 4604-4612.

[12] U. Kanade, B. Ganapathy, Camera placed behind a display with a transparent backlight, Google Patents, 2011.

[13] S. Liu, D.H. Reneker, Droplet-jet shape parameters predict electrospun polymer nanofiber diameter, Polymer 168 (2019) 155-158.

[14] F.M. Wunner, P. Mieszczanek, O. Bas, S. Eggert, J. Maartens, P.D. Dalton, E.M. De-Juan-Pardo, D.W. Hutmacher, Printomics: the high-throughput analysis of printing parameters applied to melt electrowriting, Biofabrication 11(2) (2019) 025004.

[15] Q. Wang, C.K. Curtis, N.M. Thoppey, J.R. Bochinski, R.E. Gorga, L.I. Clarke, Unconfined, melt edge electrospinning from multiple, spontaneous, self-organized polymer jets, Materials Research Express 1(4) (2014) 045304.

[16] R.B. Bird, R.C. Armstrong, O. Hassager, Dynamics of polymeric liquids. Vol. 1: Fluid mechanics, (1987).

[17] K.K. Chao, M.C. Williams, The ductless siphon: a useful test for evaluating dilute polymer solution elongational behavior. Consistency with molecular theory and parameters, Journal of Rheology 27(5) (1983) 451-474.

[18] T.M. Robinson, D.W. Hutmacher, P.D. Dalton, The next frontier in melt electrospinning: taming the jet, Advanced Functional Materials 29(44) (2019) 1904664.

[19] S. Malakhov, S. Belousov, A. Bakirov, S. Chvalun, Electrospinning of Non-Woven Materials from the Melt of Polyamide-6 with Added Magnesium, Calcium, and Zinc Stearates, Fibre Chemistry 47(1) (2015) 14-19.

[20] E. Shabani, C. Li, R. Komer, L. Clarke, J. Bochinski, R. Gorga, B. Boland, N. Sheoran, Strategies to improve the unconfined melt electrospinning process via incorporation of ionically conductive particles, Bulletin of the American Physical Society 64 (2019).

[21] E. Zhmayev, D. Cho, Y. Lak Joo, Electrohydrodynamic quenching in polymer melt electrospinning, Physics of fluids 23(7) (2011) 073102.

[22] S. Peng, R. Landel, Preliminary investigation of elongational flow of dilute polymer solutions, Journal of Applied Physics 47(10) (1976) 4255-4260.

[23] R. Balmor, Steady and unsteady isochoric simple extensional flows, Journal of Non-Newtonian Fluid Mechanics 2(4) (1977) 307-322.

CHAPTER 3: The effect of the spin-line temperature profile on the translocation of the solidification point and jet thinning in unconfined melt electrospinning

Elnaz Shabani[1], Amir Azimi Yancheshme[2], Avner Ronen[3,4], Russell E. Gorga[1*]

[1]Fiber and Polymer Science Program, North Carolina State University, Raleigh, North Carolina 27695, United States
[2]Department of Chemical and Biological Engineering, Drexel University, Philadelphia, Pennsylvania, United States
[3]Civil and Environmental Engineering Department, Temple University, Philadelphia, Pennsylvania, United States
[4]Zuckerberg Institute for Water Research, The Jacob Blaustein Institutes for Desert Research, Ben-Gurion University of the Negev, Sede Boker, Israel
[*]Corresponding author: Russell E. Gorga, Email Address: regorga@ncsu.edu

This chapter has been published as a manuscript in the journal ACS Applied Polymer Materials (ACS Publications) in 2020.

Abstract

This work aims to provide effective strategies and practical tools to control fiber diameter, a long-lasting challenge in the application of free surface melt electrospinning, mainly by highlighting the importance of solidification point. A systematic approach to map the solidification point and temperature profile in an electrohydrodynamic jet in the melt electrospinning process was developed experimentally through backlit imaging technique and numerically through computational fluid dynamic. The effect of the different spin-line temperature profiles on the robustness of the process as well as the fiber morphology was investigated. SEM analysis demonstrated that at high spin-line temperature profiles, the fiber diameter dropped four times compared to the room temperature spin-line environment. Both in-situ backlit images from the jets in the spin-line and the numerical phase fraction analysis revealed an immediate solidification of the jet, which is elongated by twice in the case of the high spin-line temperature profiles. The elongated freezing length for the high spin-line temperature profiles as a result of the delayed solidification was identified as one of the main factors contributing to the jet thinning and subsequent fiber diameter reduction. Based on the simulation, the temperature profile of the jet demonstrated an approximately 20 °C drops along the jet length in the non-solidified portion (freezing length), proposing the viscosity drop as a second factor in the fiber diameter reduction mechanism. Ultimately, molten film thickness on the plate was identified as a semi-physical confinement parameter, controlling the size of the formed cones and subsequently fiber diameter, despite the free surface nature of the unconfined melt electrospinning.

Keywords: Unconfined melt electrospinning, solidification point, spin-line temperature profile, electrohydrodynamic jet, Computational fluid dynamic

3.1. Introduction

Electrospinning is a versatile technique to produce continuous fibers. A wide variety of polymers are viable to turn into the fibrous structure of micron to nano size through electrospinning.[1] These sub-micron scale structures possess an extensive surface area to volume ratio that provides them with a variety of applications.[2] Applications for the nanofibers include biomedical[3,4,5], textiles[6], filtrations[7], sensors[8,9], etc. Electrospinning even though is a simple to assemble and straightforward to fabricate materials with advanced functions, has not yet become a potential source of fabrication for large-scale manufacturing. The low production rate has been a long-lasting bottleneck for this technique that has recently become an emerging topic of investigation for researchers.

Free surface electrospinning was introduced in 2004 by Yarin et al., exploring the potential of the electrospinning technique for upscale and high production rate purposes.[10] In their first trial, both electrical and magnetic fields were utilized as driving forces acting on a two-layer system. They observed that several cones form on the free surface of the fluid that increases the production rate to 12-fold enhancement and eliminates the frequent clogging problem in traditional electrospinning setups. Lukas et al. explain the theoretical concept explaining the self-organization of the jets from the free surface of a one-dimensional liquid.[11] The phenomenon is explained by the initial wave formation on the free surface of the liquid, followed by the mechanism of fastest forming instability domination at a certain electric field that creates the so-called perturbation or cones. The insightful knowledge on the fundamentals of the free surface electrospinning has facilitated many interventions on the setup design for the technique.[12,13,14,15,16,17,18,19] Many of the current free surface designs utilize a polymer solution to fabricate fibers.

Solution electrospinning, despite the popularity encompasses various challenges, including usage of toxic solvents, low production rate, presence of residual solvents in fiber, and the limitation to be employed for thermoplastics, like polyolefins, that do not readily dissolve in a solvent at room temperature.[20] Melt electrospinning, which utilizes the polymer melt directly as a spinning fluid, has gained popularity in recent years. This green approach provides versatility for thermoplastic fiber fabrication, offers sustainability by eliminating the toxic solvent, and enhances the overall throughput.[21,22] Recently introduced free surface melt electrospinning overcomes the challenges associated with the pumping of the high viscosity polymer melt through a tiny needle and increases the viability of the technique for industrial upscaling. The first configuration was proposed in 2010, called rod-electrospinning, in which polymer is fed on top of a rod electrode, and after melting, self-organization of multiple jets on the free surface of the rod produces spinning jets.[18] Several more designs of free surface electrospinning have been proposed till now, that even though meets the essential shortcomings of the melt electrospinning technique, yet suffers from difficulty in the feeding mechanism or complexity in the design.[15,23] Melt electrospinning from a plate surface, developed in 2014 by Gorga and Clarke et.al. introduced a simple approach for fabricating micron-scale fibers.[24] Due to the high viscosity nature of the polymer melt and the lack of whipping motion, fibers from this technique are shown to have larger diameters compared to the solution techniques. Therefore, further thinning optimization is required to obtain fibers with comparable size ranges to their solution spun counterparts. Many researchers have identified the main factor affecting jet thinning is the viscosity that is normally controlled by temperature. However, Naraghi et al. observed a reverse dependence of fiber diameter to melt viscosity for a free surface melt electrospinning, attributed to the viscosity-dependent flow rate in this method. The effect of the spin-line temperature, the temperature of the surrounding air around the spinning

jet, on the morphology of the fibers has been studied before. This was obtained by the utilization of extra heating modules in the spin-line region, which could complexify the setup design further. The further thinning of the fiber by increasing the spin-line temperature is attributed to the decreased viscosity of the jet and, as a result, the enhancement of the stretchability.[25,26] Joo et al. utilized an infrared camera to monitor the inside jet temperature tentatively and observed a rapid jet quenching, faster than model predictions, which were linked to electrohydrodynamic effects.[27]

Achieving sub-micron scale fibers from melt phase spinning processes, including melt electrospinning, has been a long-lasting challenge. To this date, there is no study that fundamentally investigates the essence of the solidification or phase change process in an electrospinning jet and its correlation with further thinning of the jet and the final fiber diameter. In this work, a backlighting technique, developed by the authors[28], was utilized to precisely determine the solidification point in a melt electrospun jet. The electrospinning jet was considered as a phase change material that undergoes solidification to become a fiber. This concept became the basis for the utilization of the computational fluid dynamic, introduced as a practical tool to monitor jet behavior in a melt phase electrospinning process. The approach here is unique because it introduces a systematic method to precisely control the spinning zone temperature without the need to increase the melt temperature or incorporate any second-part heating module along with a real-time monitoring tool. The strategies and tools are in particular discussed for the relatively new field of free surface melt electrospinning; however, it should translate to other melt phase fiber fabrication techniques.

3.2. Experimental

3.2.1. Materials

In this work, linear low-density polyethylene (PE) granule was used for all experiments. PE, ASPUN 6850 Fiber Grade Resin, with the melt index of 30 g/min under 190 °C/2.16 kg based on the datasheet provided by the manufacturer, was supplied by Dow Chemical company. PE powder was obtained with cryogenic grinder using freezer mill grinder, SPEX CertiPrep 6750 purchased from SPEX SamplePrep. PE powder was used to create a uniform molten film on the plate. The melting temperature of this PE, (T_m), based on the obtained DSC thermogram, is 129 °C.

3.2.2. Apparatus

The unconfined melt electrospinning apparatus (Figure 1) consists of an aluminum sharp edge plate with a surface area of 13.6 x 4.8 cm and edge walls of 1 mm thickness and 0.8 cm height on the sides (With no wall on the sharp edge where fibers are formed). As aluminum has low abrasion resistance, to get a consistent sharpness in the spinning edge of the plate that undergoes heavy cleaning after each run of the process, a steel blade was cut and screwed in on to the edge. A commercial hot plate (Fisher Scientific, model: HP88857100) was used to heat the source plate in two modes: In the first mode, the source plate is placed on the hot plate off centered where the edge of the plate protrudes for 2 cm. In the second mode, the source plate is attached to the hot plate from the back wall, and the entire plate is protruded (Figure 2). The two modes provide the spin-line environment with different temperature profiles discussed in more detail in section 1.4. In both modes, the entire apparatus is placed in a wooden chamber with a transparent front door and a top wall made from acrylic to observe the process. Thermal grease (Halnziye HY880) was used between the source plate and hot plate for better thermal contact. One side of the source plate

is connected to a k-type thermocouple to monitor the temperature of the source plate. The opposite side of the plate is attached to the ground wire. The counter electrode consists of a square aluminum plate with a surface area of 30 x 30 cm that is connected to the negative polarity of a high voltage source (Glassman, Model FC60R2). A hand-made thermocouple holder is placed inside the chamber to measure the inside melt temperature before and after each run.

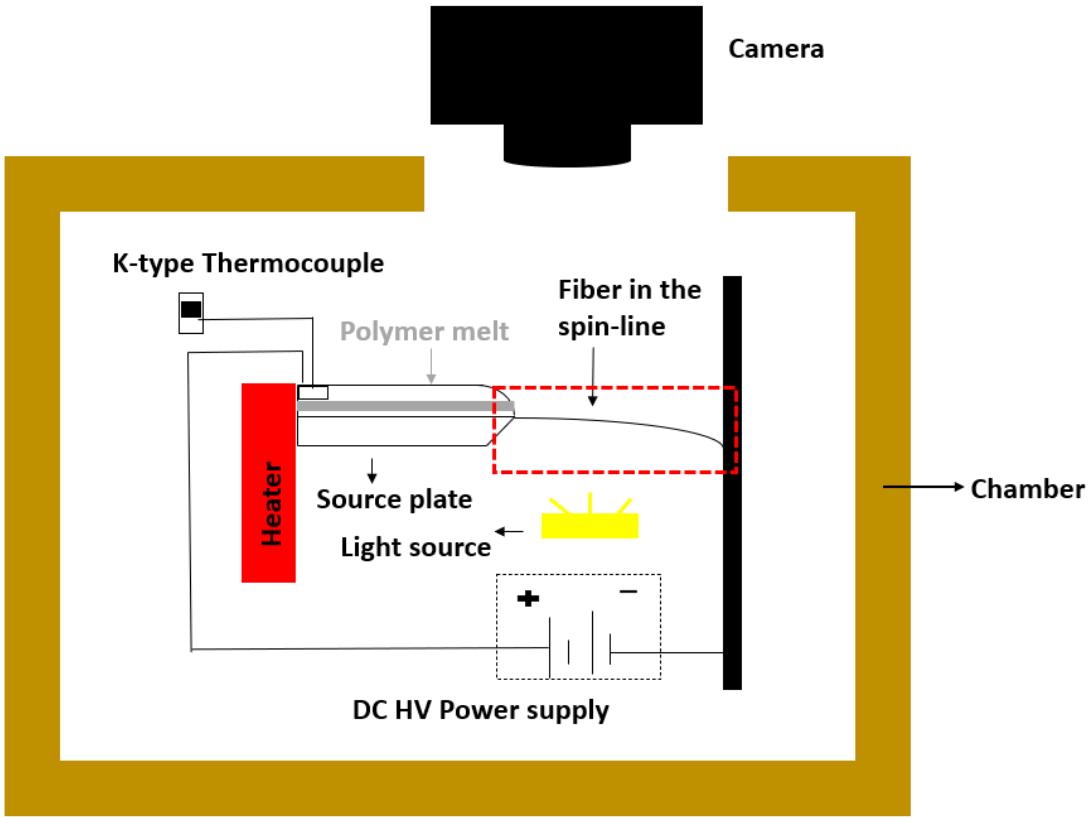

Figure 3.1. Schematic diagram of the apparatus inside the chamber from side view accompanied with a backlighting camera setup.

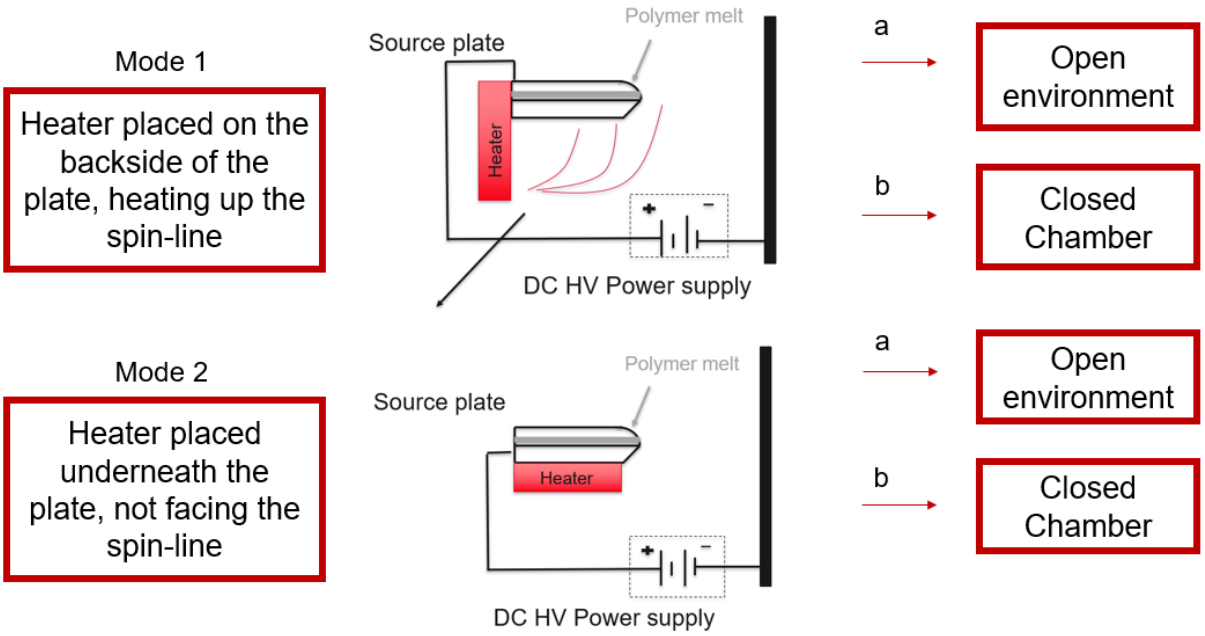

Figure 3.2. Schematic diagram of the different modes of configuration; mode 1-a (open environment, vertical heater), mode 1-b (closed chamber, vertical heater), mode 2-a (open environment, horizontal heater), and mode 2-b (closed chamber, horizontal heater). Each mode provides a different spin-line temperature profile (section 3.2.4).

3.2.3. The experiment characterization

All the spinning experiments were done at the electric field of 1.84E6 V/m at 500 microns away from the plate edge. Simulations were done by Ansys Maxwell software version 19.2. Voltages were set to 40 kV for the Mode 1 and 32.7 kV for the mode 2 configuration to obtain the same electric field magnitude, as simulation showed that the plate protrusion affects the electric field around the edge, which can result in the different electric field for the two modes. More information regarding the electric field simulation is provided in the supporting information (Figure S1 and Table S1). The spinning distance was set to 10 cm. The source plate was set to 190 °C by which the temperature of the inside molten film on the plate reached 165 ± 2 °C and was almost constant throughout the running process for all the experiments with +2 °C increase after 20 minutes, which is assumed to be negligible. A camcorder (Canon, Model HF R72) was used to

record the spinning process (run for 20, 40, and 70 minutes) for further analysis of jet evolution after the process. Still images were taken by a Canon DSLR camera (Canon EOS Rebel T5i with 18-135mm EF-S IS STM Lens) for cone diameter and inter-jet spacing analysis using ImageJ software. Each experiment was repeated three times, and averaged results were reported. The backlighting technique was developed to obtain high-resolution images with clear object edges[28]. In this technique, a wireless portable LED lamp (33 LED Super Bright Wardrobe Lights, Portable Magnetic Stick Wireless, geometry 9.5 inches by 1.5 inches by 0.7 inches, manufacturer: CHNXU) was placed in the spinning region, shinning the camera lens directly with the spinning jets located between the camera and the lighting source (Figure 1). The process was begun by heating the source plate to 190 °C, and after the temperature of the plate was steady, 10 grams (except for where noted) of the polymer powder was uniformly spread on the plate. When the source plate temperature gets steady to 190 °C (experimentally, this was obtained after 15-20 minutes), the temperature of the molten polymer film was measured by inserting a thermocouple inside the melt. Lastly, the high voltage is applied between the source plate and the collector, and electrospinning starts after the induction time is passed. The induction time is the time for the waves to pass the critical growth factor to prevail the formed waves on the surface of the fluid beyond the critical electric field and turn into the perturbations.

3.2.4. Spin-line temperature profile

Four spin-line temperature profiles were obtained through different configuration designs (Figure 3.2) and were measured by inserting a thermocouple at 0.5 cm, 1 cm, 2 cm, 3 cm, and 10 cm distance from the plate edge, in the spin-line (Figure 3.3). Cone zone, defined as the region 0.5 cm from the plate edge in the spin-line is where cones are initiated after ejecting from the plate. As the cone zone temperature is an important feature of each spin-line temperature profiles (due

to the non-solidified nature of the jet in this region that is discussed later in more details), in this work, spin-line temperature profiles were mentioned by their cone-zone temperature (e.g., the cone zone temperature of RT (room temperature, 35 °C), refers to the dark blue curve in Figure 3.3).

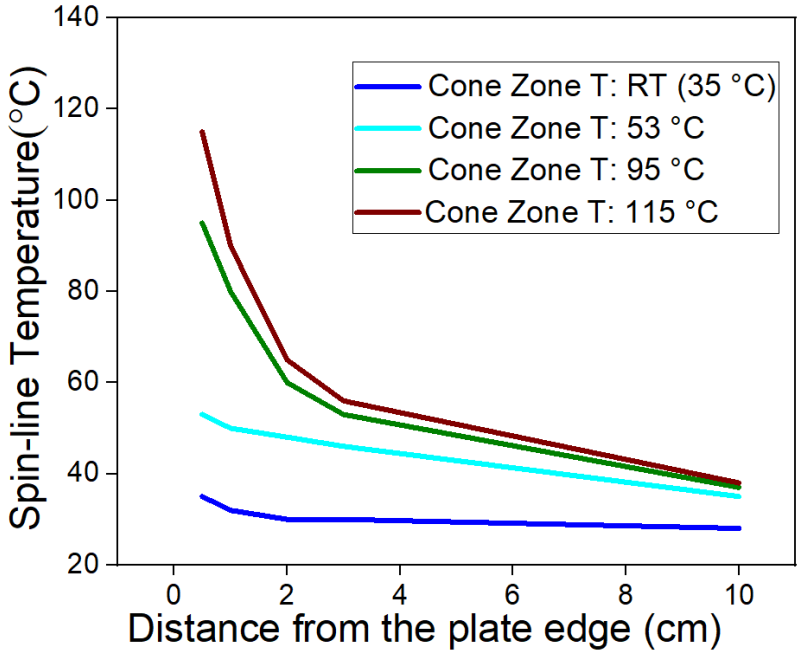

Figure 3.3. Spin-line temperature profiles specified by their cone zone temperature. Profiles are related to their respective configuration as Cone Zone T: 115 °C relates to the mode 1-b, Cone Zone T: 95 °C relates to the mode 1-a, Cone Zone T: 53 °C relates to the mode 2-b, and Cone Zone T: RT relates to the mode 2-a (mode configurations are demonstrated in Figure 3.2).

It was observed that the temperature is almost uniform throughout the 13.6 cm length of the plate (from left to the right side) and only changes through the spin-line, the path that fiber travels after ejecting from the plate to reach the collector, as is specified by the spin-line temperature profiles. The hot plate is the main source of the thermal heating for both the source plate and the spin-line. The further away from the hot plate into the spin-line, the temperature drops to lower degrees, as observed in the profiles. Another factor changing the temperature profile is the configuration of the hot plate. In the vertical mode (1-a and 1-b), the spin-line region was directly exposed by the hot plate and was being heated through the convection mechanism. In the

case of horizontal configuration (2-a and 2-b), the spin-line region was less exposed by the hot plate and therefore was not directly being heat up; hence a different profile was obtained.

3.2.5. Fiber Characterization

The fiber mat morphology was characterized using scanning electron microscopy (SEM) (Hitachi S3200N Variable Pressure SEM) at an accelerating voltage of 5 kV. The fibers were coated using a sputter coater with Au-Pd with a thickness of approximately 50 nm to form a conductive surface. To analyze the fiber diameter from the SEM images, ImageJ software analyzer was used. For each sample approximately 50 fibers were analyzed using at least 3 SEM images from different samples, and the average fiber diameter and standard error were reported.

3.2.6. Numerical modeling and simulation

A comprehensive numerical approach was applied in order to describe the phase change process of the polymer melt in the electrospinning process. Heat and momentum transport equations along with continuity equations (equations 1-3) were numerically solved using Finite Element Method (FEM) to describe the fluid flow and temperature gradients throughout the fiber jet. Zero shear rate viscosity of the polyethylene at the experiment temperature was experimentally measured and substituted in the momentum equation. This is also in line with other researchers' approach in the modeling of the melt electrospinning jet.[26,27] As the system is a continuous process, a steady state model was utilized. All simulations were performed in a 2D-axisymmetric framework with the aid of commercial code COMSOL MULTIPHYSICS 5.5.

Momentum transport equation :

$$\rho(\mathrm{u}\cdot\nabla)\mathrm{u} = -\nabla \mathrm{p} + \mu\nabla^2\mathrm{u} \qquad (1)$$

Continuity equation:

$$\nabla\cdot\mathrm{u} = 0 \qquad (2)$$

Heat transport equation:

$$\rho c_P u \nabla T = K \nabla^2 T \qquad (3)$$

In which p is the pressure, ρ is the density (kg/m^3), k is the thermal conductivity (W/m. K), which is assumed to be constant in the melt electrospinning process[26,27], C_p is the specific heat capacity at constant pressure (J/kg.K), and u is the velocity of polymer jet. Table A-1.2 contains material properties and operational conditions used in simulations, which are the same as our experimental conditions. Simulations have been done for the four different cases of spin-line temperature profile categorized based on the surrounding air temperatures, as shown in Figure 3.3.

In order to take the phase change process into account, instead of using latent heat directly into the energy balance equation, apparent heat capacity formulation was used [28,29]. In this formulation, to account for the latent heat related to the phase transition, the phase of material in the "mushy" zone (i.e., region of both solid and molten material coexists in the temperature interval of $T_m - {\Delta T}/{2}$ and $T_m + {\Delta T}/{2}$) is modeled by a smoothed function, θ, representing the fraction of the phase before the transition. The density (ρ), thermal conductivity (k), and the specific heat capacity (C_p)of the material are predicted as below (Equations 4 -6):

$$\rho = \theta\rho_1 + (1-\theta)\rho_2 \qquad (4)$$

$$k = \theta k_1 + (1-\theta)k_2 \qquad (5)$$

$$\rho C_p = \left(\theta\rho_1 C_{p1} + (1-\theta)\rho_2 C_{p2}\right) + \rho L_m \, {d\alpha_m}/{dT} \qquad (6)$$

Indices 1 and 2 denote the phase 1 (liquid) and phase 2 (solid), respectively. The first term of equation 6 represents the equivalent specific heat capacity where θ represents the melt fraction, and the second term is the distribution of the latent heat. $L_m$is the latent heat and α_m is the mass fraction, which is defined by equation 7:

$$\alpha_m = {(1-\theta)\rho_2 - \theta\rho_1}/{2\rho} \qquad (7)$$

Heat transfer of the fiber jet with surrounding air was modeled through convection heat transfer using heat transfer coefficient (h) and surrounding air temperature of the spin-line ($T_{sur.}$) as specified in Figure 3.3 profiles. An empirical relation by Matsuo and Kase [30] was used to predict the heat transfer coefficient (equation 8). Adopted boundary conditions in this model have been shown in Table A-1.3 and Figure A-1.2-a**.**

$$h = 0.388 k_{air} \left({V}/{\vartheta_{air}.A}\right)^{0.334} (1 + ({8v_{air}}/{V})^2)^{0.166} \qquad (8)$$

In which h is the heat transfer coefficient, $k_{air}$is the air thermal conductivity, V is the fiber velocity, v_{air} is the surrounding air velocity, A is the cross-sectional area of the fiber, and ϑ_{air} is the kinematic viscosity of the air.

In order to resolve the location of phase transformation precisely, as it is not known in the first place, we started our simulations with a fine mesh (free triangular, 73556 elements) along with the adaptive mesh refinement algorithm (i.e., refining the mesh to put more elements around the transition region) to rebuild meshes up to 3 adaptations. Figure A-1.2 (b-c) shows incorporated meshes before and after adaptation.

3.3. Results and Discussion

3.3.1. Jet Evolution

The spinning process starts with the self-initiation of the cone shape protrusions on the free surface of the polymer melt (Figure 3.4-a). This phenomenon is recognized as self-organization based on the fastest forming instabilities. The interaction between the electric field force and the surface tension of the fluid causes instantaneous perturbation formation, which starts the

electrospinning process (Figure 3.4-b). The protrusions turn into spinning jets moving towards the collector and finally lay down on the collector as fibers (Figure 3.4-c).

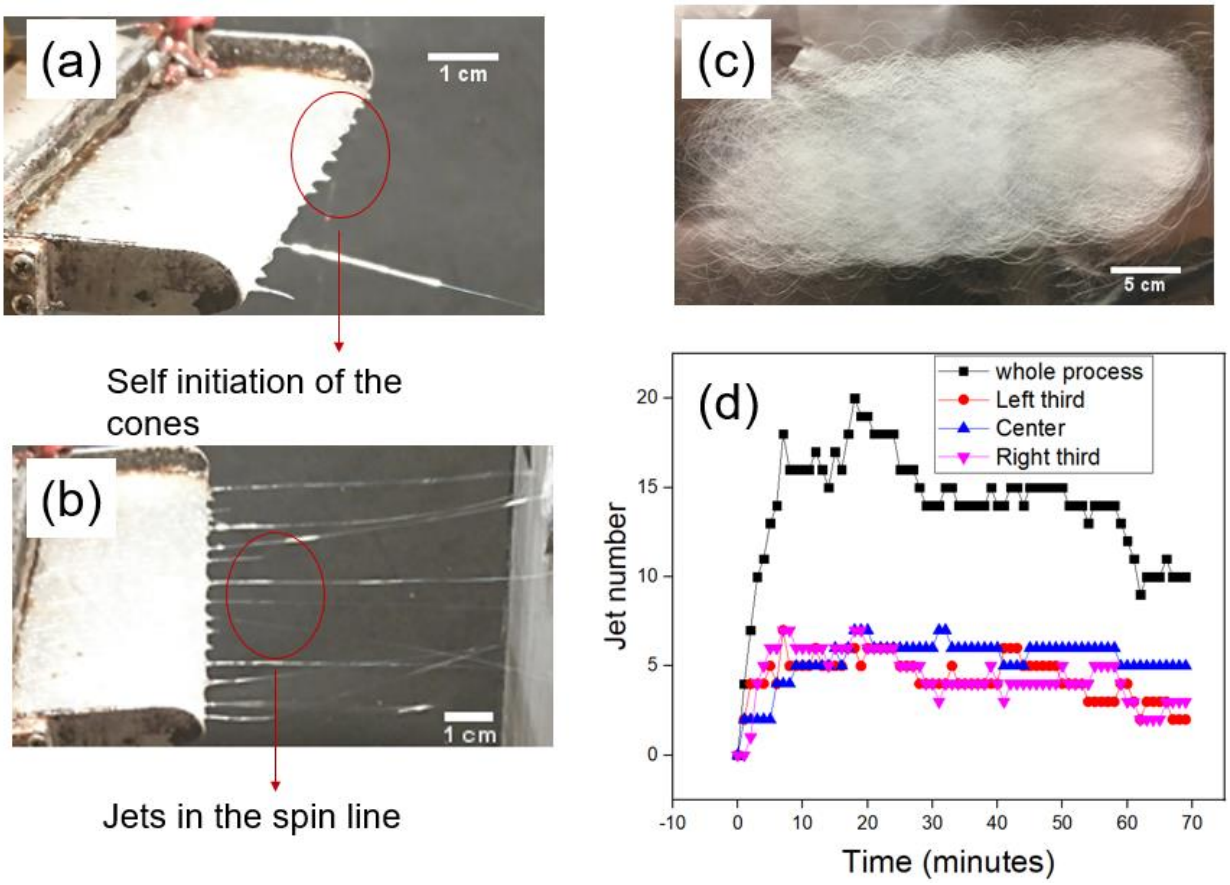

Figure 3.4. Illustration of the electrospinning process for (a) self-initiation of the cones (b) in process view of the spinning jets (c) final product. The electrospinning parameters are set to 10 cm distance between the plate and the collector, 32.7 kV voltage, and the mode 1-a setup configuration with the cone zone temperature of 95 °C (d) jet evolution of the electrospinning at 40 kV and cone zone temperature of 53 °C for 70 minutes run of the process. The analysis is done for the entire plate (black curve) as well as the middle, right, and left sections of the plate (colored curves).

The jet number evolution with time is shown in Figure 3.4-d for different run times. It is observed that the jet number evolution with time follows a growth function and levels off approximately after a 15-20 minutes. The total number of jets levels off when the inter-jet distance saturates. As this saturation occurs after 15 to 20 minutes run of experiments, all the experimental analysis is carried out on the products of 20 minutes experiment run. The jet number analysis has

been carried out, dividing the source plate into three sections. It is observed that all three sections of the plate (right, center, and left) show the same trend of jet evolution. This observation proves that the effect of side edges on the electric field is negligible on the spinning process.

3.3.2. Fabrication of sub-micron fiber

An important parameter in melt electrospinning that affects the fiber diameter is melt viscosity, which is inversely proportional to the temperature. Increasing the polymer melt temperature well above the melting point can lower the viscosity of the melt; however prolonged exposure to high temperature can cause chain scission and degradation.[33] Therefore, higher temperature in the spin-line region, where jets enter after leaving the source plate, prevents spontaneous freezing of the jets, providing more stretching and lowers fiber diameter. In the following section, four different spin-line temperature profiles were examined, and their effect on the solidification point and, ultimately, fiber morphology and other process properties were described.

3.3.3. Evolution of the jet number and jet spacing with the spin-line temperature

The distance between two adjacent jets was calculated experimentally by analyzing the static photo of the process taken after 20 minutes. The experimental results demonstrate that at higher spin-line temperature, the average of jet-jet spacing decreases, and it follows a narrower distribution. At higher spin-line temperature, the average number of jets is also higher (Figure 3.5 (a-b)). The narrower distribution of the spacings at higher spin-line profiles suggests that at a more crowded plate jets are likely to place more organized compared to an empty surface where jets can localize more arbitrarily. The initially formed waves are the result of the interaction of the electric field and the surface tension on the surface of the fluid. Even though the melt temperature was kept constant despite the change in the spin-line temperature, one might assume that the melt

surface on the edge of the plate where cones are formed is exposed to lower temperatures in case of lower spin-line profiles, which can affect the surface tension. Hence, it is noteworthy to recognize the possibility of the change in the surface tension of the polymer melt at different spin-line profile settings. As an estimation, the surface tension was calculated for the formed cones (perturbation), as they are a good representative of the melt surface at the edge of the plate. To estimate the temperature of the perturbations, the temperature profile throughout the entire jet, both on the surface and inside of the jet, was numerically calculated using COMSOL simulation, which is discussed in more details in section 3.3.4.

The experimental average jet spacing was calculated by dividing the plate length by the average number of jets that were calculated by analyzing the recorded process over the 20 minutes run of the experiment (the recorded process is reported in Figure 3.4-d). The theoretical jet spacing was calculated based on the equation 9[11].

$$\lambda = 2\pi(3\gamma/2\varepsilon_0 E^2) \qquad (9)$$

where λ is the jet spacing, $\varepsilon_0$is the permittivity of the free space, γ is the surface tension and is calculated based on the equation from reference[33] (γ = 33.1- 0.0390*T (°C) mN/m). Temperatures are calculated from the simulation on the surface of the cones (discussed in more detail in section 3.3.4) and are reported in Table A-1.4. The electric field value 500 microns away from the plate edge, which is a good estimation of where cones are formed and starting to turn into jets, is calculated based on the electric field simulation and is 1.8E6 V/m. Based on the simulation, the change in the jet surface temperature was relatively minimal, which is shown not to affect the surface tension of the melt at different spin-line profiles. The experimental average jet-jet spacing is approximately within the range of theoretically calculated spacing, and at higher temperature,

with closer packing of the jets, the experimental results are closer to the theoretical data as is observed in Figure 3.5-c.

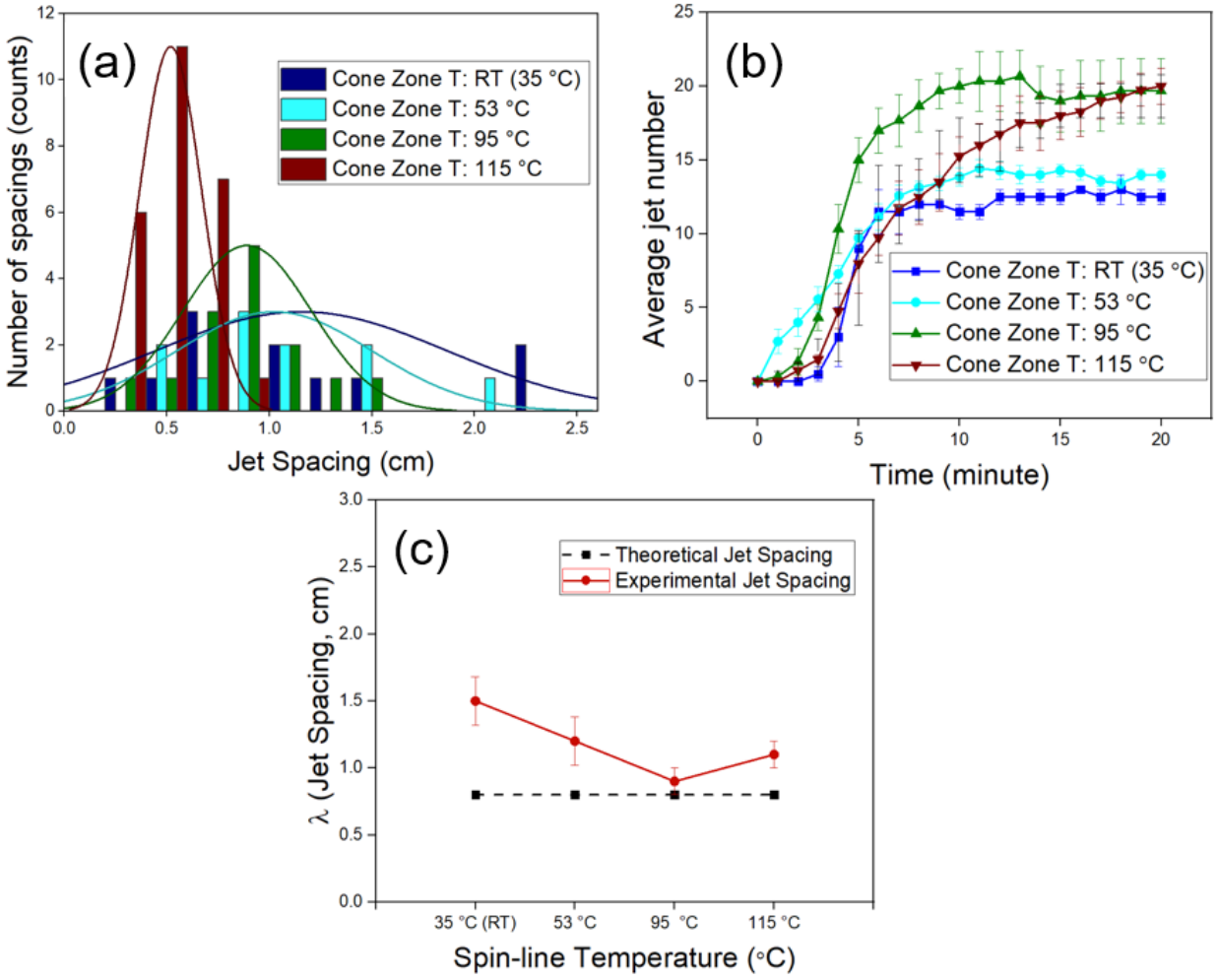

Figure 3.5. (a) Histogram of the jet spacing analysis of the 20 minutes run of experiment for different spin-line temperature profile, (b) Average jet number evolution for the first 20 minutes of the experiment (c) the theoretical and experimental average jet spacing over the 20 minutes run of the experimental for different spin-line temperature profiles.

Figure 3.6 (a-d) shows the effect of the spin-line temperature profile on fiber morphology and diameter. By increasing the spin-line temperature from room temperature to the 115 °C temperature profile, the average fiber diameter decreases from 43 microns to 11 microns. Based

on the SEM images, the uniformity of the morphology significantly enhances at higher spin-line temperatures.

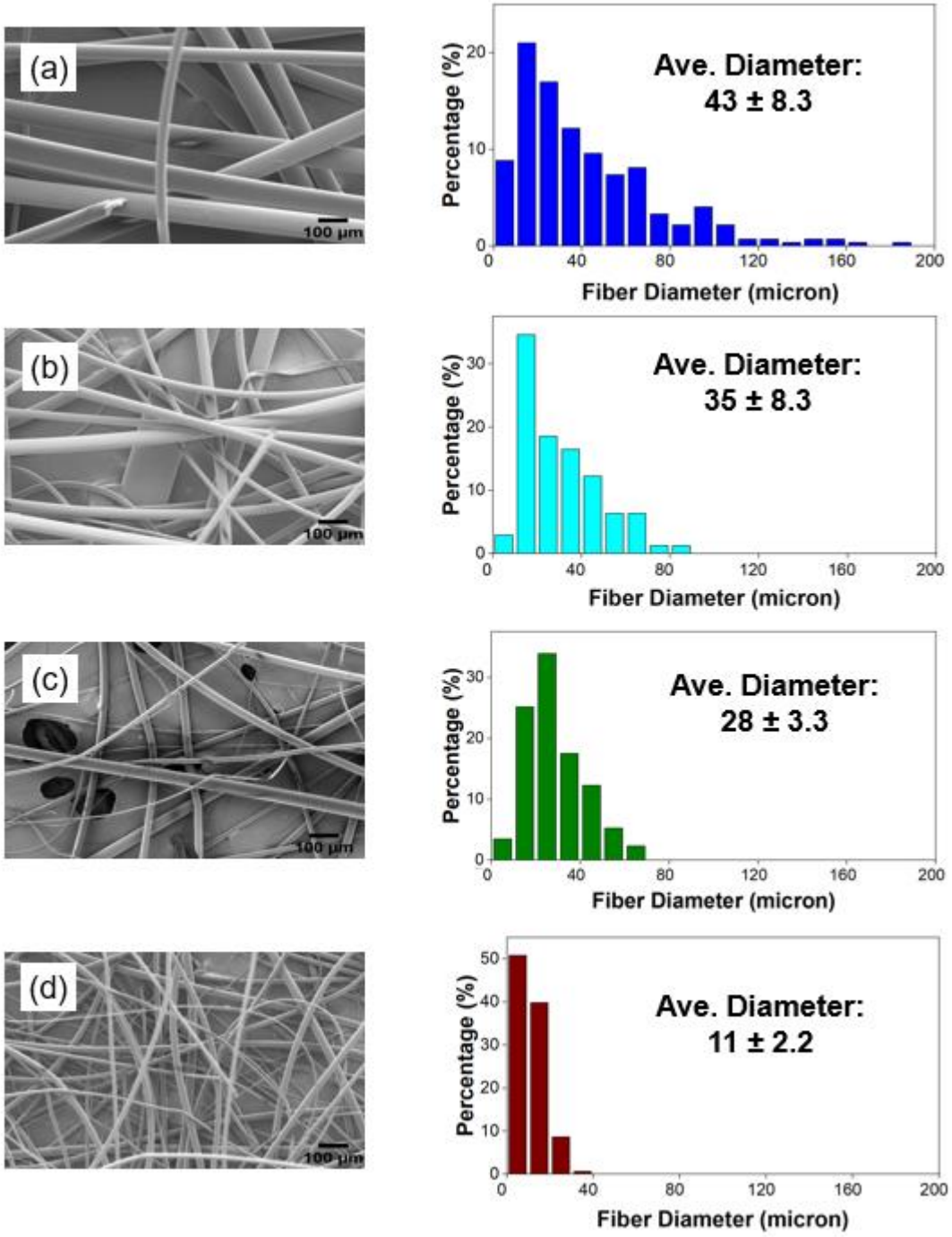

Figure 3.6. SEM images, fiber diameter distribution, and the reported measured fiber diameter for spin-line temperature profiles of (a) room temperature (35 °C) (b) 53 °C (c) 95 °C (d) 115 °C.

To analyze the fundamental effect of the spin-line temperature on lowering the fiber diameter, two hypotheses were proposed and evaluated. In the first hypothesis, the role of the spin-line temperature on reducing the size of the formed cones (perturbations) was evaluated. As observed in the jet-spacing analysis, at high temperature profiles, more cones and jets are formed. This observation suggests that as more cones are formed on the free surface of the melt, fewer spaces might be available for the newer cones to form; hence either smaller cones will be initiated, or cones will shrink throughout the process. To test this hypothesis, static photos taken from the process both at the initiation of each cone and after 20 minutes run of the experiment were examined, and cone diameters were measured and are reported in Figure A-1.3 (a-b). Based on the observations, the average cone diameter does not show a trend with the cone zone temperature. This was expected as the cones (protrusions) are formed due to the interaction between the electric field and the surface tension (equation 9) on the free surface of the fluid, and viscosity (as an interrelated fluid parameter with the temperature) is not a factor. Moreover, the inside melt temperature and as a result, the viscosity is kept constant in between all experiments, and only the spin-line temperature is variable. However, with increasing the temperature, a narrower distribution of cone diameter is obtained at the initiation stage. This is explained by higher crowds of cones (or jets) at higher spin-line temperature (Figure 3.5-b), which is assumed to help with the uniform nucleation (initiation stage) of the cones on the free surface of the melt.

The second hypothesis regarding the mechanism of the fiber diameter reduction at the higher spin-line temperature profiles is the solidification length throughout the jet. It is expected that at a higher spin-line temperature, not only is the jet experiencing a higher temperature and lower viscosity; it will go through a greater amount of stretching due to the delayed solidification in the spin-line. The stretching force on the jet is only effective on the thinning of the jet when

applies to the melt portion of the jet, as the solidified portion does not provide any significant chain mobility. To evaluate this, static photos were taken from the process utilizing the developed backlighting technique. This technique provided a means to take high-quality in-situ images from a micron-scale object and revealed information regarding the phase change of the jets during the electrospinning process, which was previously unattainable. The freezing point (the phase change location) is identified by the transformation point of the transparent liquid jet into an opaque solidified jet. Figure 3.7 (a-b) In this work, the distance between the plate edge and the solidification point is defined as freezing length. The freezing length was calculated for 15 distinct jets for each of the four different spin-line profiles. It was observed that at high spin line temperature (115 ℃), the freezing length (FL) is longer than that of the lower temperature profiles. It is worthwhile to mention that the cone diameter affects the size of the formed jet and consequently the jet's solidification process, as larger protrusions of the polymer melt take longer to solidify. To solicit the effect of the cone size, the freezing length of the jet is normalized by its cone diameter (D_c), and the result is reported as freezing length ratio (equation 10) in Figure 3.7-c.

$$\text{Freezing Length} = {}^{\text{FL}}/_{D_c} \qquad (10)$$

Based on the results, the freezing length ratio, and the freezing length for the 115 ℃ profile are almost two times higher than the room temperature profile. The delay in the solidification provides room for further stretching of the jet in the spin-line and can directly affect the fiber diameter. In the next section, the freezing length was further validated through computation fluid dynamic simulation. Moreover, the temperature profile of the spinning jet was calculated to monitor the temperature and, as a result, viscosity change throughout the length of the jet.

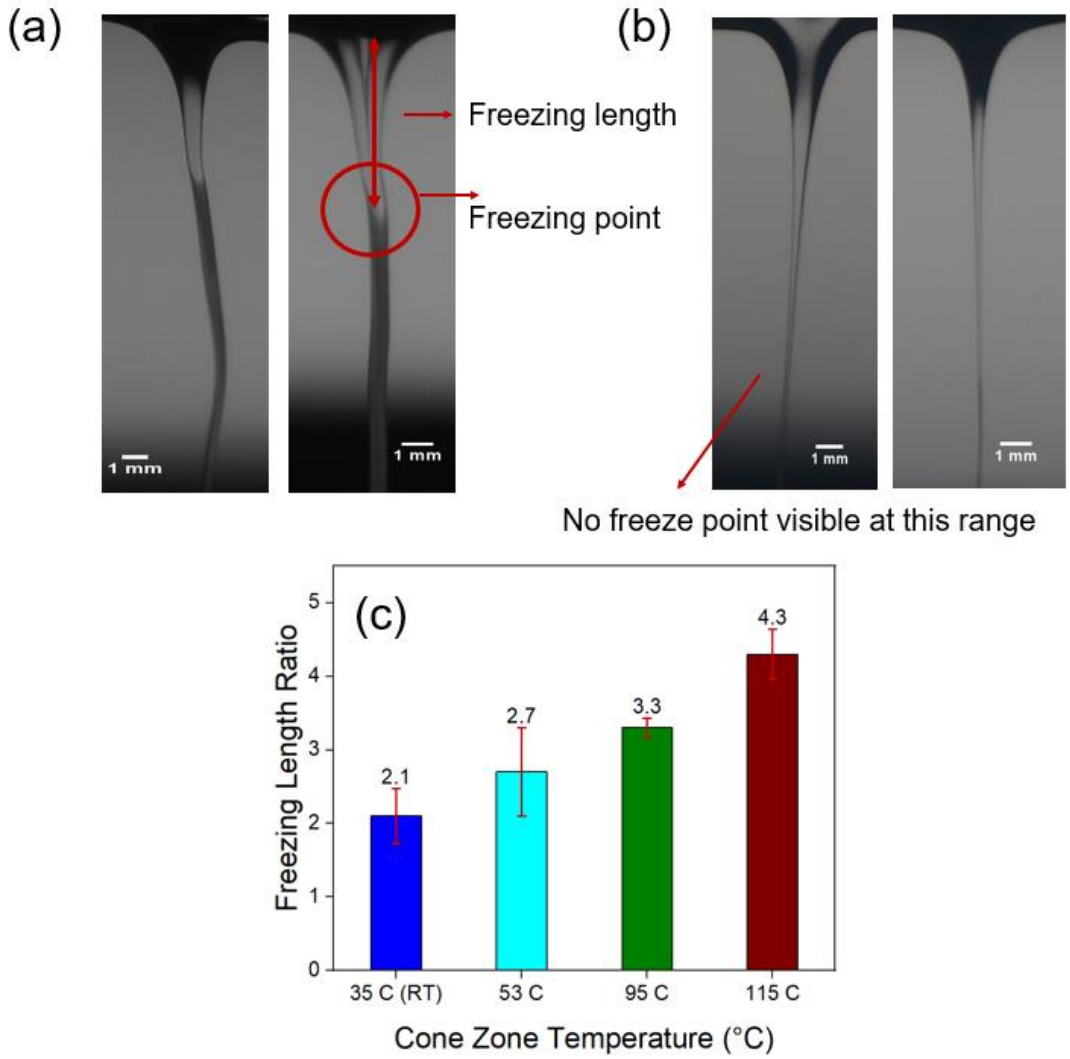

Figure 3.7. The illustration of the freezing point and freezing length through the jets taken in-situ utilizing backlighting technique for (a) room temperature (RT) spin-line profile and (b) 115 °C spin-line temperature profile. (c) the freezing length ratio calculated for the different spin-line temperature profiles.

3.3.4. Computational fluid dynamic simulation

The phase change process of the jet through the heat transfer with the spin-line environment is simulated based on the computational fluid dynamic approach. Figure 3.8-a shows the liquid phase fraction of the jet throughout the spin-line for the four different spin-line profiles. It is observed that the phase change starts at a relatively short distance from the cone for all the cases

(deviation after 1 cm in the graph of Figure 3.8-a), and the solidification process is approximately completed within the first 1.5 cm of the jets (Figure 3.8-b) (2D images are provided in the Appendix Figure A-1.4). Based on both experimental results obtained from backlit images and simulation, the length of the liquid fraction is relatively small compared to the full length of the jet (1.5 cm to 10 cm), highlighting the limited accessibility of the fluid portion to undergo extensive stretching via electric force. This can also justify the absence of the whipping motion in the melt electrospinning process, as the major portion of the jet exists in the solid phase. The shortage of the stretchable fluid phase in the jet dictates the importance of the role of freezing length on the final fiber diameter.

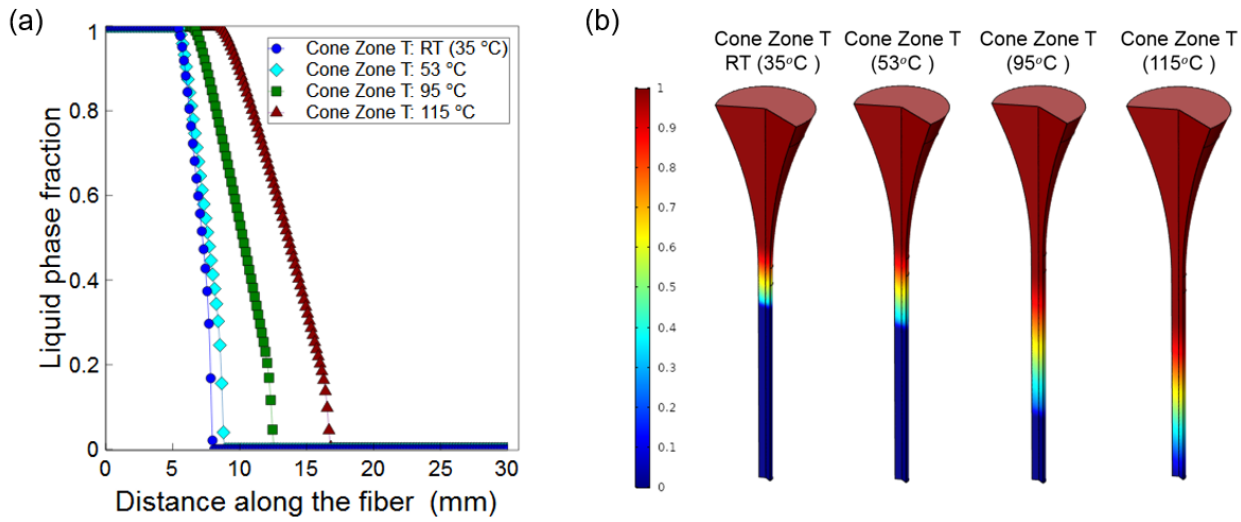

Figure 3.8. (a) Variation of the liquid phase fraction along the fiber for different spin-line temperature profiles, (b) 3D phase fraction distribution inside fiber jets. The picture shows the first 15 mm distance from the cone of fibers.

The backlit images revealed a longer freezing length of approximately 1.5 cm for the jets in the highest spin-line temperature profiles (115 °C) compared to the 0.7 cm in the lowest temperature profile (RT). The results of the simulation and its comparison with corresponding experimental data are presented in Figure 3.9 (a-b). Freezing lengths of the jets for each case of the spin-line temperature profiles were chosen and compared to the simulation results for further

validation. Deviation of the model's prediction results from the experimental for all cases (Table 3.1) shows both are in good agreement. The results from the simulation further validated the observation of the solidification point and the longer freezing length of the higher spin-line profiles. A higher deviation of the simulation results from the experiment for the case of 95 °C and 115 °C profiles is observed compared to the two lower temperature profiles. This is attributed to the effect of the surrounding air velocity that is more significant in the case of mode 1 configuration (Figure 3.2), in which the heater is directly facing the spin-line. The direct exposure of the heater creates convection heat movements in the surrounding air of the spin-line, which enhances the heat transfer of the jet. Therefore, the experiment results show a relatively smaller freezing length compared to the simulation, as the exact air velocity was not considered in the simulation due to the difficulty of the measurement. The effect of the air velocity was previously mentioned by Joo et al. as electrohydrodynamic quenching.[27]

Table 3.1. Predicted values of the freezing line by simulation and experiment and relative errors.

	Freezing length from the fiber cone (mm)			
Cone-Zone Temperature (spin-line profile)	**Cone zone T: RT**	**Cone zone T: 53 °C**	**Cone zone T: 95 °C**	**Cone zone T: 115 °C**
Experiment	7.0 ±3.2	8.3 ±1.9	10.3 ±2.3	14.8 ±5.1
Simulation	6.3	7.6	13.6	20.3
Relative error	10 %	8 %	32 %	37%

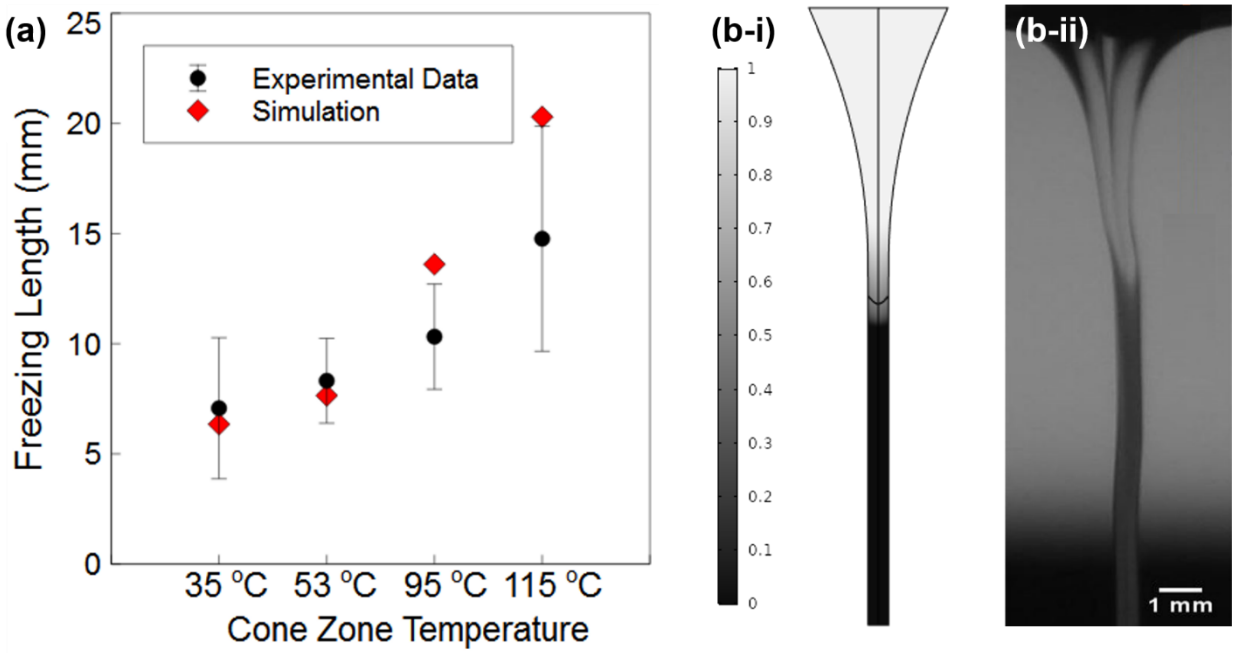

Figure 3.9. Experimental vs. simulation results. (a) Values of freezing front for different air temperatures, (b) Snapshot of freezing front for case 1; (b-i) simulation, (b-ii) experiment.

To understand the effect of the spin-line temperature on the jet viscosity, the temperature of the outer layer of the jet was calculated via simulation and is demonstrated in figure 3.10 (a-b) (The jet centerline temperature distribution graph along with the 2D images is provided in the supporting information Figure A-1.5 and Figure A-1.6). As it can be seen in figure 3.10-a, the slope of the temperature graphs decreases at the distance of about 1 cm from the fiber cone (plateaus). This can be attributed to the start of the phase change process in this region. The latent heat released during the solidification process slows down the decrease of the temperature along the fiber and lowers the slope of the diagrams. Figure 3.10-b demonstrates the non-solidified portion of the jet for each of the cases. It is observed that the length of the plateau region is longer at higher spin-line temperature profiles, which highlight the slower heat transfer of the jet inside a higher temperature environment due to the lower temperature gradient. Moreover, with increasing

the fiber velocity, we expect an elongated phase change region, and therefore, the length of the plateau for the “cone zone T: 115 °C” is more than others as this case has the highest velocity.

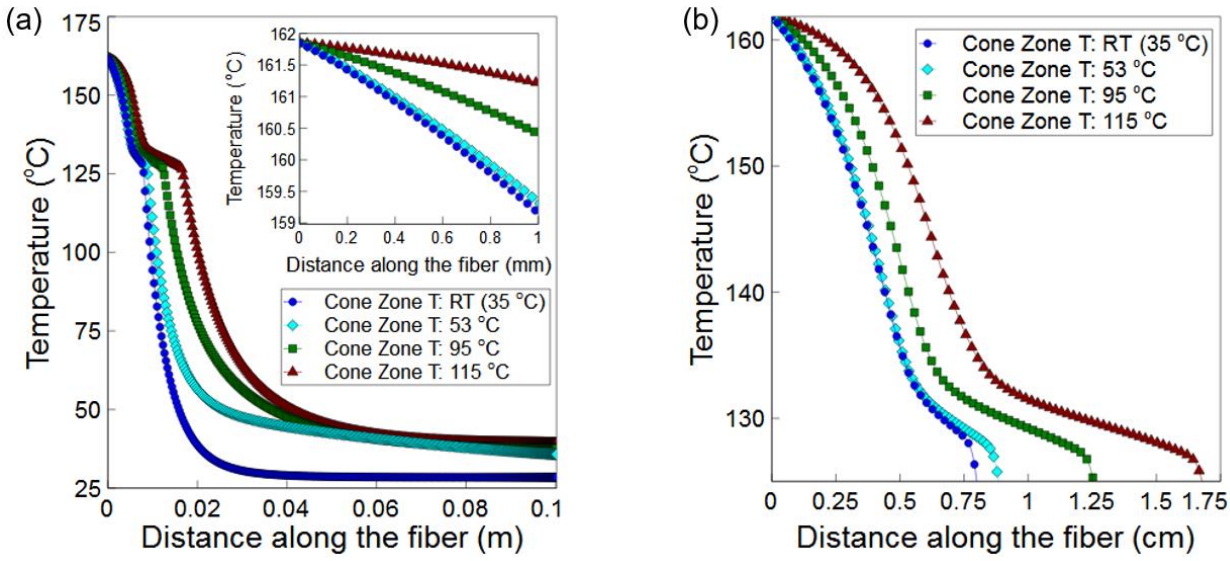

Figure 3.10. Variation of the fiber temperature at its outer layer for different spin-line air temperature profiles (a) for the full 10 cm length of the jet (b) the non-solidified region of the jet.

3.3.5. Lowering Fiber Diameter through Cone size adjustment: Regulating melt thickness

Unlike conventional approaches where a nozzle or spinneret controls the formation of the Taylor cones, in free surface electrospinning, cones are formed freely without confinement. The lack of physical confinement proposes randomness in the cone formation process and signifies the role of the fastest forming instabilities as a result of the interaction of the electric field and surface tension. However, polymer melt thickness on the plate was identified as a semi-physical confinement parameter, resembling the role of the spinneret in the conventional approaches that shows a significant effect on the cone and final fiber diameter as well as the maximum number of the formed cones. The observation shows that cone diameter decreases by decreasing melt thickness, which ultimately results in a lower fiber diameter (Figure 3.11-a). This is because

formed cones tend to maintain their circular cross-section to decrease their surface energy; hence lower melt thickness results in lower cone diameter (Figure 3.11 (a-b)). The significant decrease in the cone size (by almost twice) leaves more free space between two adjacent cones, and this explains the observed higher jet number after 20 minutes. Figure 3.11-c

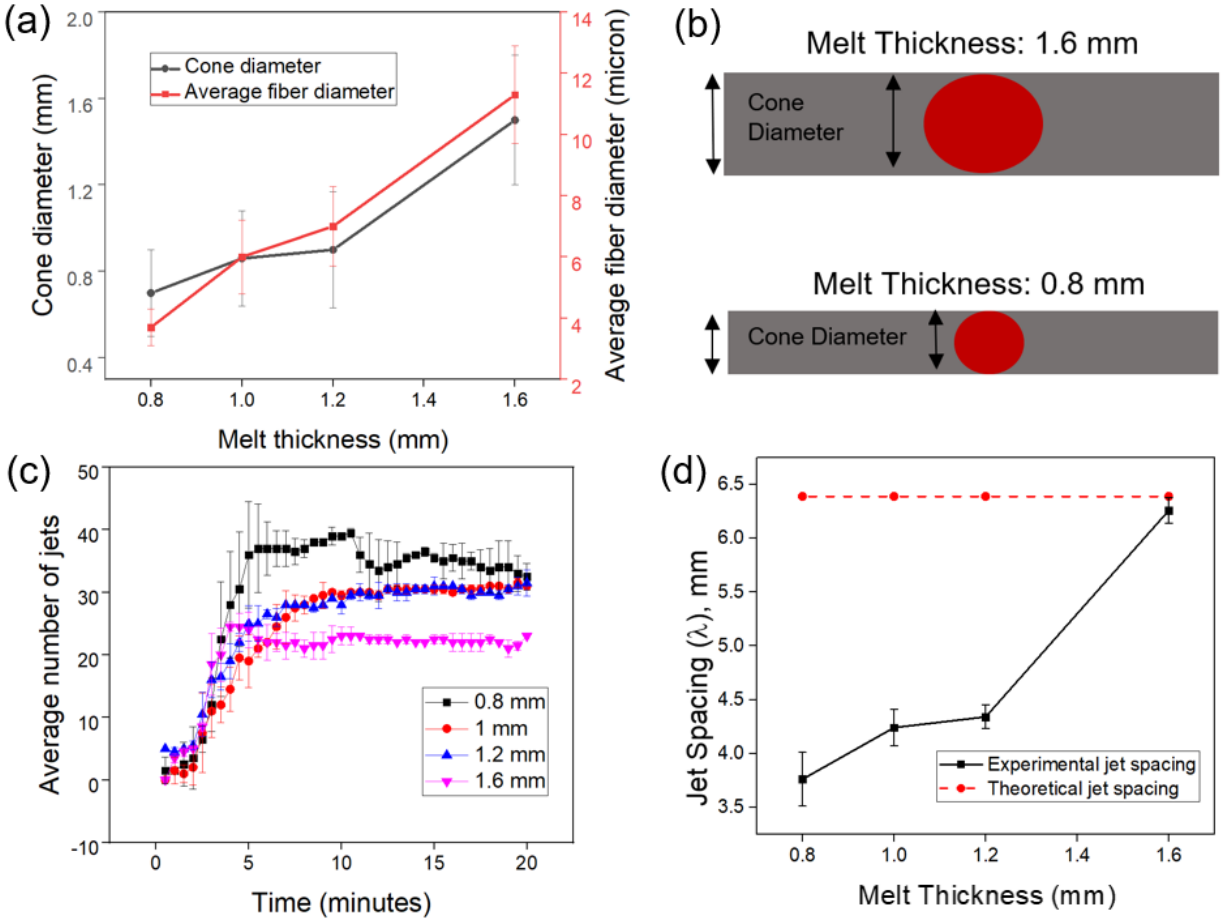

Figure 3.11. (a) Average cone diameter and fiber diameter vs. four different melt thicknesses (b) schematic of the cross-section of the formed cones from the thickness of the polymer melt on the source plate edge (c) average jet number vs. time for four different melt thicknesses (d) theoretical and experimental jet spacing for various melt thicknesses. Processing conditions: voltage: 35 kV, distance: 7.5 cm, melt temperature:165 ̊C ± 2 at spin-line temperature profile of 115 °C.

Figure 3.11-c demonstrates that by decreasing the thickness from 1.6 mm to 0.8 mm, the maximum jet number after 20 minutes of the process increases to almost twice. The theoretical

and experimental jet spacing is calculated and reported in Figure 3.11-d. For various thicknesses. The jet spacing data vary between 3 and 6 mm and are very well correlated with the theoretical results. Based on the equation, jet spacing (or jet number) results from an interaction between electric field and surface tension. However, by changing melt thickness, it is observed that jet spacing decreases to almost half the amount. This can be due to the excess of the free space resulting from a smaller cone size in lower melt thicknesses. (it was also previously observed that cones crowdedness lowers the initiated cone diameter).

3.4. Conclusions

Controlling the spin-line temperature provides a viable approach to control fiber morphology, including fiber diameter and uniformity in a melt electrospinning process, without the need for direct control over the polymer melt temperature. We reported that higher spin-line temperature shows an improvement on the maximum of the jet number, hence increases the production rate and the uniformity of the jet spacings with an enhanced correlation with the theoretical data. Increasing the spin-line temperature from room temperature up to slightly lower than the polyethylene melting temperature, covering full ranges of the environment temperature possible to attain fibers (above melting temperature jets do not solidify in time to form fibers), demonstrated a significant effect on fiber diameter reduction and uniformity of the diameters. We have implemented a unique visual technique of backlighting imaging that measures the non-solidified portion (freezing length) of the spinning jet, which was further validated via numerical simulation.

To elucidate the mechanism of the jet thinning and fiber diameter change with respect to the spin-line temperature, two hypotheses were examined: first, the effect of the cone-zone

temperature on the surface tension and subsequently the reduction of the initial cone diameter as smaller cones produce thinner jets. This hypothesis was ruled out as the visual analysis of the cone diameter both at the initiation and at the final stage of the experiments did not show a trend with cone-zone temperature. The second hypothesis was revolved around the jet-dependent parameters, including viscosity, jet solidification location, and freezing length. Both the in situ backlit images from the jet in the spin-line and the numerical simulation revealed delayed solidification (higher freezing length) at higher spin-line temperatures. We demonstrated that a major portion of the jet in the spin-line exists in the solid phase, which does not attribute any stretchability (not enough chain mobility in the solid phase). Therefore, even an infinitesimal change in the freezing length plays an important role in the jet tinning process, highlighting the role of the translocation of the solidification point on fiber diameter reduction. To investigate the role of viscosity, the jet temperature profile both inside and on the outer layer of the jet was obtained numerically. The temperature of the fully liquid phase portion of the jet (varies approximately between 0.7 cm to 1.5 cm for the room temperature and the 115 °C profiles, respectively) differ to some extent for different spin-line temperature profiles, which proposes the possibility of the viscosity reduction effect on the jet thinning mechanism. The overall observation highlights the overrated importance of the translocation of the solidification point via spin-line temperature adjustment in controlling the fiber morphology which is mostly overlooked in the literature compared to the other parameters such as melt temperature and viscosity.

In many melt phase fiber fabrication techniques such as melt spinning, a viable approach to tune fiber diameter is through increasing the melt temperature largely above the melting point to decrease the viscosity. This approach encompasses limitations due to the polymer degradation at prolonged exposure to the elevated temperature, as well as the limitation of the critical viscosity

to maintain a continuous spinnable jet. The fundamental analysis of the spin-line temperature effect on the solidification point and the subsequent jet thinning that was presented here introduces an alternative approach for fiber morphology attunement in melt phase fiber fabrication techniques in addition to extending the scope of the melt electrospinning application towards nanofibers fabrication.

Acknowledgement

This work was supported by the "National Science Foundation (NSF)" grant CMMI 1635113. The authors thank Taslim Ur Rashid for his extensive advices on the preparation of this manuscript, Mr. Phillip Strader for assistance with SEM measurements at the AIF center, Rebecca Komer for assistance with the experiments, Chengxi Li for the design of the chamber, Brent Boland for discussions and advices on the electric field simulation, Ms. Birgit Anderson for the differential scanning calorimetry, Mr. Hai Bui for technical assistance with the source plate fabrication, and NC State University libraries for use of digital SLR cameras. Authors would like to acknowledge Dr. Laura Clarke and Dr. Jason Bochinski for their advices.

3.5. References

(1) Bera, B. Literature Review on Electrospinning Process (A Fascinating Fiber Fabrication Technique). IJIR 2016, 2, 972–984.

(2) Teo, W. E.; Ramakrishna, S. A Review on Electrospinning Design and Nanofiber Assemblies. Nanotechnology 2006. https://doi.org/10.1088/0957-4484/17/14/R01.

(3) Wang, C.; Yan, K.; Lin, Y.; Hsieh, P. C. H. Biodegradable Core / Shell Fibers by Coaxial Electrospinning: Processing, Fiber Characterization, and Its Application in Sustained Drug Release. Macromolecules, 2010, 43, 6389–6397. https://doi.org/10.1021/ma100423x.

(4) Ye, P.; Xu, Z.; Wu, J.; Innocent, C.; Seta, P. Nanofibrous Membranes Containing Reactive Groups: Electrospinning from Poly (Acrylonitrile- Co -Maleic Acid) for Lipase Immobilization. Macromolecules 2006, 39, 1041–1045. https://doi.org/10.1021/ma0517998.

(5) Gentsch, R.; Pippig, F.; Schmidt, S.; Cernoch, P.; Polleux, J.; Hans, G. B. Single-Step Electrospinning to Bioactive Polymer Nanofibers. Macromolecules 2011, 44, 453–461. https://doi.org/10.1021/ma102847a.

(6) Ma, M.; Mao, Y.; Gupta, M.; Gleason, K. K.; Rutledge, G. C. Superhydrophobic Fabrics Produced by Electrospinning and Chemical Vapor Deposition. Macromolecules 2005, 38, 9742–9748. https://doi.org/10.1021/ma0511189.

(7) Shi, X.; Xu, Z.; Huang, C.; Wang, Y.; Cui, Z. Selective Swelling of Electrospun Block Copolymers: From Perforated Nanofibers to High Flux and Responsive Ultrafiltration Membranes. Macromolecules 2018, 51, 2283−2292. https://doi.org/10.1021/acs.macromol.8b00220.

(8) Laforgue, A.; Robitaille, L. Production of Conductive PEDOT Nanofibers by the Combination of Electrospinning and Vapor-Phase Polymerization. Macromolecules 2010, 43, 4194–4200. https://doi.org/10.1021/ma9027678.

(9) Long, Y.; Chen, H.; Yang, Y.; Wang, H.; Yang, Y.; Li, N.; Li, K.; Pei, J. Electrospun Nanofibrous Film Doped with a Conjugated Polymer for DNT Fluorescence Sensor. Macromolecules 2009, 42, 6501–6509. https://doi.org/10.1021/ma900756w.

(10) Yarin, A. L.; Zussman, E. Upward Needleless Electrospinning of Multiple Nanofibers. Polymer (Guildf) 2004, 45, 2977–2980. https://doi.org/10.1016/j.polymer.2004.02.066.

(11) Lukas, D.; Sarkar, A.; Pokorny, P. Self-Organization of Jets in Electrospinning from Free Liquid Surface: A Generalized Approach. J. Appl. Phys. 2008, 103 (8). https://doi.org/10.1063/1.2907967.

(12) Chen, H.; Li, H.; Ma, X.; He, W.; Tan, J.; Yang, W. Large Scaled Fabrication of Microfibers by Air-Suction Assisted Needleless Melt Electrospinning. Fibers Polym. 2016, 17 (4), 576–581. https://doi.org/10.1007/s12221-016-5915-z.

(13) Thoppey, N. M.; Gorga, R. E.; Bochinski, J. R.; Clarke, L. I. Effect of Solution Parameters on Spontaneous Jet Formation and Throughput in Edge Electrospinning from a Fluid-Filled Bowl. Macromolecules 2012, 45 (16), 6527–6537. https://doi.org/10.1021/ma301207t.

(14) Forward, K. M.; Flores, A.; Rutledge, G. C. Production of Core/Shell Fibers by Electrospinning from a Free Surface. Chem. Eng. Sci. 2013, 104, 250–259. https://doi.org/10.1016/j.ces.2013.09.002.

(15) Fang, J.; Zhang, L.; Sutton, D.; Wang, X.; Lin, T. Needleless Melt-Electrospinning of Polypropylene Nanofibres. J. Nanomater. 2012, 382639. https://doi.org/10.1155/2012/382639.

(16) Thoppey, N. M.; Gorga, R. E.; Clarke, L. I.; Bochinski, J. R. Control of the Electric Field-Polymer Solution Interaction by Utilizing Ultra-Conductive Fluids. Polym. (United Kingdom) 2014, 55 (24), 6390–6398. https://doi.org/10.1016/j.polymer.2014.10.007.

(17) Roman, M. P.; Thoppey, N. M.; Gorga, R. E.; Bochinski, J. R.; Clarke, L. I. Maximizing Spontaneous Jet Density and Nanofiber Quality in Unconfined Electrospinning: The Role of Interjet Interactions. Macromolecules 2013, 46 (18), 7352–7362. https://doi.org/10.1021/ma4013253.

(18) Komárek, M.; Martinová, L. DESIGN AND EVALUATION OF MELT-ELECTROSPINNING ELECTRODES. NANOCON 2010, 10, 12–14.

(19) Ko, J.; Mohtaram, N. K. Principle and Equipment of Polymer Melt Differential Electrospinning Preparing Ultrafine Fiber. NANOSTRUC 2014, 64. https://doi.org/10.1088/1757-899X/64/1/012013.

(20) Wang, Q.; Curtis, C. K.; Thoppey, N. M.; Bochinski, J. R.; Gorga, R. E.; Clarke, L. I. Unconfined, Melt Edge Electrospinning from Multiple, Spontaneous, Self-Organized Polymer Jets. Mater. Res. Express 2015, 1 (4), 45304. https://doi.org/10.1088/2053-1591/1/4/045304.

(21) Góra, A.; Sahay, R.; Thavasi, V.; Sahay, R. Melt-Electrospun Fibers for Advances in Biomedical Engineering, Clean Energy, Filtration, and Separation. Polym. Rev. 2011, 51, 265-287. https://doi.org/10.1080/15583724.2011.594196.

(22) Brown, T. D.; Dalton, P. D.; Hutmacher, D. W. Melt Electrospinning Today: An Opportune Time for an Emerging Polymer Process. Prog. Polym. Sci. 2016, 56, 116–166. https://doi.org/10.1016/j.progpolymsci.2016.01.001.

(23) Morikawa, K.; Vashisth, A.; Grimme, C. J.; Green, M. J.; Naraghi, M. Wire Melt Electrospinning of Thin Polymeric Fibers via Strong Electrostatic Field Gradients. Macromol. Mater. Eng. 2019, 304 (1), 1–9. https://doi.org/10.1002/mame.201800417.

(24) Thoppey, N. M.; Bochinski, J. R.; Clarke, L. I.; Gorga, R. E. Unconfined Fluid Electrospun into High Quality Nanofibers from a Plate Edge. Polymer (Guildf). 2010, 51 (21), 4928–4936. https://doi.org/10.1016/j.polymer.2010.07.046.

(25) Liu, Z.; Li, H.; Wu, W.; Chen, H.; Ding, Y.; Yang, W. Effect of Electric Field on Gas-Assisted Melt Differential Electrospinning with Hollow Disc Electrode. J Polym Eng 2015, 35(1), 61–70. https://doi.org/10.1515/polyeng-2014-0015.

(26) Mayadeo, N.; Morikawa, K.; Naraghi, M.; Green, M. J. Modeling of Downstream Heating in Melt Electrospinning of Polymers. J POLYM SCI POL PHYS 2017, 55, 1393–1405. https://doi.org/10.1002/polb.24394.

(27) Zhmayev, E.; Cho, D.; Joo, Y. L. Electrohydrodynamic Quenching in Polymer Melt Electrospinning. Phys. Fluids 2012, 073102 (September 2010). https://doi.org/10.1063/1.3614560.

(28) Shabani, E.; Rashid, T. U.; Gorga, R. E.; Krause, W. E. A Facile LED Backlight in Situ Imaging Technique to Investigate Sub-Micron Level Processing. Polym. Test. 2020, 92 (August), 106865. https://doi.org/10.1016/j.polymertesting.2020.106865.

(29) Alawadhi, E. M.; Amon, C. H. PCM Thermal Control Unit for Portable Electronic Devices: Experimental and Numerical Studies. IEEE Trans. Components Packag. Technol. 2003, 26 (1), 116–125. https://doi.org/10.1109/TCAPT.2003.811480.

(30) Mzad, H.; Otmani, A.; Bey, K.; Łopata, S. A Model of Water-Spray Cooling Effect on a Continuous Casting Process. MATEC Web Conf. 2018, 240. https://doi.org/10.1051/matecconf/201824005022.

(31) Matsuo, T.; Kase, S. Studies on Melt Spinning. VII. Temperature Profile. J. Appl. Polym. Sci. 1976, 20, 367–376.

(32) Capone, C.; Landro, L. Di; Inzoli, F.; Penco, M.; Sartore, L.; Vinci, L. Thermal and Mechanical Degradation During Polymer Extrusion Processing. Polym. Eng. Sci. 2007, 4–10. https://doi.org/10.1002/pen.

(33) Stutz, H.; Po, P. Surface Tension, Interfacial Tension, and Morphology in Blends of Thermoplastic Polyurethanes and Polyolefins. Part I. Surface Tension of Melts of TPU Model Substances and Polyolefins. Polymer 2002, 43, 6965–6972.

CHAPTER 4: Effect of the Spin-line Temperature Profile on the Mechanical Properties of Melt Electrospun Polyethylene Fibers

Elnaz Shabani, Russell E. Gorga*

Fiber and Polymer Science Program, Wilson College of Textiles, North Carolina State University, 1020 Main Campus Drive, Raleigh, North Carolina 27606, United States
*Corresponding author: Russell E. Gorga, Email Address: regorga@ncsu.edu

This chapter is under review as a manuscript in the Journal of Applied Polymer Science (Wiley Publications).

Abstract

The covid-19 pandemic has revealed the need for alternative production approaches with low startup costs like electrospinning for filter needs, the most imperative element of the personal protective equipment (PPE). Current attempts in advancing melt electrospinning deal with developing strategies for fiber diameter attenuation toward sub-micron scale. Here we utilize the attunement in the spinning-zone temperature known as "spin-line temperature profile" as baseline for fiber diameter reduction. We report the mechanical performance of the melt-electrospun linear low-density polyethylene (LLDPE) fibers to characterize their structural transformation with respect to various spin-line temperature profiles. With an increase in the spin-line temperature to above 100 °C in the area of cone formation, we demonstrated increased tensile and yield strength along with fiber diameter reduction by four-folds. We observed a significant increase in toughness, by almost three times, without compromising the stiffness and Young's modulus. The dynamic mechanical analysis revealed that spinning in high temperatures produces changes in the alpha (α) relaxation, contributing to the significant increase in strain at break. These results are significant because polyolefin fibers are an imperative element of medical textiles and PPE. Therefore, developing a correlation for process-structure-properties for emerging production techniques like melt electrospinning becomes critical.

Keywords*:* Melt Electrospinning, Mechanical properties, Polyethylene, Polymer fibers, Dynamic mechanical analysis

4.1. Introduction

Electrospinning, a versatile form of process for fabricating micron to sub-micron fibers with control over the morphology and chemical composition, has found utility in multiple industries, including filtration[1], medical textiles[2], industrial catalysis[3], biosensors[4], and within biomedical for drug delivery and tissue engineering[5,6]. The capability to produce sub-micron fibers with high precision coupled with the low startup costs makes electrospinning an attractive option for industrial upscaling. Despite many advantages, the low production rate of electrospinning remains a bottleneck for fully thriving in a fast-paced industrial environment. To overcome this hurdle, attempts have been focused on developing the multi-nozzle setups[7] as well as a free surface platform where multiple jets can be formed simultaneously[8]. Commodity polymers such as polyolefins, despite many applications, especially in medical textiles and hygienic products[9], have been largely absent from the list of the polymers electrospun so far. Polyolefins are not readily soluble at room temperature in any solvent and this limitation poses a huge hindrance to the development of electrospinning as a viable process for polyolefin sub-micron fiber fabrication.

Melt electrospinning which uses the polymer melt directly as the spinning fluid has been a viable technique for electrospinning a range of polymers, including thermoplastics and polyolefins with high production rate[10,11]. Melt electrospinning presents more challenges than conventional electrospinning due to 1) the need for elevated temperature and control, 2) decreased electrical conductivity, 3) high viscosity, and 4) relatively larger fiber diameter compared to the solution counterparts. Free surface melt electrospinning, introduced first in 2010[12], proposes new avenues into upscaling the process with reduced challenges of pumping a highly viscous fluid through a tiny needle[13,14,15]. Despite many advancements, obtaining sub-micron scale fibers from melt electrospinning remains challenging. Efforts have been taken to reduce the fiber diameter by

processing parameters attunement such as electric field intensity and molecular structure[16], incorporating plasticizing agents or ionically conductive additives[17,18,19], and controlling the spinning zone temperature[20,21,22,23,24]. Among all, the spin-line temperature control has been shown to be promising in significantly reducing the fiber diameter. It was first explored by Joo et al. that creating a heat chamber in the spinning zone promotes sub-micron scale fiber fabrication of polylactic acid (PLA)[25]. It was later proposed by Liu and Deng et al. that further increase in the spin-line temperature can adversely affect the fiber attenuation and an optimum point depending on the thermal properties of the fiber is desirable[22]. Despite many successes in fiber diameter attenuation through the spinning zone temperature control, precise control of the spin-line temperature and its effect on the fibers' microstructure, including mechanical and viscoelastic properties, remains unknown.

Polyethylene (PE) was first melt-electrospun by Larrondo et al.[26] and several other researchers have used low-density PE for melt electrospinning so far. The PE fibers produced have fiber diameters ranging from few microns to several hundreds of microns[27,28,26]. In application, the mechanical integrity of the electrospun material ultimately determines whether it will hold up under end-use conditions. Therefore, it is important to explore the influence of the melt electrospinning conditions and parameters on the microstructure of the formed fibers, which ultimately determines the mechanical and viscoelastic properties of the fibers. In the conventional spinning of PE, it has been shown that the post-process drawing induces a high level of chain orientation, which ultimately enhances the mechanical properties[29]. In a study done by Park et al., UHMWPE was gel electrospun at different spinning temperatures. It was demonstrated that the change in fiber diameter due to the spinning temperature in the spinning region significantly enhances the mechanical properties of the fibers[30]. On the same ground, changes in the spin-line

temperature are expected to affect the chain orientation and subsequently, the thermal and mechanical properties of the fibers. Despite several attempts in controlling the spin-line temperature to achieve fiber diameter attenuation in melt electrospinning, no systematic study has been developed to demonstrate the microstructural transformation with respect to the spin-line temperature. In this work, linear low-density PE was melt-electrospun using an unconfined melt electrospinning system. Precise control over the spin-line temperature enabled us to reduce the fiber diameter from approximately 40 microns on average to only 10 microns. The significant effect of the spin-line temperature on diameter attenuation brought up questions on the microstructural transformations of the fibers, which will be explored in this work.

4.2. Materials and Methods

4.2.1. Materials

Linear low-density polyethylene (LLDPE) ASPUN 6850 Fiber Grade Resin, with the melt index of 30 g/min under 190 °C/2.16 kg based on the datasheet provided by the manufacturer, was supplied by Dow Chemical company. PE powder was obtained with a cryogenic grinder using freezer mill grinder, SPEX CertiPrep 6750 purchased from SPEX SamplePrep. PE powder was used to create a uniform molten film on the source plate. The melting temperature of the PE (T_m), based on the obtained DSC thermogram, is 129 °C.

4.2.2. Apparatus

The unconfined melt electrospinning apparatus (Figure 4.1) consists of an aluminum sharp edge plate with a surface area of 13.6 x 4.8 cm and edge walls of 1 mm thickness and 0.8 cm height on the sides (With no wall on the sharp edge where fibers are formed). A commercial hot plate (Fisher Scientific, model: HP88857100) was used to heat the source plate in two modes: In the

first mode, the source plate is placed on the hot plate off-centered where the plate's edge protrudes for 2 cm. In the second mode, the source plate is attached to the hot plate from the back wall, and the entire plate is protruded (Figure 4.2). The two modes provide the spin-line environment with different temperature profiles discussed in more detail in section 3.1. In both modes, the entire apparatus is placed in a wooden chamber with a transparent front door and a top wall made from acrylic to observe the process. Thermal grease (Halnziye HY880) was used between the source plate and hot plate for better thermal contact. One side of the source plate is connected to a k-type thermocouple to monitor the source plate's temperature, and the opposite side of the plate is attached to the ground wire. The counter electrode consists of a square aluminum plate with a surface area of 30 x 30 cm that is connected to the negative polarity of a high voltage source (Glassman, Model FC60R2). A hand-made thermocouple holder is placed inside the chamber to measure the inside melt temperature before and after each run.

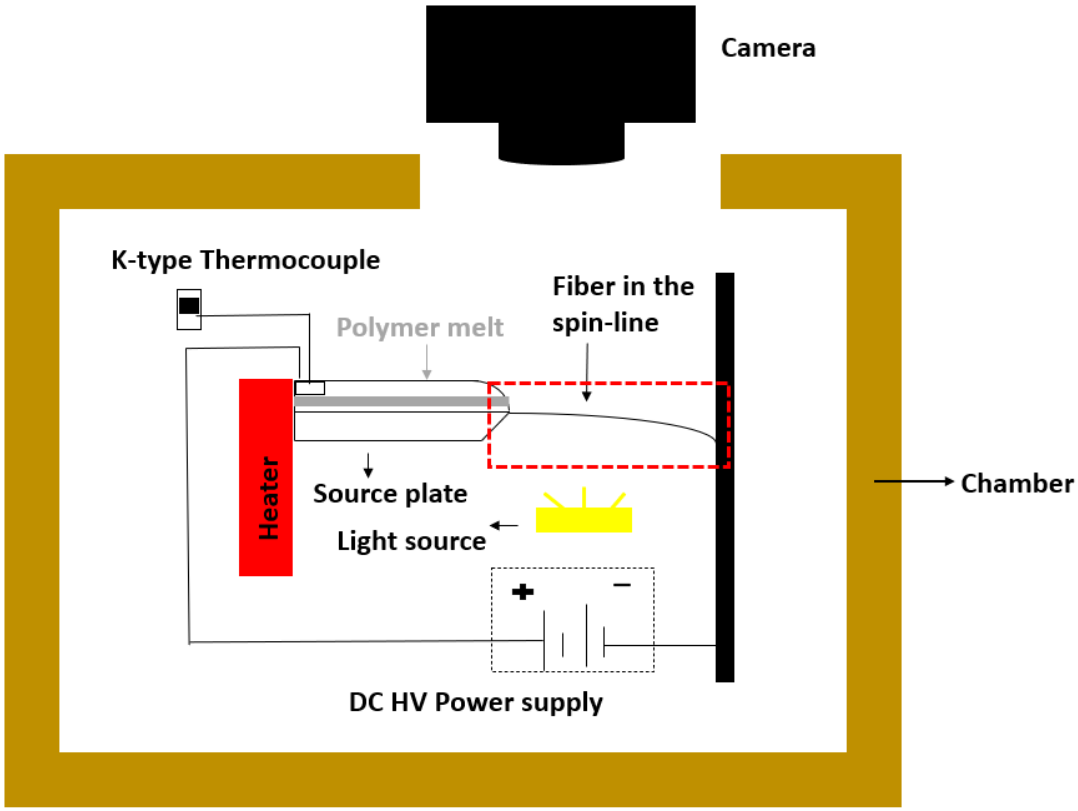

Figure 4.1. Schematic diagram of the apparatus inside the chamber from side view accompanied with a backlighting camera setup.

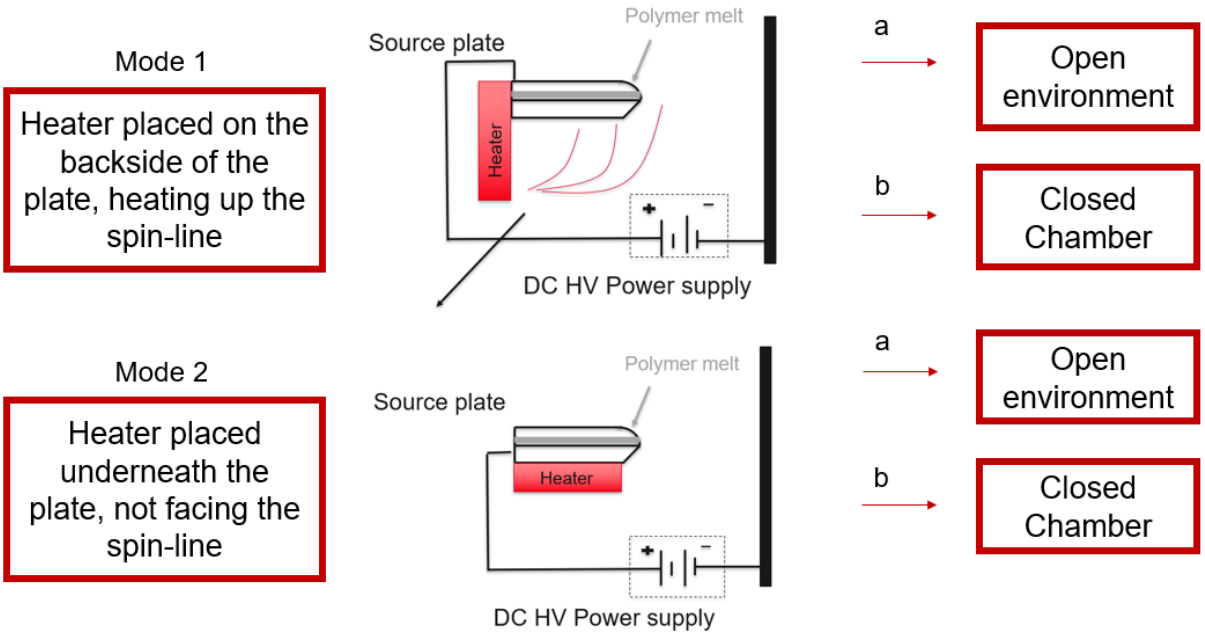

Figure 4.2. Schematic diagram of the different modes of configuration; mode 1-a (closed chamber, vertical heater), mode 2-a (open environment, horizontal heater), and mode 2-b (closed chamber, horizontal heater). Each mode provides a different spin-line temperature profile (Figure 4.3).

4.2.3. The experiment characterization

All the spinning experiments were done at the electric field of 1.84E6 V/m at 500 microns away from the plate edge. Electric field measurement was done by simulation using Ansys Maxwell software version 19.2. Voltages were set to 40 kV for the Mode 1 and 32.7 kV for the mode 2 configuration to obtain the same electric field magnitude, as simulation showed that the plate protrusion affects the electric field around the edge, which can result in a different electric field for the two modes. The spinning distance was set to 10 cm. The source plate was set to 190 °C by which the temperature of the inside molten film on the plate reached 165 ± 2 °C and was almost constant throughout the running process for all the experiments with +2 °C increase after 20 minutes, which is assumed to be negligible. Still images were taken by a Canon DSLR camera (Canon EOS Rebel T5i with 18-135mm EF-S IS STM Lens) for backlighting image analysis. Each

experiment was repeated three times, and averaged results were reported. Backlighting technique[31] was developed to obtain high-resolution images with clear object edges for further size analysis using Image J. In this technique, a wireless portable LED lamp (33 LED Super Bright Wardrobe Lights, Portable Magnetic Stick Wireless, geometry 9.5 inch by 1.5 inches by 0.7 inches, manufacturer: CHNXU) was placed in the spinning region, shinning the camera lens directly with the spinning jets located between the camera and the lighting source (Figure 4.1). The process was begun by heating the source plate to 190 °C, and after the temperature of the plate was steady, 10 grams (except for where noted) of the polymer powder was uniformly spread on the plate. When the source plate temperature gets steady to 190 °C (experimentally, this was obtained after 15-20 minutes), the temperature of the molten polymer film was measured by inserting a thermocouple inside the melt. Lastly, the high voltage is applied between the source plate and the collector, and electrospinning starts after the induction time is passed. The induction time is the time for the waves to pass the critical growth factor to prevail the formed waves on the fluid's surface beyond the critical electric field and turn in to the perturbations.

4.2.4. Fiber Characterization

The fiber mat morphology was characterized using a scanning electron microscopy (SEM) (Hitachi S3200N Variable Pressure SEM) at an accelerating voltage of 5 kV. The fibers were coated using a sputter coater with Au-Pd with a thickness of approximately 50 nm to form a conductive surface. To analyze the fiber diameter from the SEM images, the ImageJ software analyzer was used. For each sample, approximately 50 fibers were analyzed using at least 3 SEM images from different samples, and the average fiber diameter and standard error were reported.

The crystallization and melting temperatures of the LLDPE granules and fibers were obtained by differential scanning calorimetry (DSC) (Discovery, TA Instruments). The polymer

was heated from room temperature to 160 °C with a heating rate of 5 °C/min. The degree of crystallinity was obtained using $X = (\Delta H_m - \Delta H_c)/\Delta H_m^0$ where ΔH_m was calculated by integrating the melting peak from the DSC heating curve, ΔH_c is the enthalpy of the cold crystallization peak which is zero in this work, and ΔH_m^0 is the specific enthalpy of fusion, 293.6 J/g[30].

The mechanical properties of individual fibers were measured using a tensile testing machine (Instron Model 5544 with the Bluehill software version 2.0). The sample preparation and test method are discussed in detail in the Supporting Information (Figures A-2.1-3). The strain rate of 0.4 mm/sec was used in a uniaxial tension mode, and the force as a function of strain was measured. The Young's modulus was measured using linear regression in the low strain region (from the origin to the 1 % of strain). The yield point was determined using Coplan's method in which the yield point refers to the stress given by the intersection of the tangent at the origin with the tangent having the least slope.[32] All measurements were strained up to the fracture point. For each sample, nine different individual fibers were selected, and the diameter of the fibers was measured prior to the testing using an optical microscope. (Figure A-2.1-a)

Dynamic mechanical analysis (DMA) was performed using a TA Q800 instrument with fiber tension mode. For each sample, six individual fibers were geometrically measured prior to testing. Test specimens of 1 ± 0.3 mm length fibers with an average diameter of 140 ± 40 microns were taped on the two ends (Figure A-2.4) and mounted using fiber clamps. The instrument's accuracy does not allow for measuring the force for a very delicate sample, and experimentally, we observed samples of below 100 microns show not to be in the optimum range for DMA. All samples were tested under a sinusoidal frequency of 1 Hz, pre-stress of 0.01 N, the amplitude of

15 microns, and heating rate of 3 °C/min from -130 °C to 80 °C. Storage modulus and loss modulus were measured as a function of temperature.

4.3. Results and Discussion

4.3.1. Characterization of unconfined melt electrospinning

The unconfined melt electrospinning was used to fabricate polyethylene fibers ranging from 43 to a few microns.[33] Here, we utilized a spin-line temperature control system to create fibers with different diameters and morphologies. Figure 4.3-a shows the three spin-line temperature profiles in which the spinning process takes place. Spin-lines are identified by their respective cone-zone temperature. The cone zone is the region 0.5 cm off the plate edge into the spin-line where the initial cones are formed. Figure 4.1-b

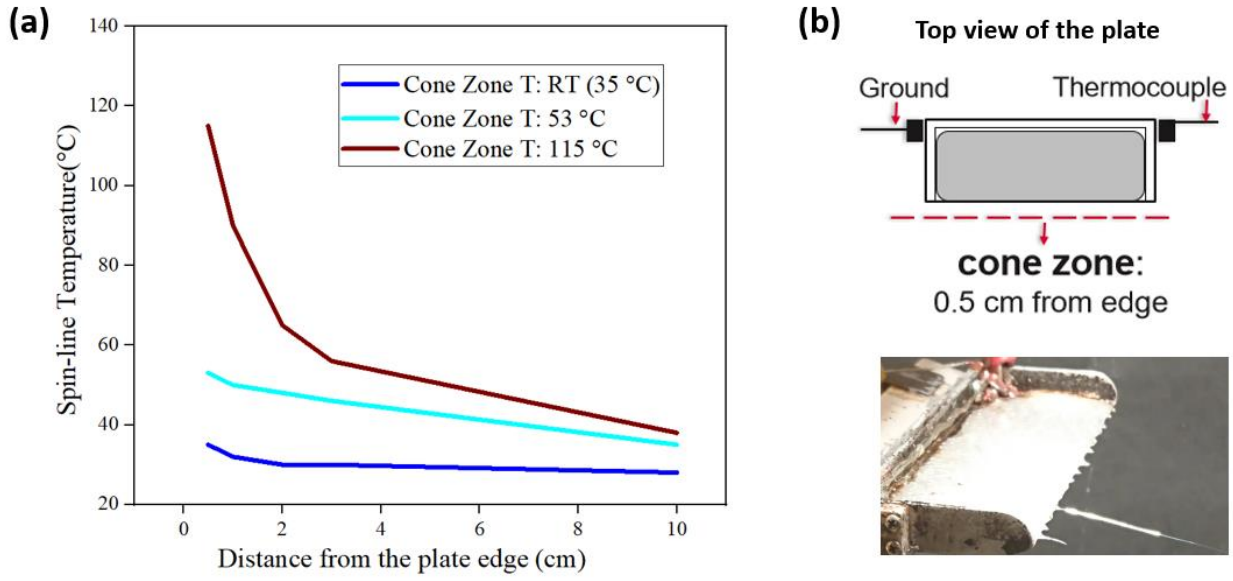

Figure 4.3. (a) Spin-line temperature profiles obtained by various configurational modes discussed in Figure 4.2. The temperatures are measured by a thermocouple placed inside the chamber. Profiles are identified by their respective cone-zone region temperature which is a region 0.5 cm in the spin-line where cones are formed. (b) schematic of the cone zone region along with the illustration of the formed cones on the plate edge.

The three spin-line temperature profiles of room temperature, 53 °C, and 115 °C were chosen based on the PE's thermal properties obtained via DSC. (Figure A-2.5) Room temperature is the most common case in many of the spinning processes. The 115 °C profile was chosen as this is the closest temperature to the melting point of the PE (129 °C) in which the spinning and fiber formation was viable. The 53 °C temperature was chosen as a profile between the other two and relatively close to the α-relaxation temperature, discussed in section 4.3.4.

The spin-line temperature control is reported to be promising in precisely controlling the solidification and jet thinning process. The backlighting technique developed by Shabani et al.[31] was utilized to monitor the solidification point along the spinning jet. Based on this system, the solidification length of the spinning jets was calculated for different spin-line temperature profiles. (Figure 4.4-a) The experimental results were further validated by temperature profile simulation inside the jet. (Figure 4.4-b) The simulation results provide detailed information on the temperature profile inside the jet (for more details of the COMSOL simulation, see appendix A-2 section 2.3). Here we utilized the information of the inside jet temperature profile along the entire spinning region (10 cm from the source plate to the collector) to further analyze the morphology and properties of the fibers.

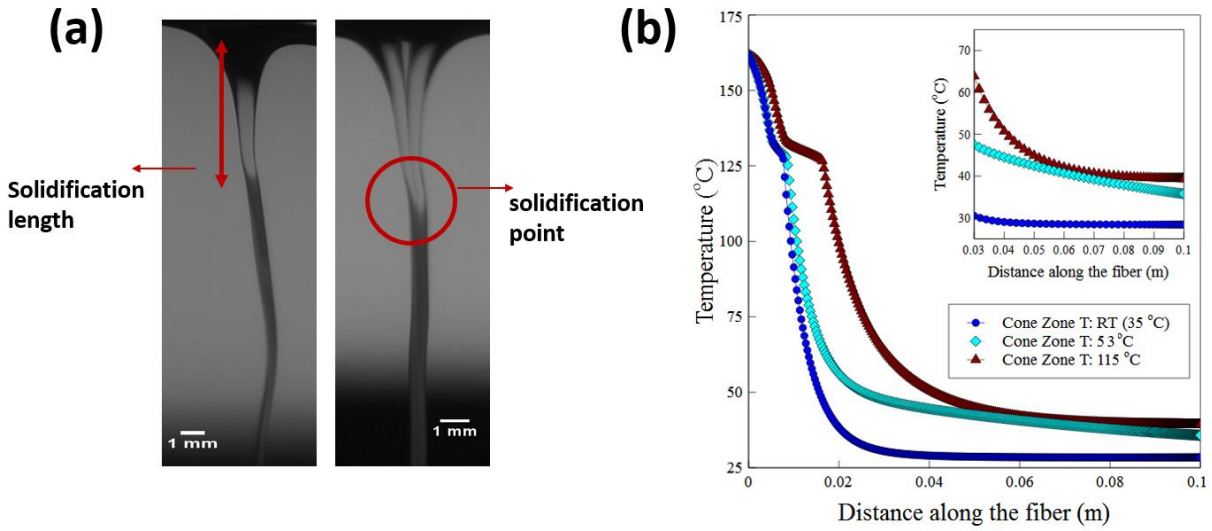

Figure 4.4. (a) An *in situ* backlit image of a single fiber jet in the spin-line. The image reveals solidification point, and the solidification length can be measured and averaged for various jets in the spin-line. The measured solidification length is reported to be 7 ± 3.2, 8.3 ± 1.9, 14.8 ±5.1 mm for the RT, 53 °C, and 115 °C spin-line temperature profiles, respectively. (b) temperature of a spinning jet calculated via computational fluid dynamic simulation. The data were further validated via experimental solidification length. The solidification length obtained via simulation is 6.3, 7.6, 20.3 mm for the RT, 53 °C, and 115 °C spin-line temperature profiles, respectively.

As is observed in Figure 4.4-b, for the two higher spin-line temperature profiles (53 °C and 115 °C), almost the entire length of the jet has a temperature above or close to 50 °C while in the room temperature case only after 2 cm the temperature inside the jet drops to approximately room temperature. This analysis is specifically important in understanding the microstructure of the formed fibers, which will be discussed in the next sections.

4.3.2. Fiber Structure Characterization

The spin-line temperature effect on the morphology and mean fiber diameter is illustrated in Figure 4.5 a-c. By increasing the spin-line temperature, the average fiber diameter decreases by four times, and the fiber diameter distribution span a narrower range showing more uniformity.

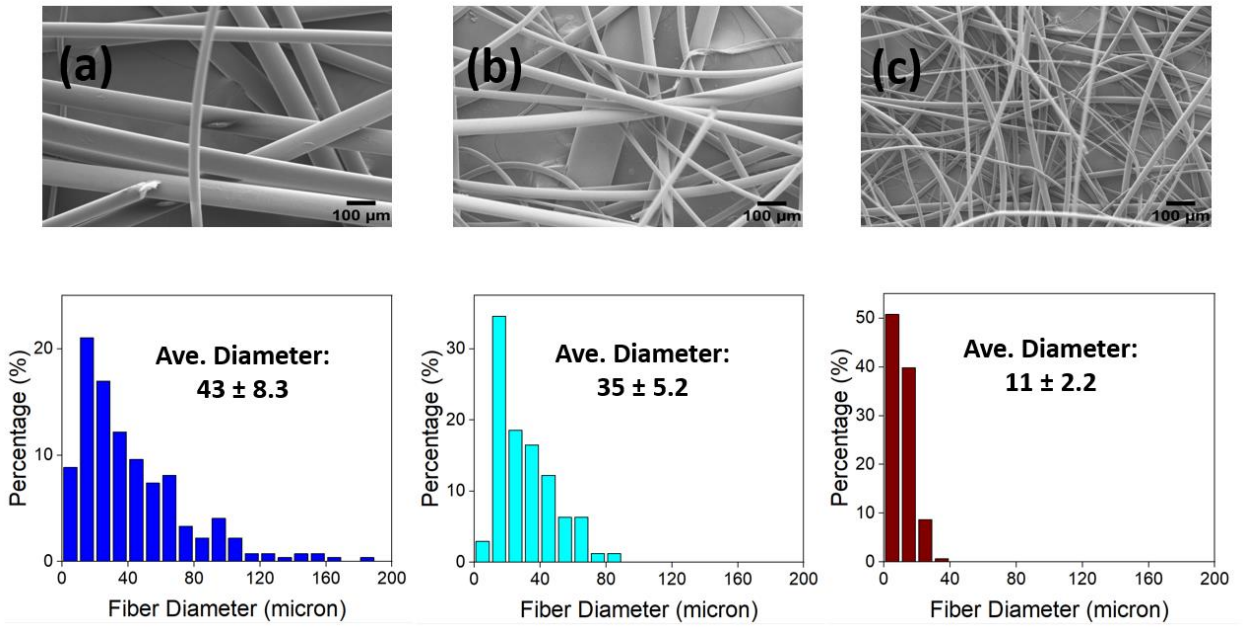

Figure 4.5. SEM images and the respective fiber diameter distribution graphs obtained for (a) Room temperature (RT), (b) 53 °C, and (c) 115 °C spin-line temperature profiles.

The main factor contributing to the significant jet thinning is the translocation of the solidification point based on the spin-line temperature profiles. Such a significant change in fiber diameter raises questions about the microstructural changes within the fibers' crystalline and amorphous regions. To better understand the crystallization behavior of the fibers, DSC runs are performed, as shown in Figure 4.6. The DSC data for the three spin-line temperature profiles are summarized in Table 4.1. The melting peak temperature remains constant with the increase in the spin-line temperature, indicating that the crystal structure does not transform significantly. It was previously reported that by applying hot drawing to UHMWPE, crystal transformation occurs from shish kebab structure to fibrillar structure. The transition proceeds by pooling elastically the inactive loops present in the folded chain lamellae of the shish kebabs, also known as taut between entanglements. The transition is evident in the melting temperature and enthalpy of crystallization that shifts to higher degrees[34].

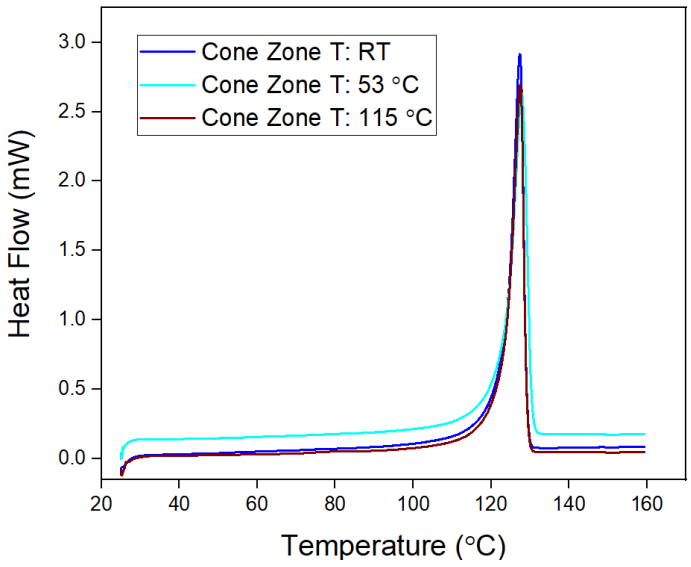

Figure 4.6. Differential Scanning Calorimetry (DSC) heating curves for fibers formed at the three spin-line temperature profiles. The heating rate is 5 °C/min.

Table 4.1. Thermal properties and degrees of crystallinity for the fibers fabricated in the spin-line temperature profiles.

Cone Zone T (spin-line profile)	**Cone zone T: RT**	**Cone zone T: 53 °C**	**Cone zone T: 115 °C**
$\boldsymbol{T_m}$ **(°C)**	127	128	127
$\boldsymbol{\Delta H_m}$ **(J** $\boldsymbol{g^{-1}}$**)**	171	174	159
$\boldsymbol{X_C}$ **(%)**	58%	59%	54%

It is observed that the crystal content does not change significantly with the change in the spin-line temperature. The fibers that are formed at a higher spin-line temperature do not show an increased degree of crystallization. This is a novel result as one might intuitively expect a higher degree of crystallization at the high spin-line temperature profiles due to the higher chain mobility and a potentially higher degree of chain orientation. However, the rapid crystallization of LLDPE molecules coupled with the fast quenching of the jets at all the spin-line temperature profiles induces the same crystallization behavior between the fibers. The same behavior was previously

observed where the crystallization of the LLDPE fibers remains constant with respect to the various take-up velocities[29].

4.3.3. Mechanical properties of the melt-electrospun fiber

Figure 4.7-a shows the engineering stress-strain curve for the individual fibers formed at the three different spin-line temperature profiles. Fibers for mechanical testing are chosen based on the proximity to the average diameter (±10%) reported for each sample from SEM. The Young's moduli are determined from the slope of linear regression in the region of small strain up to 1%. The moduli are plotted against spin-line temperature profiles for nine different individual fibers from each sample. Figure 4.7-b No dramatic difference is observed between the moduli numbers for the fibers formed at different spin-line temperature profiles, and the mean is almost constant. (Table 4.2) This observation is in line with the constant crystal content between samples from DSC as Young's modulus strongly depends on the crystallization percent of the sample.

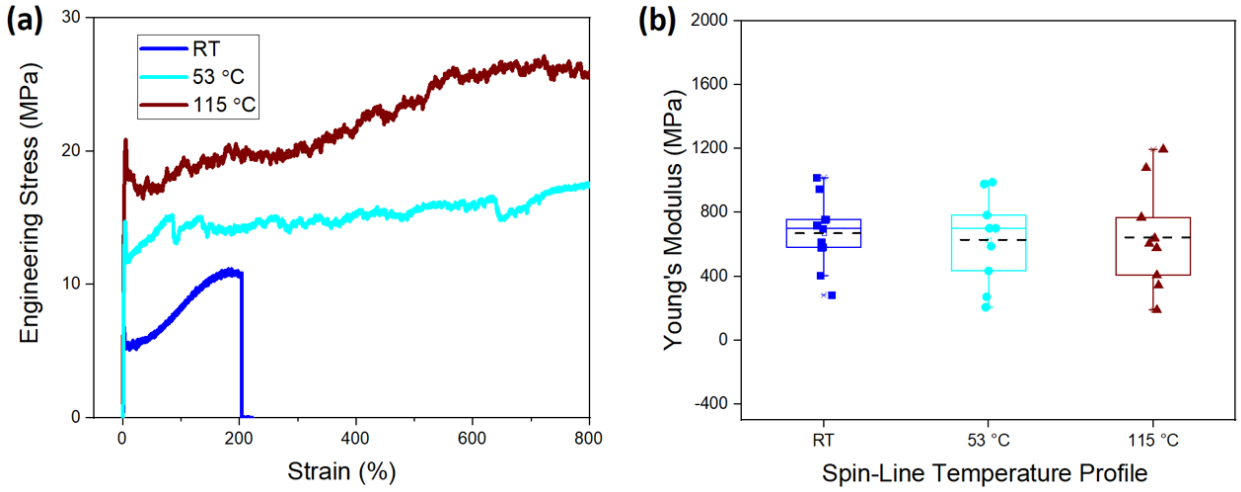

Figure 4.7. Tensile deformation behavior of melt-electrospun LLDPE fibers at the three spin-line temperature profiles. (a) Stress–strain curves for LLDPE fibers at the three spin-line temperature profiles of RT, 53 °C, and 115 °C. (b) Young's modulus versus spin-line temperature profiles for the average fiber diameters of 53 ± 3.2 microns for RT (dark blue), 37 ± 1.5 microns for 53 °C (light blue), and 16 ± 1 microns for the 115 °C (wine red) spin-line temperature profiles.

The mean Young's modulus for the samples is within the range of 700 MPa, higher than the 135 MPa Young's moduli reported for the bulk LLDPE.[35] Moreover, the single fibers moduli are higher than the 514 MPa average reported for LLDPE nonwoven mat[36]. The higher observed moduli are attributed to the high draw ratio of the electrospinning process due to the electric force. In the conventional spinning methods, e.g., melt spinning, fibers' properties have been found to be sensitive to the take-up velocity or the second stage drawing[29,37]. Here, even though one might assume that the higher spin-line temperature can facilitate the chain orientation and, therefore, the modulus, it is observed that the degree of crystallinity remains unchanged, and the moduli remain constant. As the moduli are constant, one can assume that the degree of crystallite orientation does not change dramatically between fibers formed at different spin-line temperature profiles. Figure 4.8-a shows the average tensile and yield strength measured for the single melt-electrospun fibers from the three spin-line temperature profiles. Unlike modulus, the tensile and yield strength increases by increasing the spin-line temperature by almost three times. The same behavior is observed for the toughness and strain at break (%) properties of the fibers. In addition to the spin-line temperature effect, the diameter change is also being taken into consideration and is represented in Figure 4.8-b.

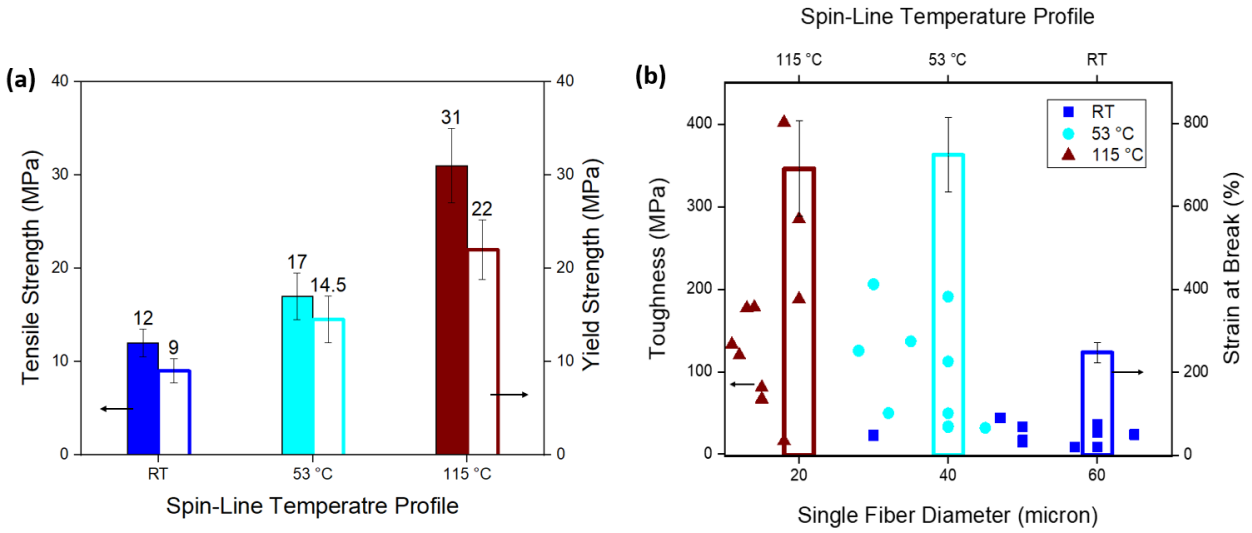

Figure 4.8. (a) Tensile strength and Yield strength for the fibers formed at the three spin-line temperature profiles of RT, 53 °C, and 115 °C. (b) Toughness and strain at break for individual fibers versus fiber diameter and averaged for the three spin-line temperature profiles of RT, 53 °C, and 115 °C.

Table 4.2. Average mechanical properties for melt-electrospun LLDPE fibers for the three spin-line temperature profiles of RT, 53 °C, and 115 °C.

Cone Zone T (spin-line profile)	**Cone zone T: RT**	**Cone zone T: 53 °C**	**Cone zone T: 115 °C**
Average Fiber Diameter (micron)	43 ± 8.3	35 ± 5.2	11 ± 2.2
Average Young's Modulus (MPa)	667±71	691 ± 88	747 ± 142
Average Tensile Strength (MPa)	12 ± 1.5	17 ± 2.5	31 ± 4
Average Yield Strength (MPa)	9 ± 1.3	14.5 ± 2.5	22 ± 3.2
Toughness (MPa)	23.5 ± 3.7	101 ± 20	165 ± 35.5
Strain at Break (%)	248 ± 24	724 ± 90	691 ± 115

First, to understand the origin of the improvements in strength and toughness with regard to spin-line temperature and fiber diameter, these properties are correlated using Griffith's theory of fracture[38] in which the tensile strength increases with a reduction in diameter, which is assumed to limit the crack length. The theory was originally developed to explain the brittle fracture of linear elastic materials. Later, the theory was adopted for plastic deformation e.g., crazes followed

by fracture[39]. Griffith's theory, that utilizes the continuum approach, recognizes that all materials contain imperfections, such as cracks or crazes in case of plastics, at which the fracture is initiated. The stress (σ) required for a crack to propagate is dependent on the crack length. Penning et al. developed a correlation between the tensile strength (σ), toughness (G_c), Modulus (E), and fiber diameter (d) such that $\sigma \sim (G_c E/d)^{\alpha}$ and $\alpha=0.5$[40]. From the log-log plot of the σ versus $G_c E/d$ shown in Figure 4.9, we obtained α value of 0.32 and Pearson's correlation coefficient of 0.9. The obtained α value is smaller than the optimal 0.5, yet it is significantly larger than the 0.19 value that Penning et al. reported for the case of UHMWPE. The number is also comparable to the 0.37 that was previously obtained for the gel-electrospun UHMWPE by Rutledge et al.[30] According to Penning et al. in order to acquire a correct dependence of the strength to the diameter, all other factors that can contribute to the strength should be isolated. Here, it is shown that fibers, regardless of their diameter and spin-line temperature, have the same modulus; therefore, differences in the fibers' strength can be directly related to the fracture process itself. Unlike Penning et al., that observed no dependence of the strength on diameter for samples with moderate to low modulus where the reported α value was as low as 0.034, here the fibers of small modulus show a relatively good correlation with Griffith's theory.

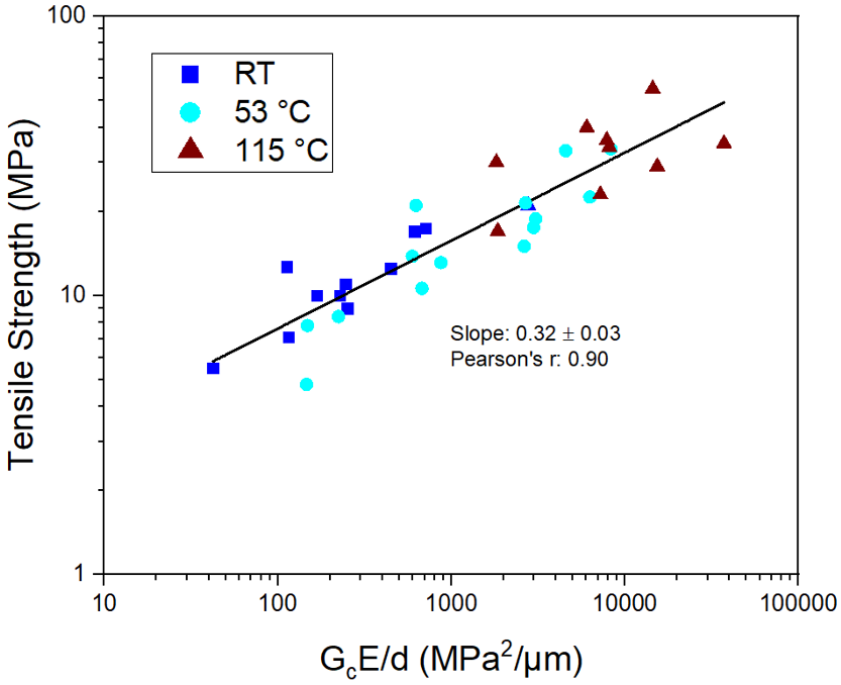

Figure 4.9. A log–log plot of tensile strength versus G_cE/d where G_c=fracture toughness (MPa), E = elastic modulus (MPa), and d = fiber diameter (micron) for the three spin-line temperature profiles of RT, 53 °C, and 115 °C. The black solid line is an empirical fit (see text for details).

4.3.4. Dynamic Mechanical Analysis

The combinations of higher toughness and extensive strain at break by increasing the spin-line temperature profiles merit further comment. As the crystalline region remains constant between samples, the attention goes towards the amorphous regions. The large degree of crystallinity (~ 60%) proposes that the amorphous region is influenced by the crystalline domains. The topology of the disordered amorphous region includes chains leaving and re-entering the same crystals, those leaving and entering a different crystal (tie chains), and randomly coiled chains in between[41]. To examine the behavior of the amorphous region that is tied to the crystalline region, dynamic mechanical analysis was carried out from the fibers formed at different spin-line temperature profiles. (Figure 4.10) In the loss modulus graphs versus temperature two relaxation peak is observed: one at the temperature of ~ -115, which is attributed to the γ transition, also

known as glass transition ($\mathbf{T_g}$). The second relaxation happens at around room temperature, which is attributed to the α-transition. It is observed that the intensity of the α-relaxation decreases with increasing the spin-line temperature from the room temperature by almost 50% and levels off at the 53 °C or 115 °C spin-line temperature profiles. (Figure 4.10 and Table 4.3).

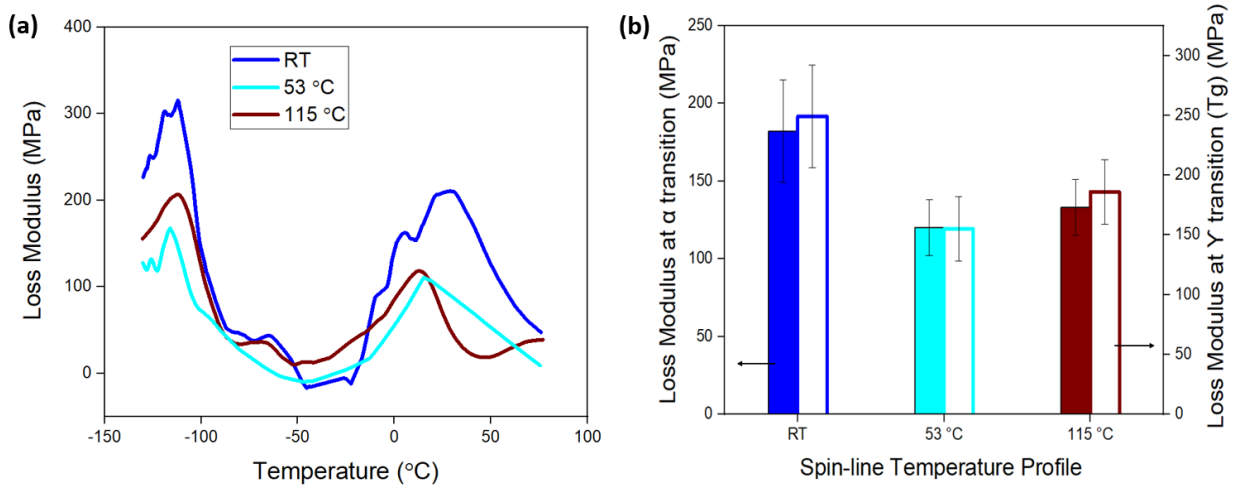

Figure 4.10. Dynamic mechanical analysis (DMA) of the individual fibers obtained from the three spin-line temperature profiles of RT, 53 °C, and 115 °C. (a) Loss modulus versus temperature from -130 °C to 80 °C (b) The loss modulus strength at α-transition and γ-transition (T_g) of the individual fibers versus spin-line temperature profile.

Table 4.3. Loss Modulus at α-transition and γ-transition ($\mathbf{T_g}$), Temperature of the α loss peak, and intensity of the storage modulus transition (S-factor) for the three spin-line temperature profiles of RT, 53 °C, and 115 °C.

Cone Zone T (spin-line profile)	**Cone zone T: RT**	**Cone zone T: 53 °C**	**Cone zone T: 115 °C**
Loss modulus peak at α transition	182 ± 33	120 ± 18	133 ± 18
Loss modulus peak at γ transition ($\mathbf{T_g}$)	249 ± 43	155 ± 27	186 ± 27
α-transition temperature	23 ± 1.7	17 ± 1.7	20 ± 1.7
S-factor[42]	0.98	0.91	0.90

The α-peak temperature, representing the lamellae thickness of the crystals, does not show a dramatic change with respect to the spin-line temperature, in line with the melting temperature data obtained from DSC. It is generally agreed that the α-transition originates with some type of

motion in the crystalline region. It has been shown that the crystal body itself would not contribute to α-transition, but it is the fold surface and the tie molecules that are necessary for the relaxation[43]. Boyd's model explains that the α-transition occurs in the amorphous phase, including the loops, folds, and tie chains, which is normally rigid without the crystal mobility[41]. It was previously shown for HDPE fibers that by increasing the hot drawing ratio, the α-relaxation strength increases. This was attributed to the high orientation of the chains that changes the microstructure of the crystalline phase[44]. The observation of the α-relaxation decrease with an increase in the spin-line profile shows that the amorphous regions in the lower spin-line profile are more oriented in the fiber length axis. This is curious as one might assume a more oriented amorphous region at higher spin-line temperature due to more chain mobility. However, according to the simulation of the jet temperature (Figure 4.4-b), for the case of room temperature profile, an extensive length of the jet has a temperature of 25-30 °C, as the curve levels off after the first 2 cm length of the jet. However, for the other two cases of the profiles, the first 5 cm of the jet has a temperature above 50 °C and the second 5 cm only levels off to approximately 40 °C (the inset of Figure 4.4-b). As the α-relaxation peak occurs approximately at room temperature and spans up to 50 °C, the latter two cases are being drawn above the α transition temperature for the amorphous chains tied to the crystalline regions (representative of the α-relaxation) to be mobile to the point that the jets can lose their chain orientations by the time they reach the collector. However, the former case quenches fast enough to maintain the orientation induced by the electric field stretching force.

The S-factor, defined as the intensity of transition from glassy state to rubbery state in storage modulus is a good indicator of the amorphous content of the material. S-factor was calculated using equation 1[42]:

$$S=\frac{\acute{E}_a-\acute{E}_d}{\acute{E}_d} \qquad (1)$$

Where $\acute{E}_a$ is the storage modulus before and $\acute{E}_d$ after the transition. The S-factor remains constant, proposing a constant crystallinity degree and amorphous region mobility between different spin-line temperature profiles. To sum it up, it is expected that the interlamellar amorphous regions in the RT spin-line temperature profile is more oriented, as opposed to the more random coiled chain configuration of the fibers formed at the two higher spin-line temperature profiles. The remarkably higher elongation at break for the two higher spin-line temperature profiles compared to the room temperature profile (700% vs. 250%) proposes less oriented chains in the axis of the fiber length, which is in line with the observations from the α-relaxation peak in the DMA. It was also previously observed that higher chain orientation reduces the stretchability of the fibers[29].

4.4. Conclusion

We report a robust mechanism for fiber diameter attenuation and its effect on the mechanical performance of the LLDPE in unconfined melt electrospinning. Precise control of the temperature in the spinning zone enabled us to fabricate fibers with only ~10 microns on average without the need for increasing the melting temperature. Obtaining such a low diameter range is extremely challenging for PE in the melt electrospinning process due to high viscosity nature and complex processability[28]. Systematic advancements in mechanisms of fiber diameter reduction in melt electrospinning, being one of the major bottlenecks for its industrial applications, merits systematic process-structure-properties correlation development carried out throughout this work. We demonstrated that increasing the spin-line temperature, specifically in the cone zone translocates the solidification point and increases the solidification length of the jet, which is identified as the major factor for the fiber diameter reduction. Increasing the spin-line temperature enhances the tensile strength, yield strength, and toughness of the products without compromising

the stiffness. Unexpectedly, spinning at higher spin-line temperature even though enhances the chain mobility, does not contribute to further chain orientation in the amorphous region and the type and degree of crystallinity remain unchanged. This enabled the fibers to achieve three times higher strain at break and toughness without compromising Young's modulus. Dynamic loss modulus strength at α-transition, which is mainly correlated to the tie molecules in the amorphous region, decreases with increasing the spin-line temperature. This indicates a lower chain alignment for the tie molecules, which justifies the extensive strain before fracture for the fibers produced at the higher temperature spinning zone. To sum up, we demonstrated that employing the strategy of spinning zone temperature increase to reduce fiber diameter creates PE fabrics with enhanced mechanical properties in unconfined melt electrospinning.

4.5. Acknowledgment

This work was supported by the "National Science Foundation (NSF)" grant CMMI 1635113. The authors thank Amir Azimi Yancheshme and Dr. Avner Ronen for the COMSOL simulation, Phillip Strader for assistance with SEM measurements at the AIF center, Patrick Hughes for assistance with the mechanical testing, Dr. Jay Hoon Park for the discussions over the mechanical properties, Chengxi Li for the design of the chamber, Brent Boland for discussions and advises on the electric field simulation, Alireza Garmabi for the discussions on the mechanical testing, Ms. Birgit Anderson for the differential scanning calorimetry, Mr. Hai Bui for technical assistance with the source plate fabrication, Mr. Gary Mann for the help with the DMA instrument and NC State University libraries for the use of digital SLR camera.

4.6. References

1. Yun, K. M., Hogan, C. J., Matsubayashi, Y., Kawabe, M., Iskandar, F., Okuyama, K. *Chem. Eng. Sci.*, **2007**, 62, 4751–4759.
2. Mouthuy, P. A., Zargar, N., Hakimi, O., Lostis, E., Carr, A. *Biofabrication*, **2015**, **7**.
3. Berber, E., Horzum, N., Hazer, B., Demir, M. M. *Fibers Polym.*, **2016**, 17, 760–768.
4. Mercante, L. A., Scagion, V. P., Migliorini, F. L., Mattoso, L. H. C., Correa, D. S. *TrAC - Trends Anal. Chem.*, **2017**, 91, 91–103.
5. Nagy, Z. K., Balogh, A., Drávavölgyi, G., Ferguson, J., Pataki, H., Vajna, B., Marosi, G. *J. Pharm. Sci.*, **2013**, 102, 508–517.
6. Agarwal, S., Wendorff, J. H., Greiner, A. *Adv. Mater.*, **2009**, 21, 3343–3351.
7. Koenig, K., Beukenberg, K., Langensiepen, F., Seide, G. *Biomater. Res.*, **2019**, 23, 1–12.
8. Yarin, A. L., Zussman, E. *Polymer (Guildf).*, **2004**, 45, 2977–2980.
9. Manjula, B., Reddy, A. B., Sadiku, E. R., Sivanjineyulu, V., Molelekwa, G. F., Jayaramudu, J., Raj Kumar, K. *Polyolefin Fibres Struct. Prop. Ind. Appl. Second Ed.*, **2017**, 539–560.
10. Brown, T. D., Dalton, P. D., Hutmacher, D. W. *Prog. Polym. Sci.*, **2016**, 56, 116–166.
11. Robinson, T. M., Hutmacher, D. W., Dalton, P. D. *Adv. Funct. Mater.*, **2019**, 29.
12. Komárek, M., Martinová, L. *NANOCON*, **2010**, 10–15.
13. Fang, J., Zhang, L., Sutton, D., Wang, X., Lin, T. *J. Nanomater.*, **2012**, 2012.
14. Thoppey, N. M., Bochinski, J. R., Clarke, L. I., Gorga, R. E. *Polymer (Guildf).*, **2010**, 51, 4928–4936.
15. Morikawa, K., Vashisth, A., Grimme, C. J., Green, M. J., Naraghi, M. *Macromol. Mater. Eng.*, **2019**, 304, 1–9.

16. Lyons, J., Li, C., Ko, F. *Polymer (Guildf).*, **2004**, 45, 7597–7603.

17. Shabani, Elnaz; Li, Chengxi; Komer, Rebecca; Clarke, Laura; Bochinski, Jason; Gorga, Russell; Boland, Brenton; Sheoran, N. Bull. Am. Phys. Soc. **2019**, 64.

18. Koenig, K., Hermanns, S., Ellerkmann, J., Saralidze, K., Langensiepen, F., Seide, G. *Text. Res. J.*, **2020**, 90, 1948–1961.

19. Nazari, T., Garmabi, H. *J. Appl. Polym. Sci.*, **2016**, 133.

20. Shen, Y., Liu, Q., Deng, B., Yao, P., Xia, S. *Fibers Polym.*, **2016**, 17, 1227–1237.

21. Doustgani, A., Ahmadi, E. *J. Ind. Text.*, **2016**, 45, 626–634.

22. Zhmayev, E., Cho, D., Joo, Y. L. *Polymer (Guildf).*, **2010**, 51, 4140–4144.

23. Kong, C. S., Jo, K. J., Jo, N. K., Kim, H. S. *Polym. Eng. Sci.*, **2009**, 49, 391–396.

24. Mayadeo, N., Morikawa, K., Naraghi, M., Green, M. J. *J. Polym. Sci., Part B: Polym. Phys.* **2017**, 1393–1405.

25. Zhou, H., Green, T. B., Joo, Y. L. *Polymer (Guildf).*, **2006**, 47, 7497–7505.

26. Larrondo, L., Manley, R. S. J. *J. Polym. Sci. Part A-2, Polym. Phys.*, **1981**, 19, 933–940.

27. Deng, R., Liu, Y., Ding, Y., Xie, P., Luo, L., Yang, W. *J. Appl. Polym. Sci.*, **2009**, 114, 166–175.

28. Morikawa, K., Vashisth, A., Bansala, T., Verma, P., Green, M. J., Naraghi, M. *Macromol. Mater. Eng.*, **2020**, 2000106, 1–7.

29. Cho, H. H., Kim, K. H., Kang, Y. A., Ito, H., Kikutani, T. *J. Appl. Polym. Sci.*, **2000**, 77, 2267–2277.

30. Park, J. H., Rutledge, G. C. *J. Mater. Sci.*, **2018**, 53, 3049–3063.

31. Shabani, E., Rashid, T. U., Gorga, R. E., Krause, W. E. *Polym. Test.*, **2020**, 92, 106865.

32. Ward, I. Mechanical properties of solid polymers, Wiley: New York, 2nd edn., **1983**.

33. Wang, Q., Curtis, C. K., Thoppey, N. M., Bochinski, J. R., Gorga, R. E., Clarke, L. I. *Mater. Res. Express*, **2015**, 1, 45304.

34. Smook, J., Pennings, J. *Colloid Polym. Sci.*, **1984**, 262, 712–722.

35. Bhasney, S. M., Bhagabati, P., Kumar, A., Katiyar, V. *Compos. Sci. Technol.*, **2019**, 171, 54–61.

36. Hidalgo-Salazar, M. A., Correa, J. P. *Results Phys.*, **2018**, 8, 461–467.

37. Smith, P., Lemstra, P. J. *J. Mater. Sci.*, **1980**, 15, 505–514.

38. Griffith, A. A. *Philos Trans R Soc A*, **1921**, 221, 163-198.

39. Williams JR. *Adv Polym Sci*, **1978**, 27, 69–120 .

40. Penning, J. P., De Vries, A. A., Ven, J. Van der, Pinnings, A. J., Hoogstraten, H. W. *Philos. Mag. A Phys. Condens. Matter, Struct. Defects Mech. Prop.*, **1994**, 69, 267–284.

41. Boyd, R. H. *Polym. Eng. Sci.*, **1979**, 19, 1010–1016.

42. Díez-Gutiérrez, S., Rodríguez-Pérez, M. A., De Saja, J. A., Velasco, J. I. *Polymer (Guildf).*, **1999**, 40, 5345–5353.

43. Khanna, Y. P., Turi, E. A., Taylor, T. J., Vickroy, V. V., Abbott, R. F. *Macromolecules*, **1985**, 18, 1302–1309.

44. Barkoula, N. M., Alcock, B., Cabrera, N. O., Peijs, T. *Polym. Compos.*, **2008**, 16, 101–113.

CHAPTER 5: Outlook and Path Forward

5.1. Introduction

This Ph.D. dissertation focuses on developing strategies to improve melt electrospinning from a free surface with regard to average fiber diameter and the corresponding microstructural transformation. This work has implications in various fields including filtration media[1,2,3,4,5], personal protective equipment (PPE)[6,7,8,9], within biopharma including drug delivery[10,11,12], and other applications[13,14,15]. This field of electrospinning has flourished within the last ten years, and significant progress has been made in the design of the free surface platforms as well as the strategies to improve fiber diameter and distribution ranges. However, it is the opinion of the author that significant advancement is still needed for commercialization of the melt electrospinning. For instance, limitations like low production rate, relatively large fiber diameter compared to solution electrospinning, and the complexity in the design of the heating modules all require further investigations prior to full commercialization. To unpack these challenges, a variety of areas of improvement are discussed below that the author believes to be key elements for future researchers.

5.2. Areas of improvements

5.2.1. Fiber diameter attenuation challenge

Fibrous structures are distinctive from bulk materials due to their high aspect ratio of surface area to the volume. This attribute enables them to perform best in numerous areas such as filtration to trap small size aerosols and pollutes, composites materials, catalysts support, and drug delivery with enhanced drug release depending on the extent of the fibers surface area[16]. An excellent example to illustrate the importance of fiber diameter and morphology is the current respirators and surgical masks made of melt-blown polypropylene (PP) fibers, that are typically above micron size, and therefore, they mostly rely on the electrostatic charges to repel sub-micron

particles. Upon decontamination, electrostatic charges are lost, which makes the masks to be single-use equipment. One way to boost their efficacy for filtering sub-micron particles is to reduce the fiber diameter to bellow micron size. Therefore, for emerging fabrication alternatives like melt electrospinning to come in use, attempts always revolve around proposing strategies to decrease fiber diameter while maintaining the overall morphology and robustness of the process. Despite many advancements in this realm, obtaining nanofibers from melt electrospinning remains challenging[17,18,19,20,21,22,23,24,25].

As an option to combat this limitation, this Ph.D. dissertation explored the attunement of spinning zone temperature to control the heat transfer and the subsequent solidification of the jet. With the development of an efficient imaging technique (chapter 2), we demonstrated that melt electrospun jets undergo a fast quenching. Utilizing this information, we then proposed an efficient strategy to fabricate fibers with decreased diameter up to only ~3.5 microns (chapter 3). Unfortunately, achieving lower scale fiber diameter remains challenging, and to implement melt electrospinning as a real-world application, further research is required. One promising solution includes compounding the polymer melt with additives to either decrease the viscosity (e.g., plasticizers) or increase the conductivity (e.g., ionic conductive additives). Another way to achieve lower viscosity in polymer melt is by increasing the temperature. However, this needs to be done by precaution as prolonged exposure of the melt to high temperatures can create degradation and deteriorate the overall performance of the fabric.

5.2.2. Morphological and performance data

Systematic advancements in the strategies for improving fiber diameter range in melt electrospinning require methodical exploration and acquiring the material and performance data. So far, despite many interventions in the process design and parameters to achieve the desired fiber

diameter and morphology, the correlated advancements in the microstructural transformations and the subsequent performance of the fabrics (e.g., mechanical properties) are lagging.

Despite missing data for melt electrospun fabrics, other comparable melt processes that are widely commercialized for creating fabrics mainly from polyolefins like PE and polypropylene are well studied[26,27,28,29]. To enhance the access to the performance data of melt electrospun fabrics, this Ph.D. dissertation investigated the mechanical properties of the individual fibers versus the spin-line temperature profile, as the strategy explored in chapter 3 for fiber diameter attenuation. We demonstrated that melt electrospinning is capable of fabricating fibers with diameters comparable to melt-blown fabrics (below 10 microns)[26], with significant mechanical properties comparable to melt spinning[30,31,32]. Potential future directions include studying the crystalline phase orientation and microstructure of the individual fibers versus spinning zone temperature to reveal more ultimate performance information for the melt electrospun fibers.

For the manufacturing segments to be able to take advantage of the alternative approaches like melt electrospinning, especially in a time of crisis like the current pandemic, further enhancement in the materials and performance data is required. Potential areas of improvement in addition to mechanical properties are the filtration efficacy and pressure drop analysis, two important aspects for respirators and surgical masks, basis weight to express how much a nonwoven fabric weighs per unit area, and the fabric thickness versus various process parameters.

5.2.3. Production Rate

A significant long-lasting challenge with electrospinning is the relatively low production rate. Despite many interventions to scale up the electrospinning, this remains unraveled in most cases where a tiny needle is implemented to form the spinning jet. Multi nozzle designs along with free surface setups have been shown to be promising in increasing the production rate[33,34]. Many

of the proposed designs so far have been explored in solution electrospinning, while melt electrospinning has been lagging significantly. (Chapter 1) Here we replaced a single needle with a flat plate surface where the number of jets that form simultaneously increased by 40 folds for a 14 cm plate length. This trajectory has room for improvement, and further research is required. The author proposes complementary designs for further scale-ups. Waterfall design, where multiple plates are in operation as well as bigger sizes of plates that are fed by an extruder, are potential solutions for this limitation.

5.3. Conclusion

Table 5.1 summarizes the progress with Polyethylene (PE) fiber in the literature compared to the product we created in this research. So far, achieving below 10 microns PE fiber from melt processing techniques like melt electrospinning was only possible by increasing the polymer melt temperature well above the melting point to approximately 300 °C. Prolonged exposure of the PE to such high temperatures can be problematic as the degradation temperature of the PE is approximately 370 °C. Here, we were able to create fibers with diameter as low as ~ 3 microns on average with 15% population of the fibers having diameter in the nanometer range (80-800 nm) at very low polymer melt temperature (~ 165 °C) with only precisely controlling the spin-line temperature profile.

Table 5.1. PE fiber fabricated via melt phase fiber fabrication techniques in the literature compared to our product.

Process type	Process temperature (°C)	Ave. fiber diameter (micron)
Melt electrospinning[35] **(Single needle)**	~ 200-220	~ 100
Melt electrospinning[36] **(Single needle)**	~ 315-355	~ 5-6
Melt electrospinning[37] **(Single needle)**	~ 350	~ 5.5
Melt electrospinning[38] **(Free surface)**	~ 360 (in N_2 atmosphere)	~ 10
Melt blowing[26]	~ 255	~ 10
Ours (unconfined melt electrspinning)	~ 165	~ 3.5

While significant progress is still needed for melt electrospinning to be widely used commercially, the fundamental knowledge of polymer melt processing under the electrical field is well-known. Currently, polymer nonwovens surround us in our daily lives in everything from commodity textiles up to high-quality filtration respirators. Moreover, with the role of the current covid-19 pandemic, access to sustainable manufacturing pathways for PPEs has raised significant attention. In most cases, it is important for the new trajectories like melt electrospinning to be comparable in terms of production rate, with a boost in the performance efficacy. There is still much to be accomplished in the research area of free surface melt electrospinning, and we look forward to seeing future interventions.

5.4. References

1. Langner, M., Greiner, A. *Macromol. Rapid Commun.*, 2016, **37**, 351–355.
2. Matulevicius, J., Kliucininkas, L., Martuzevicius, D., Krugly, E., Tichonovas, M., Baltrusaitis, J. *J. Nanomater.*, 2014, **2014**.
3. Gopal, R., Kaur, S., Ma, Z., Chan, C., Ramakrishna, S., Matsuura, T. *J. Memb. Sci.*, 2006, **281**, 581–586.
4. Lv, D., Zhu, M., Jiang, Z., Jiang, S., Zhang, Q., Xiong, R., Huang, C. *Macromol. Mater. Eng.*, 2018, **303**, 1–18.
5. Li, X., Zhang, Y., Li, H., Chen, H., Ding, Y., Yang, W. *Desalination*, 2014, **344**, 266–273.
6. Liu, R., Ji, D., Zhou, G., Liu, Z., Xu, Q., Ramakrishna, S. *Chem. Eng. J.*, 2021, **404**.
7. Lee, S., Obendorf, S. K. *J. Appl. Polym. Sci.*, 2006, **102**, 3430–3437.
8. Zhang, Z., El-moghazy, A. Y., Wisuthiphaet, N., Nitin, N., Castillo, D., Murphy, B. G., Sun, G. 2020.
9. Serbezeanu, D., Popa, A. M., Stelzig, T., Sava, I., Rossi, R. M., Fortunato, G. *Text. Res. J.*, 2015, **85**, 1763–1775.
10. Nagy, Z. K., Balogh, A., Drávavölgyi, G., Ferguson, J., Pataki, H., Vajna, B., Marosi, G. *J. Pharm. Sci.*, 2013, **102**, 508–517.
11. Balogh, A., Drávavölgyi, G., Faragó, K., Farkas, A., Vigh, T., Sóti, P. L., Wagner, I., Madarász, J., Pataki, H., Marosi, G., Nagy, Z. K. *J. Pharm. Sci.*, 2014, **103**, 1278–1287.
12. Balogh, A., Farkas, B., Faragó, K., Farkas, A., Wagner, I., Van Assche, I., Verreck, G., Nagy, Z. K., Marosi, G. *J. Pharm. Sci.*, 2015, **104**, 1767–1776.
13. Ibrahim, Y. S., Hussein, E. A., Zagho, M. M., Abdo, G. G., Elzatahry, A. A. *Int. J. Mol. Sci.*, 2019, **20**, 1–17.

14. Góra, A., Sahay, R., Thavasi, V., Ramakrishna, S. *Polym. Rev.*, 2011, **51**, 265–287.

15. Muerza-Cascante, M. L., Haylock, D., Hutmacher, D. W., Dalton, P. D. *Tissue Eng. - Part B Rev.*, 2015, **21**, 187–202.

16. Cramariuc, B., Cramariuc, R., Scarlet, R., Manea, L. R., Lupu, I. G., Cramariuc, O. *J. Electrostat.*, 2013, **71**, 189–198.

17. Nayak, R., Padhye, R., Kyratzis, I. L., Truong, Y. B., Arnold, L. *Text. Res. J.*, 2013, **83**, 606–617.

18. Nayak, R., Kyratzis, I. L., Truong, Y. B., Padhye, R., Arnold, L. *J. Mater. Sci.*, 2012, **47**, 6387–6396.

19. Lyons, J., Li, C., Ko, F. *Polymer (Guildf).*, 2004, **45**, 7597–7603.

20. Koenig, K., Hermanns, S., Ellerkmann, J., Saralidze, K., Langensiepen, F., Seide, G. *Text. Res. J.*, 2020, **90**, 1948–1961.

21. Nazari, T., Garmabi, H. *J. Appl. Polym. Sci.*, 2016, **133**.

22. Shen, Y., Liu, Q., Deng, B., Yao, P., Xia, S. *Fibers Polym.*, 2016, **17**, 1227–1237.

23. Doustgani, A., Ahmadi, E. *J. Ind. Text.*, 2016, **45**, 626–634.

24. Mayadeo, N., Morikawa, K., Naraghi, M., Green, M. J. *J. Polym. Sci. Part B Polym. Phys.*, 2017, **55**, 1393–1405.

25. Zhou, H., Green, T. B., Joo, Y. L. *Polymer (Guildf).*, 2006, **47**, 7497–7505.

26. Yesil, Y., Bhat, G. S. *Int. J. Cloth. Sci. Technol.*, 2016, **28**, 780–793.

27. Yesil, Y., Bhat, G. S. *J. Text. Inst.*, 2017, **108**, 1035–1040.

28. Choi, K. J., Spruiell, J. E., Fellers, J. F., Wadsworth, L. C. *Polym. Eng. Sci.*, 1988, **28**, 81–89.

29. White, J. L., Dharod, K. C., Clark, E. S. *J. Appl. Polym. Sci.*, 1974, **18**, 2539–2568.

30. Sulong, A. B., Park, J., Azhari, C. H., Jusoff, K. *Compos. Part B Eng.*, 2011, **42**, 11–17.

31. Dees, J. R. 1974, **18**, 1053–1078.

32. Murray, A. T., Gottsegen, J. M. 1997, **29**, 1823–1847.

33. Koenig, K., Beukenberg, K., Langensiepen, F., Seide, G. *Biomater. Res.*, 2019, **23**, 1–12.

34. Yarin, A. L., Zussman, E. *Polymer (Guildf).*, 2004, **45**, 2977–2980.

35. Larrondo, L., Manley, R. S. J. *J. Polym. Sci. Part A-2, Polym. Phys.*, 1981, **19**, 933–940.

36. Deng, R., Liu, Y., Ding, Y., Xie, P., Luo, L., Yang, W. *J. Appl. Polym. Sci.*, 2009, **114**, 166–175.

37. Malakhov, S. N., Chvalun, S. N. *J. Phys. Conf. Ser.*, 2019, **1347**.

38. Morikawa, K., Vashisth, A., Bansala, T., Verma, P., Green, M. J., Naraghi, M. *Macromol. Mater. Eng.*, 2020, **2000106**, 1–7.

APPENDICES

Appendix A-1

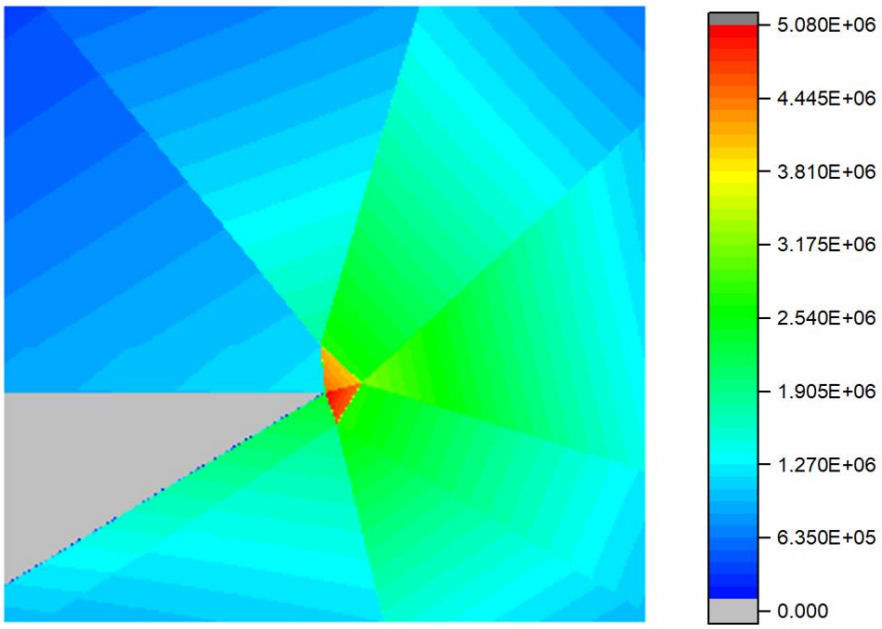

Figure A-1.1. Electric field map near the edge of the source plate using maxwell simulation software; Image demonstares a side view of the plate edge.

Table A-1.1. Electric field magnitude at 500 micron away from the plate edge resulted from simulation at two different configuration of source plate (mode 1 and 2).

Setup configuration- Plate mode	Electric field magnitude (V/m)
Mode 1- vertical plate	2.3E6
Mode 2- horizontal plate	1.8E6

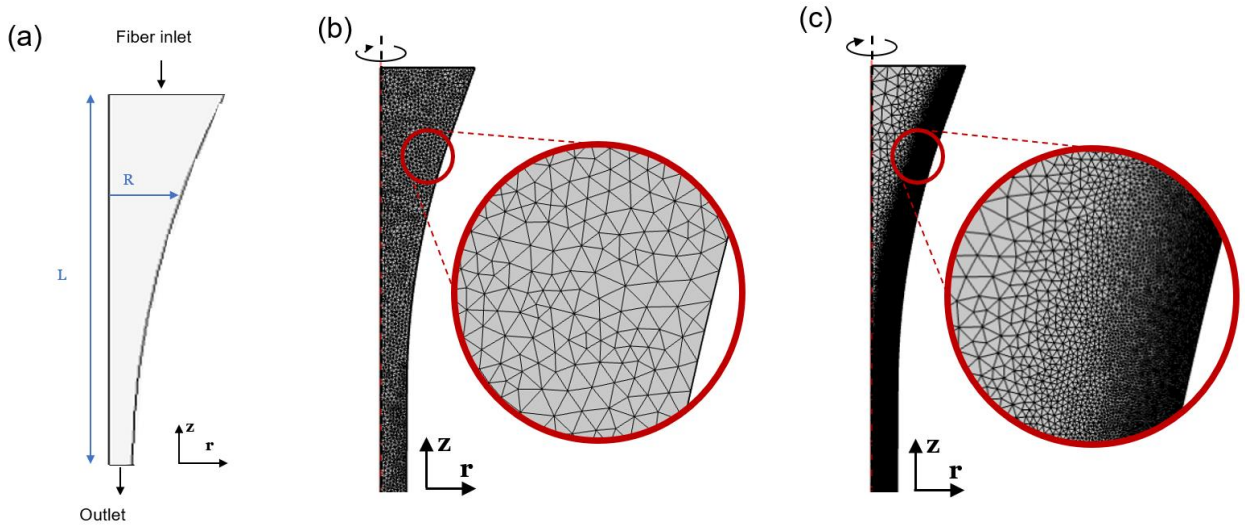

Figure A-1.2. (a) Geometry for boundary condition and Computational domain and mesh grids (b) before, (c) after mesh adaptation algorithm.

Table A-1.2. Material properties and operational conditions used in simulations.

Material Properties				
	Solid phase		**Liquid phase**	
Thermal conductivity[1] **(W/m.K)**	0.31		0.37	
Density (kg/m^3)[2]	922		922	
Heat capacity[3] **(J/kg.K)**	2174		1557	
Viscosity at 140 °C (Pa*s)[2]	~900			
Melting Temperature (K)	402.17			
Temperature transition zone (ΔT)	10.68			
Latent heat of solidification (J/kg)	178550			
Operational Parameters				
	Cone Zone T: RT	**Cone Zone T: 53 ºC**	**Cone Zone T: 95 ºC**	**Cone Zone T: 115 ºC**
Inlet melt flow rate ($m^3/s \times 10^{-11}$)	1.84	1.84	1.84	1.84
Inlet melt temperature (K)	435	435	435	435
Ambient Temperature (K)	301 – 311	308-326	310-386	312-416

Table A-1.3. Adopted boundary conditions (BCs) in computational model.

Momentum Transfer		
@ $\mathbf{r = 0}$	$\partial \mathrm{U}_r / \partial r = 0$	Axisymmetric
@ $\mathbf{r = R}$	$\mathrm{U.n} = 0$	Slip condition
@ $\mathbf{z = 0}$	$P = P_{atm}$	Outlet pressure
@ $\mathbf{z = L}$	$\dot{m} = \dot{m}_{in}$	Inlet mass flow
Heat Transfer		
@ $\mathbf{r = 0}$	$\partial \mathrm{T} / \partial r = 0$	Axisymmetric
@ $\mathbf{r = R}$	$K\, \partial \mathrm{T} / \partial r = h(T - T_{sur.})$	Heat flux (convection)
@ $\mathbf{z = 0}$	$K \nabla \mathrm{T} = 0$	Convection outflow
@ $\mathbf{z = L}$	$T = T_{in}$	Inlet Temperature

Table A-1.4. Surface tension and the inter-jet spacing calculated based on the cone surface temperature derived from the equation

Cone-Zone Temperature (spin-line profile)	**Cone zone T: RT**	**Cone zone T: 53 °C**	**Cone zone T: 95 °C**	**Cone zone T: 115 °C**
Cone surface temperature (500-micron on the jet-based on simulation)	157.7	159.1	160.8	161.7
Surface tension (mN/m)	26.9	26.9	26.8	26.8
Inter-jet spacing (cm)	0.8	0.8	0.8	0.8

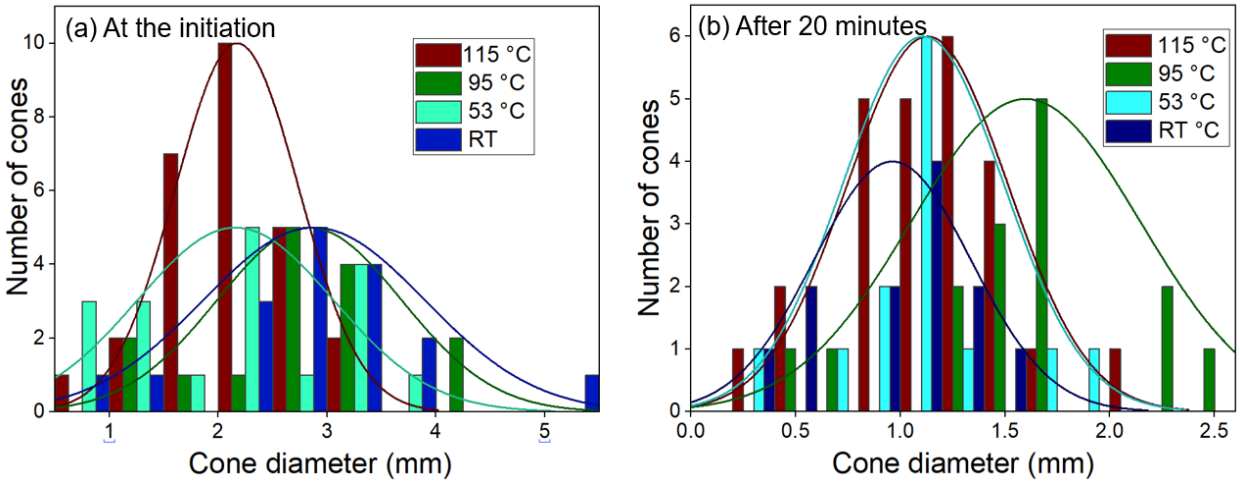

Figure A-1.3. Cone diameter distribution of different spin-line temperature profiles for (a) at the initiation stage (b) after 20 minutes run of the experiment.

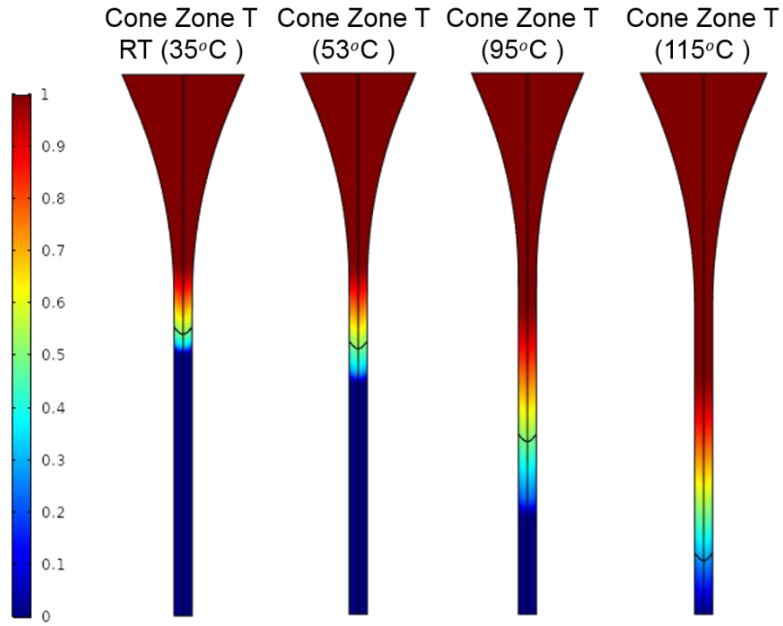

Figure A-1.4. 2D phase fraction distribution inside fiber jets. Picture shows the first 15 mm distance from the cone of fibers.

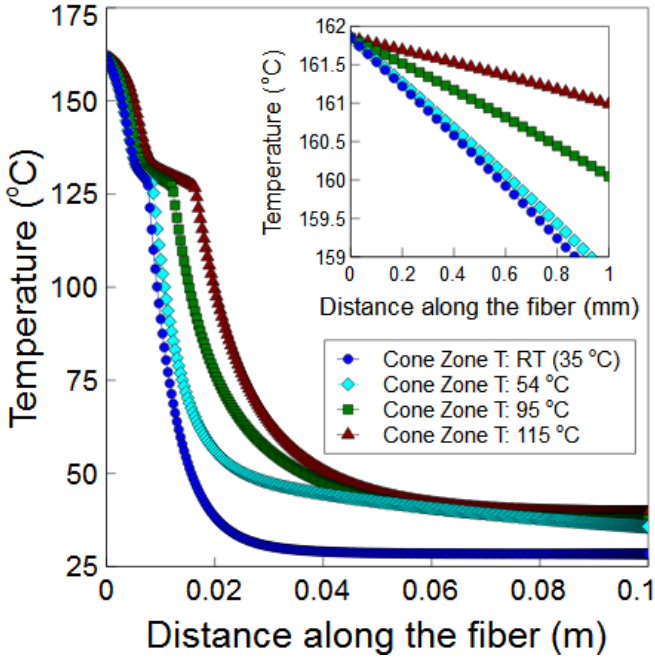

Figure A-1.5. Variation of fiber temperature at its centerline for different spin-line temperature profiles.

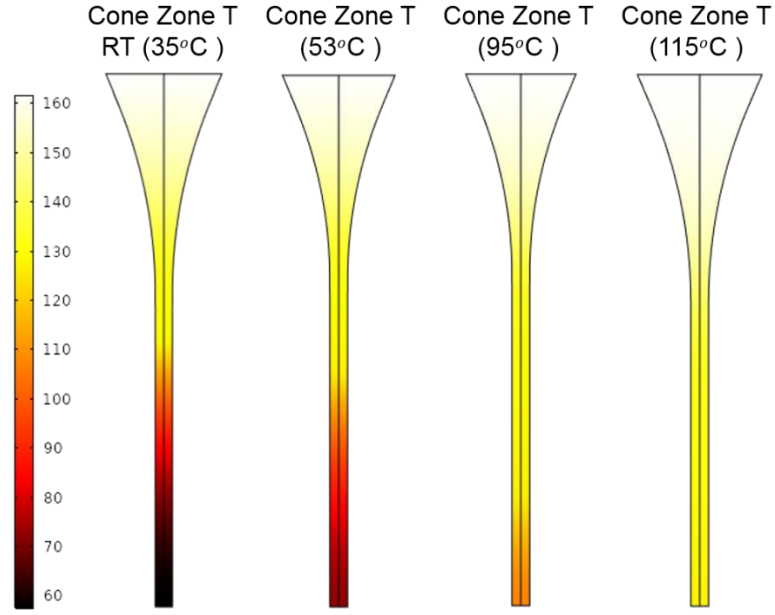

Figure A-1.6. 2D temperature distribution inside fiber jets. Picture shows the first 15 mm distance from the cone of fibers.

References

(1) Sobolciak, P.; Karkri, M.; Al-maadeed, M. A.; Krupa, I. Thermal Characterization of Phase Change Materials Based on Linear Low- Density Polyethylene , Paraffin Wax and Expanded Graphite. *Renew. Energy* **2016**, *88*, 372–382. https://doi.org/10.1016/j.renene.2015.11.056.

(2) Wang, Q.; Curtis, C. K.; Thoppey, N. M.; Bochinski, J. R.; Gorga, R. E.; Clarke, L. I. Unconfined, Melt Edge Electrospinning from Multiple, Spontaneous, Self-Organized Polymer Jets. *Mater. Res. Express* **2015**, *1* (4), 45304. https://doi.org/10.1088/2053-1591/1/4/045304.

(3) Loufakis, K.; Wunderlich, B. Heat Capacities of Polyethylene and Linear Fluoropolymers. *Polymer* **1985**, *26*, 1875–1884. https://doi.org/10.1016/0032-3861(85)90018-7

Appendix A-2

A-2.1 Single fiber specimen preparation and test method

Individual fibers are teased out of a spool of bulk polyethylene (PE) fibers. Fiber diameter is evaluated by optical microscope prior to testing as is shown in Figure A-2.1-a. One diameter measurement is drawn from each image of the fiber gage sections. Fibers are chosen based on their dimeter proximity to the average fiber diameter reported via SEM for the bulk sample. Single fibers are then mounted on the index card frames. (Figure A-2.1-b)

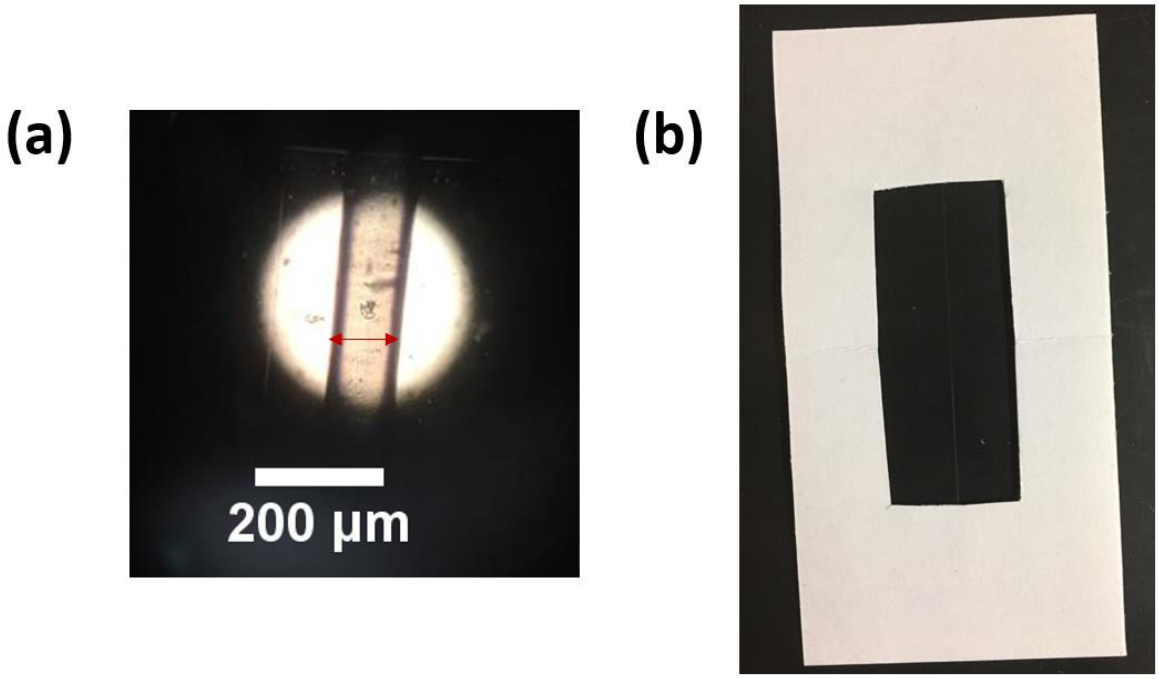

Figure A-2.1. (a) Example of the fiber diameter measurement using an image captured with the optical microscope (b) Fiber specimen mounted on the index card frame.

The interior dimensions of the frame are designed to yield the desired fiber gage length. The gage length was selected as 5 cm, accepted by ASTM D3822. Specific dimensions for the frames used in this work are shown in Figure A-2.2 for gage length of 5 cm.

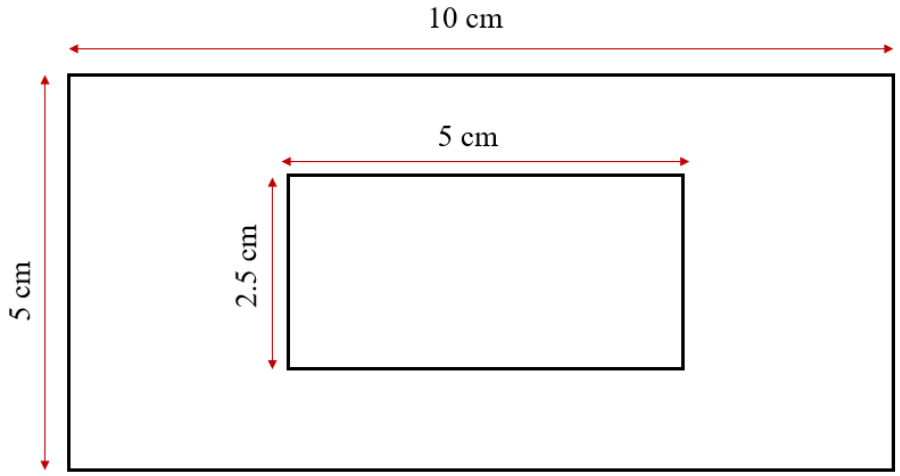

Figure A-2.2. Mounting frame dimensions for a 5-cm gage length sample.

Adjustments are made to center the fiber on the mount and once the position is finalized the fibers are secured into place using a small amount of superglue on the two ends and left to dry overnight. Approximately 10-15 specimens are prepared from each sample type.

The mounted specimen is placed into the grips on the Instron (model 5544) load frame with a load cell of 0.5-2 N as shown in Figure A-2.3. Using the tension-compression jog controls manually on the instrument, the crosshead is moved to press the grips against the specimen as much as possible without deforming the index card frame. Just prior to testing, the edges of the index card frame are cut. After the testing, to validate fracture failure with no slippage from the grips, the fiber ends are examined to still be glued to the index card. Specimens that are failed due to the grip slippage are discarded.

The instrument is operated in displacement control mode at a rate of 0.008 ε/s. Load and crosshead displacement data are recorded by the BlueHill software. The test typically lasts between 10 and 20 minutes and stops manually several seconds after failure. Fiber fragments are recovered if possible and logged for posttest investigation of fracture surface.

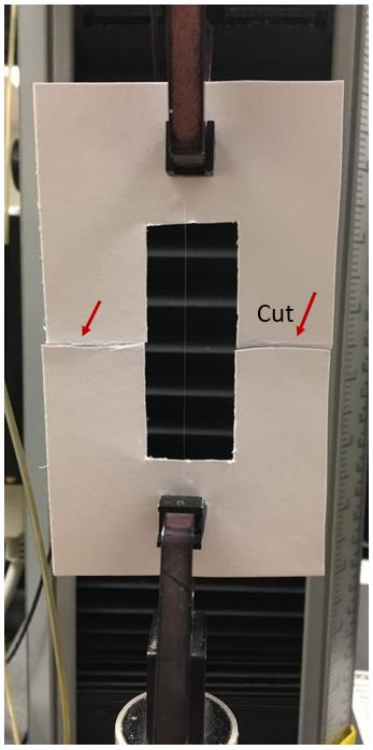

Figure A-2.3. Fiber sample installed in the instrument after the index card frame is cut.

A-2.2 Dynamic Mechanical Analysis (DMA)

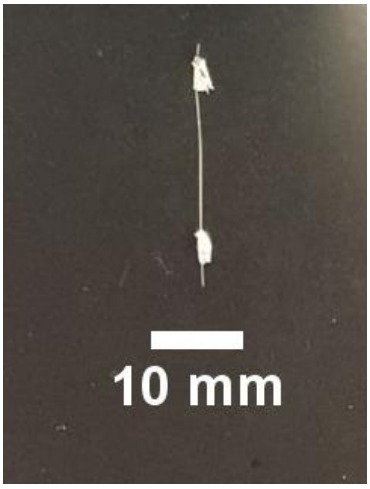

Figure A-2.4. Single fiber sample taped at the ends for the DMA measurement.

A-2.3 Computational fluid dynamic simulation

A comprehensive numerical approach was applied in order to describe the phase change process of the polymer melt in the electrospinning process. Heat and momentum transport equations along with continuity equations were numerically solved using Finite Element Method (FEM) to describe the fluid flow and temperature gradients throughout the fiber jet. Zero shear rate viscosity of the polyethylene at the experiments temperature was experimentally measured and substituted in the momentum equation. As the system is a continuous process, steady state model was utilized. All simulations were performed in a 2D-axisymmetric framework with the aid of commercial code COMSOL MULTIPHYSICS 5.5.

A-2.4 Differential Scanning Calorimetry (DSC)

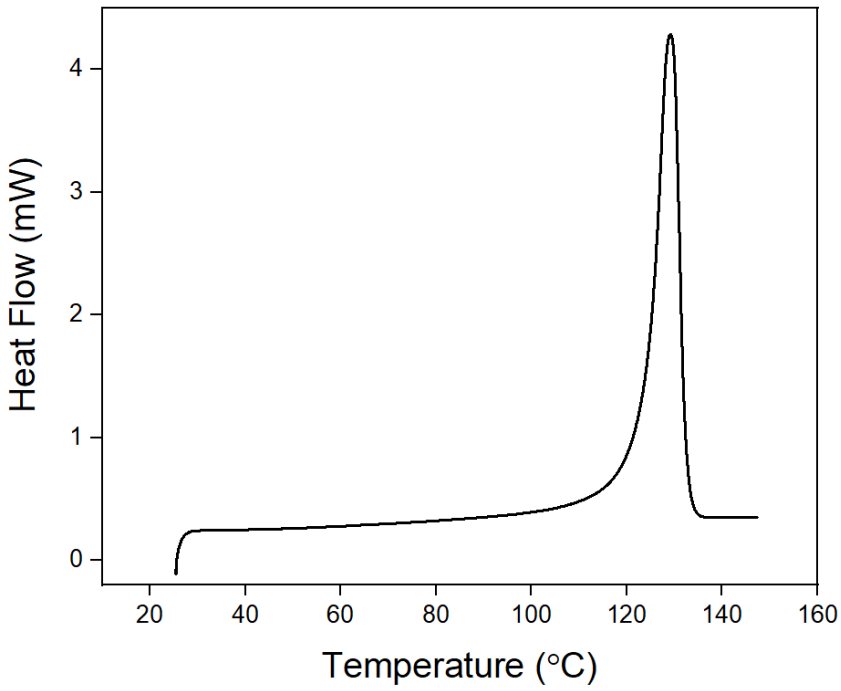

Figure A-2.5. DSC thermogram of the LLDPE granule with a heating rate of 10 °C/min. The melting peak temperature is 129 °C with a enthalpy of 179 J/g.